



## EVALUATION OF THE OXIDATION RESPONSE AND FIBER-MATRIX COMPATIBILITY IN ALUMINUM-RICH INTERMETALLIC COMPOSITES

William E. Frazier, Jeffrey Cook and Thu-Ha T. Mickle  
Air Vehicle and Crew Systems Technology Department (Code 6063)  
NAVAL AIR WARFARE CENTER  
AIRCRAFT DIVISION WARMINSTER  
P.O. Box 5152  
Warminster, PA 18974-0591

DTIC  
ELECTE  
JAN 20 1995  
S G D

17 November 1993

FINAL REPORT  
Period Covering October 1989 To September 1993

Approved for Public Release; Distribution is Unlimited

Prepared for  
OFFICE OF NAVAL RESEARCH (Code 11)  
800 N. Quincy St.  
Arlington, VA 22217-5660

19950118 013

## NOTICES

**REPORT NUMBERING SYSTEM** — The numbering of technical project reports issued by the Naval Air Warfare Center, Aircraft Division, Warminster is arranged for specific identification purposes. Each number consists of the Center acronym, the calendar year in which the number was assigned, the sequence number of the report within the specific calendar year, and the official 2-digit correspondence code of the Functional Department responsible for the report. For example: Report No. NAWCADWAR-92001-60 indicates the first Center report for the year 1992 and prepared by the Air Vehicle and Crew Systems Technology Department. The numerical codes are as follows:

CODE	OFFICE OR DEPARTMENT
00	Commanding Officer, NAWCADWAR
01	Technical Director, NAWCADWAR
05	Computer Department
10	AntiSubmarine Warfare Systems Department
20	Tactical Air Systems Department
30	Warfare Systems Analysis Department
50	Mission Avionics Technology Department
60	Air Vehicle & Crew Systems Technology Department
70	Systems & Software Technology Department
80	Engineering Support Group
90	Test & Evaluation Group

**PRODUCT ENDORSEMENT** — The discussion or instructions concerning commercial products herein do not constitute an endorsement by the Government nor do they convey or imply the license or right to use such products.

Reviewed By: J. Waldman Date: 12 Aug 94  
Branch Head

Reviewed By: J. Shaffer Date: 22 Aug 94  
Division Head

Reviewed By: F. K. [Signature] Date: 23 Aug 94  
Director/Deputy Director

REPORT DOCUMENTATION PAGE			Form Approved OMB No. 0704-0188	
Public reporting burden for this collection of information is estimated to average 1 hour per response, including the time for reviewing instructions, searching existing data sources, gathering and maintaining the data needed, and completing and reviewing the collection of information. Send comments regarding this burden estimate or any other aspect of this collection of information, including suggestions for reducing this burden, to Washington Headquarters Services, Directorate for Information Operations and Reports, 1215 Jefferson Davis Highway, Suite 1204, Arlington, VA 22202-4302, and to the Office of Management and Budget, Paperwork Reduction Project (0704-0188), Washington, DC 20503.				
1. AGENCY USE ONLY (Leave blank)	2. REPORT DATE 17 NOV 1993	3. REPORT TYPE AND DATES COVERED Final 10/89 - 9/93		
4. TITLE AND SUBTITLE EVALUATION OF THE OXIDATION RESPONSE AND FIBER-MATRIX COMPATIBILITY IN ALUMINUM-RICH INTERMETALLIC COMPOSITES		5. FUNDING NUMBERS		
6. AUTHOR(S) William E. Frazier, Jeffrey Cook and Thu-Ha T. Mickle				
7. PERFORMING ORGANIZATION NAME(S) AND ADDRESS(ES) Air Vehicle and Crew Systems Technology Department (Code 6063) NAVAL AIR WARFARE CENTER AIRCRAFT DIVISION WARMINSTER P.O. Box 5152 Warminster, PA 18974-0591		8. PERFORMING ORGANIZATION REPORT NUMBER  NAWCADWAR-93083-60		
9. SPONSORING / MONITORING AGENCY NAME(S) AND ADDRESS(ES)  OFFICE OF NAVAL RESEARCH (Code 11) 800 N. Quincy St. Arlington, VA 22217-5660		10. SPONSORING / MONITORING AGENCY REPORT NUMBER		
11. SUPPLEMENTARY NOTES				
12a. DISTRIBUTION / AVAILABILITY STATEMENT  Approved for Public Release; Distribution is Unlimited			12b. DISTRIBUTION CODE	
13. ABSTRACT (Maximum 200 words) <p>The present study was undertaken in order to elucidate the role of fiber-matrix interactions on the oxidation response of <math>Al_3Ti</math>-based metal matrix composites. The fibers examined in this work were SCS-6, <math>TiB_2</math>, and Saphikon. Since these trialuminides have very high melting points, a solid state powder processing fabrication route was chosen in order to minimize fiber degradation. The matrix alloy was rapidly solidified by melt spinning in order to insure compositional homogeneity. A hammer mill was used to comminute the alloy ribbon into -40 mesh powder. The powder and fibers were then encapsulated in titanium cans, hot vacuum degassed, and hot isostatically pressed. Preliminary investigations indicated that <math>Al_3Ti</math>'s narrow range of compositional stability could present difficulties: excess aluminum could melt and vigorously attack fibers at the HIP consolidation temperatures, viz., 1100 °C and 1200 °C. Niobium additions were used to expand the phase field of <math>Al_3Ti</math> and reduce the alloy's propensity to partition aluminum during melt processing. HIP consolidated composites all exhibited some matrix cracking making them unsuitable for oxidation studies. However, the oxidation response of the monolithic matrix alloys was investigated. The extent of fiber-matrix reaction owing to the HIP consolidation procedure was also pursued. The SCS-6 fibers reacted severely with the matrix materials. The <math>TiB_2</math> fibers did not experience significant chemical degradation although significant diffusion and cracking was observed. Saphikon was the least affected by the consolidation process. The fiber does not react chemically with the matrix materials; however, differences in the thermal expansivities of the fiber and matrix materials are believed responsible for extensive cracking.</p>				
14. SUBJECT TERMS Fiber-Matrix Interactions, Oxidation Response, <del>INTERMETALLIC</del> ALUMINUM-RICH INTERMETALLIC COMPOSITES			15. NUMBER OF PAGES	
			16. PRICE CODE	
17. SECURITY CLASSIFICATION OF REPORT UNCLASSIFIED	18. SECURITY CLASSIFICATION OF THIS PAGE UNCLASSIFIED	19. SECURITY CLASSIFICATION OF ABSTRACT UNCLASSIFIED	20. LIMITATION OF ABSTRACT SAR	

**ABSTRACT**

The present study was undertaken in order to elucidate the role of fiber-matrix interactions on the oxidation response of  $\text{Al}_3\text{Ti}$ -based metal matrix composites. The fibers examined in this work were SCS-6,  $\text{TiB}_2$ , and Saphikon. Since these trialuminides have very high melting points, a solid state powder processing fabrication route was chosen in order to minimize fiber degradation. The matrix alloy was rapidly solidified by melt spinning in order to insure compositional homogeneity. A hammer mill was used to comminute the alloy ribbon into -40 mesh powder. The powder and fibers were then encapsulated in titanium cans, hot vacuum degassed, and hot isostatically pressed. Preliminary investigations indicated that  $\text{Al}_3\text{Ti}$ 's narrow range of compositional stability could present difficulties: excess aluminum could melt and vigorously attack fibers at the HIP consolidation temperatures, viz., 1100 °C and 1200 °C. Niobium additions were used to expand the phase field of  $\text{Al}_3\text{Ti}$  and reduce the alloy's propensity to partition aluminum during melt processing. HIP consolidated composites all exhibited some matrix cracking making them unsuitable for oxidation studies. However, the oxidation response of the monolithic matrix alloys was investigated. The extent of fiber-matrix reaction owing to the HIP consolidation procedure was also pursued. The SCS-6 fibers reacted severely with the matrix materials. The  $\text{TiB}_2$  fibers did not experience significant chemical degradation although significant diffusion and cracking was observed. Saphikon was the least affected by the consolidation process. The fiber does not react chemically with the matrix materials; however, differences in the thermal expansivities of the fiber and matrix materials is believed responsible for extensive cracking.

## Table of Contents

Abstract.....	ii
List of Figures.....	iv
List of Tables.....	vi
Introduction.....	1
The Trialuminide Matrix.....	1
Fiber Toughening in brittle matrix.....	2
Fiber Properties.....	2
Fiber-Matrix Compatibility.....	3
Prior HIP Work at the NAWC.....	5
Oxidation.....	6
Experimental Procedure.....	8
Materials Processing.....	8
Microstructural Characterization.....	10
Oxidation.....	11
Thermodynamics.....	12
Experimental Results.....	13
Optical Metallography.....	13
X-Ray Diffraction.....	16
Differential Thermal Analysis.....	16
Oxidation.....	16
Thermodynamic Evaluation.....	18
Discussion of Results.....	20
Fiber-Matrix Thermal Expansion Mismatch.....	20
Oxidation.....	22
Conclusions.....	33
Acknowledgments.....	34
References.....	34

Accession For	
NTIS	CRA&I <input checked="" type="checkbox"/>
DTIC	TAB <input type="checkbox"/>
Unannounced <input type="checkbox"/>	
Justification .....	
By .....	
Distribution / .....	
Availability Codes	
Dist	Avail and/or Special
A-1	

## List of Figures

1. The Aluminum-Titanium Equilibrium Phase Diagram.
2. Crystal structure from  $L1_2$  to  $DO_{22}$ .
3. HIP Map for the Consolidation of  $Al_3Ti$ .
4. Isothermal Section of the Al-Ti-Nb Equilibrium Phase Diagram at 1200 °C.
5. Marko Materials Melt Spinner.
6. Optical Micrographs of  $TiB_2$  Fiber Composites Consolidated at 1100 °C: (a)  $Al_3Ti$  Matrix, and (b)  $Al_3Ti$  + Nb Matrix.
7. Optical Micrographs of  $TiB_2$  Fiber Composites Consolidated at 1200 °C: (a)  $Al_3Ti$  Matrix, and (b)  $Al_3Ti$  + Nb Matrix.
8. Optical Micrographs of SCS-6 Fiber Composites Consolidated in  $Al_3Ti$  + Nb Matrix: (a) at 1100 °C, and (b) at 1200 °C.
9. Optical Micrographs of Saphikon Fiber Composites Consolidated at 1100 °C: (a)  $Al_3Ti$  Matrix, and (b)  $Al_3Ti$  + Nb Matrix.
10. Optical Micrographs of Saphikon Fiber Composites Consolidated at 1200 °C: (a)  $Al_3Ti$  Matrix, and (b)  $Al_3Ti$  + Nb Matrix.
11.  $Al_3Ti/TiB_2$  Composites HIPed at 1100 °C: (a) SEM Micrograph, (b) EDS Map for Aluminum, and (c) EDS Map for Molybdenum.
12. SEM Micrograph of  $Al_3Ti/TiB_2$  Composites HIPed at 1200 °C.
13. SEM Micrograph of  $Al_3(Ti, Nb)/TiB_2$  Composites HIPed at 1100 °C.
14. SEM Micrograph of  $Al_3(Ti, Nb)/TiB_2$  Composites HIPed at 1200 °C.
15.  $Al_3Ti/SCS-6$  Composites HIPed at 1100 °C: (a) SEM Micrograph, (b) EDS Map for Aluminum, and (c) EDS Map for Titanium.
16.  $Al_3Ti/SCS-6$  Composites HIPed at 1200 °C: (a) SEM Micrograph, (b) EDS Map for Aluminum, and (c) EDS Map for Titanium.
17.  $Al_3(Ti, Nb)/SCS-6$  Composites HIPed at 1100 °C: (a) SEM Micrograph, (b) EDS Map for Aluminum, and (c) EDS Map for Titanium.
18.  $Al_3(Ti, Nb)/SCS-6$  Composites HIPed at 1200 °C: (a) SEM Micrograph, (b) EDS Map for Aluminum, and (c) EDS Map for Titanium.

## NAWCADWAR-93083-60

19. SEM Micrographs of  $\text{Al}_3\text{Ti}$ /Saphikon Composites HIPed at (a) 1100 °C and (b) 1200 °C
20.  $\text{Al}_3(\text{Ti}, \text{Nb})$ /Saphikon Composites HIPed at 1100 °C:  
(a) SEM Micrograph, (b) EDS Map for Oxygen, and (c) EDS Map for Titanium.
21. X-ray Diffraction Profiles for (i) melt spun  $\text{Al}_3\text{Ti}$  and (ii) melt spun  $\text{Al}_3\text{Ti} + \text{Nb}$ .
22. Differential Thermal Analysis Profile for  $\text{Al}_3\text{Ti} + \text{Nb}$ .
23. Weight Gain of  $\text{AlTi}$  in Cyclic Oxidation.
24. Appearance of Specimens after 28 Hours Cyclic Oxidation at 1100°C: (a)  $\text{AlTi}$  and (b)  $\text{Al}_5\text{CuTi}_2$ .
25. Weight Gain of  $\text{Al}_3\text{Ti}$  in Cyclic Oxidation.
26. Weight Gain of  $\text{Al}_5\text{CuTi}_2$  in Cyclic Oxidation.
27. Weight Gain of  $\text{AlTi}$  in Isothermal Oxidation.
28. Weight Gain of  $\text{Al}_3\text{Ti}$  in Isothermal Oxidation.
29. Weight Gain of  $\text{Al}_5\text{CuTi}_2$  in Isothermal Oxidation.
30. Solubility of Titanium in Aluminum.
31. Calculated Activity of Titanium in  $\text{Al}_3\text{Ti}$ .
32. Al-C-O Phase Stability Diagram at 1200°C.
33. Al-C-O Phase Stability Diagram at 1200°C.
34. SEM Image of  $\text{AlTi}$  after Cyclic Oxidation, Showing Internal Oxidation of Aluminum.
35. Oxidation Kinetics for  $\text{AlTi}$ .
36. SEM Image Showing the Oxide Layer on  $\text{AlTi}$  after 48 hours Isothermal Oxidation at 1100°C.
37. Parabolic Weight Gain Curves for  $\text{Al}_3\text{Ti}$  in Cyclic Oxidation.
38. Oxidation Kinetics for  $\text{Al}_3\text{Ti}$ .
39. Parabolic Weight Gain Curves for  $\text{Al}_3\text{Ti}$  in Isothermal Oxidation.
40. SEM Image of  $\text{Al}_3\text{Ti}$  Showing External Oxide Formation and Internal Oxidation after Isothermal Exposure at 1100°C.
41. Parabolic Weight Gain Curves for  $\text{Al}_5\text{CuTi}_2$  in Cyclic Oxidation.
42. Parabolic Weight Gain Curves for  $\text{Al}_5\text{CuTi}_2$  in Isothermal Oxidation.

LIST OF TABLES

1. Typical Fiber Properties [19]
2. Alloy Compositions, Wt. %
3. Types of Fiber Investigated
4. Composite Test Matrix
5. Alloy Compositions (wt, %)- Oxidation Evaluation
6. Summary of Fiber-Matrix Interactions
7. Thermodynamic Constants for the Formation of  $\text{Al}_3\text{Ti}$ .
8. The Estimated Enthalpy and Entropy Associated with the Dissolution of Titanium in a Dilute Solution.
9. Estimated HIP Processing Induced Fiber Stress.
10. Possible Reaction Products for  $\text{Al}_3\text{Ti}/\text{SCS-6}$
11.  $\text{AlTi}$  Oxidation Kinetics
12.  $\text{Al}_3\text{Ti}$  Parabolic Oxidation Parameters
13.  $\text{Al}_3\text{Ti}$ : Calculated n-Exponents
14.  $\text{Al}_5\text{CuTi}_2$  Parabolic Rate Constants



## INTRODUCTION

### The Trialuminide Matrix

Alloys based on the titanium rich portion of the aluminum-titanium phase diagram have been the subject of intense scientific and developmental work [1]. The benefits of the substantial engineering investment in the alpha, the super-alpha-two, and the gamma titanium aluminide materials are now beginning to be realized: improvements have been made in ductility, toughness, elevated temperature strength, and deformation processing [2]. However, the exploration of the aluminum rich portion of the aluminum-titanium phase diagram is still in its infancy.

As illustrated by the aluminum-titanium phase diagram,  $\text{Al}_3\text{Ti}$  is an aluminum rich, thermodynamically stable intermetallic existing both at ambient and elevated temperatures, Figure 1 [3]. The exploitation of titanium trialuminide based alloys as aircraft materials is of significant interest because of their high melting point ( $1350^\circ\text{C}$ ), high elastic moduli (170 GPa), low density ( $3.35\text{ gcm}^{-3}$ ), and elevated temperature strength [4,5]. In addition, because the trialuminides are approximately 75 atom percent aluminum their oxidation resistance is expected to be superior to that of the alpha-two and gamma titanium aluminides.

The use of titanium trialuminides has been seriously impeded by their lack of tensile ductility and their poor fracture toughness.  $\text{Al}_3\text{Ti}$  has a  $\text{DO}_{22}$  crystal structure; and therefore, may lack the slip systems necessary to satisfy von Mises criterion for slip deformation in polycrystals. Thus, at ambient temperatures the preferred deformation mode of  $\text{Al}_3\text{Ti}$  is by twinning of the  $\{111\}\langle 112 \rangle$  type [5]. Based, in part, on Pettifor's "Structure Map" [6], attempts have been made to improve ductility by alloying with various transition elements, e.g., Fe, Cu, Mn, Cr, and Ni [7, 8, 9]. Alloying with these transition elements can convert the crystal structure of  $\text{Al}_3\text{Ti}$  from  $\text{DO}_{22}$  to  $\text{L}_{12}$ , Figure 2. The  $\text{L}_{12}$  structure is closely related to the  $\text{DO}_{22}$  structure, i.e., a  $1/2[110]$  shift on every  $\text{DO}_{22}$  (001) plane results in the  $\text{L}_{12}$  [10]. Other alloys with the  $\text{L}_{12}$  crystal structure, such as  $\text{Cu}_3\text{Au}$  and  $\text{Ni}_3\text{Al}$ , are ductile in the single crystal form [11, 12]. Unfortunately, even though some  $(\text{Al}, \text{X})_3\text{Ti}$  compounds have an  $\text{L}_{12}$  crystal structure, they too fail in a brittle manner: transgranular cleavage predominates on the (110) and (111) planes [10, 11, 12].

Attempts have been made to establish why these alloys fail by transgranular cleavage. Auger analysis of the fracture surfaces has not been able to attribute failure to the presence of second phase particles or solute segregation on the cleavage planes [12]. Full-potential linearized

augmented plane wave (FLAPW) analysis indicates cleavage results because of the highly directional, "p-d", aluminum-titanium bonds [13]. Fu [13] suggests that alloying to enhance dislocation dissociation may be possible and result in improved ductility. Unfortunately, macro alloying with various transition elements and micro alloying with boron have not significantly improved ductility [8, 9].

### **Fiber Toughening in brittle matrix**

The toughening of brittle materials with fibers, particles, etc., is the subject of intense research [14, 15, 16]. Some of the energy absorbing processes which enhance fracture toughness in fiber reinforced composites include (1) fiber-matrix debonding, (2) matrix or fiber deformation, (3) fiber pull-out, and (4) crack deflection at weak interfaces.

Continuous fiber reinforced intermetallic matrix composites are being investigated as a means of improving the strength and enhancing the toughness of brittle aluminum-rich intermetallic alloys. The presence of fibers may slow down or arrest crack growth by deflecting and bridging cracks [17]; the strength of the composite is enhanced by the transference of load to the higher strength fibers. In order for the crack bridging mechanism of fiber toughening to be operative, fiber-matrix debonding must occur prior to fiber failure at the crack front. Once debonding has occurred, the sliding resistance along the interface governs the load transfer. This is exemplified by fiber pull-out. The toughness of the material is increased by a high rate of debonding and a low sliding resistance along the debonded interface.

Critical in the development of these composites is the thermodynamic and mechanical compatibility of the fiber, matrix, and fiber-matrix interphase region [18]. The properties of the interphase dictates how much fiber-matrix debonding occurs.

### **Fiber Properties**

There are a large number of mono-filament and tow fibers commercially available. Table 1 list some of the fibers which are either currently employed in metal matrix composites (MMC) or which exhibit potential for applications in MMC. Selection of a fiber for incorporation into a metal matrix involves more than choosing a fiber based upon its strength, modulus, and density. The cost and availability of the fiber as well as its chemical compatibility and thermal expansivity match with the matrix must be considered.

Three fibers exhibiting potential for incorporation into  $\text{Al}_2\text{Ti}$  include (i) Saphikon, (ii) SCS-6, and (iii)  $\text{TiB}_2$ . Saphikon is a single crystal sapphire ( $\text{Al}_2\text{O}_3$ ) fiber with a non circular cross section that varies along its length. Saphikon has high temperature potential, but it is very costly. Textron Specialty Materials produce both SCS-6 and  $\text{TiB}_2$  fibers. The SCS-6 fiber is a 140  $\mu\text{m}$  diameter monofilament and is produced by chemical vapor deposition (CVD). It consists of a 33 $\mu\text{m}$  diameter carbon core and radially oriented  $\beta$ - $\text{SiC}$ . The surface of the fiber has a carbon rich layer used to inhibit degradation. The high strength (72.5 MPa), high modulus (415 GPa), and low density ( $3.0 \text{ gcm}^{-3}$ ) of SCS-6 fibers make them attractive for use as reinforcing fibers. This fiber is also the most commercialized and thus one of the most cost effective. Textron has also made research quantities of 80  $\mu\text{m}$  diameter  $\text{TiB}_2$  fiber. The fiber is made by CVD  $\text{TiB}_2$  onto a 27  $\mu\text{m}$  diameter Mo core.

### Fiber-Matrix Compatibility

A thermodynamic rationale for predicting the chemical stability of fiber-matrix systems has been explored by Misra [18,20]. Because of the lack of reliable thermodynamic data for ternary phases he confined his work to binary systems. Basically he examined four types of reactions: (i) formation of reaction products that have unit activity, (ii) the formation of reaction products at less than unit activity, (iii) the formation of gaseous reaction products, and (iv) the effect of non-stoichiometry of the reinforcement material on chemical compatibility. Reactions can proceed at less than unit activity by dissolving in the matrix or in the reinforcement material. For an iron aluminide matrix,  $\text{Al}_2\text{O}_3$  was found to be the best type of reinforcement; other acceptable reinforcement included  $\text{TiB}_2$  and  $\text{TiC}$ [18]. In another study, the compatibility of various reinforcement with Niobium aluminides was investigated[20].  $\text{Nb}_3\text{Al}$  and  $\text{Nb}_2\text{Al}$  were found to be compatible with  $\text{Al}_2\text{O}_3$  but incompatible with  $\text{TiB}_2$ ,  $\text{SiC}$ ,  $\text{TiC}$ .

Jones et al. have examined the interphase of SCS-6/Ti-6Al-4V metal matrix composites.  $\text{TiC}$  particles were observed to form at the fiber-matrix interface along with a concurrent reduction in the pyrocarbon layer. The authors observed carbon-rich hexagonal phase  $\text{Ti}_x\text{Si}_y(\text{C})$  present in the as-received composite with its (0001) axis preferentially oriented perpendicular to the fiber's surface. This carbon-rich silicide was reported to transform to the more thermodynamically stable  $\text{Ti}_5\text{Si}_3$  phase.

Table 1 Typical Fiber Properties [19]

Fiber	Diameter ( $\mu\text{m}$ )	Density ( $\text{g/cm}^3$ )	CTE, ( $10^{-6}/^\circ\text{C}$ )	UTS, (GPa)	Modulus( GPa)	React- ivity with Ti
Sapphire	76-152	4.0	8.8	2.1-3.4	448	M
SCS-6	142	3.0	4.8	3.4-4.1	428	L
Sigma	102	3.4	4.8	2.8-3.4	407	M
TiB <sub>2</sub>	76	4.5	8.0	2.1-3.4	448	L
TiC	76	4.8	8.6	2.1-3.4	428	L
Carbon	25.4	2.1	0.0	2.8-3.4	414- 1,030	M
Boron	152	2.5	8.2	3.1-3.8	345	M

Ti-6Al-4V alloys reinforced with TiC and SiC particles have been examined by Loretto and Konitzer [21]. TiC was found to react with the matrix forming Ti<sub>2</sub>C. SiC was found to react with the matrix and form Ti<sub>5</sub>Si<sub>3</sub> and TiC.

Fiber-matrix interactions were investigated for the Ti3Al + Nb/SCS-6 MMC by Baumann et al. [22]. Concentric reaction zones were observed to form between the Ti-25Al-13Nb matrix and the SiC fiber. The zone closest to the fiber contained two types of particles: (Ti, Nb)C<sub>1-x</sub> based upon TiC, and (Ti, Nb, Al)<sub>5</sub>Si<sub>3</sub> based on Ti<sub>5</sub>Si<sub>3</sub>. The outer zone was reported to contain two phases: (Ti, Nb)<sub>3</sub>AlC based upon Ti<sub>3</sub>AlC and (Ti, Nb, Al)<sub>5</sub>Si<sub>3</sub>. This complex silicide was reported to have a hexagonal crystal structure with  $a = 7.74\text{\AA}$  and  $c = 5.45\text{\AA}$ .

The properties of DuPont's PRD-166 (a 20 $\mu\text{m}$  diameter, polycrystalline Al<sub>2</sub>O<sub>3</sub> + 20 wt% ZrO<sub>2</sub>) fiber reinforced, pressure cast TiAl have been investigated by Naurbakhsh et al. Extensive reaction was reported. ZrO<sub>2</sub> particles decorate the fiber-matrix interface. ZrO<sub>2</sub> free, Al<sub>2</sub>O<sub>3</sub> grains are observed in the fiber interior.

Prior HIP Work at the NAWC

The powder processing route was chosen early on in this work in order to eliminate liquid metal-fiber reactions. Rapidly solidified alloy powders were produced by a process of melt spinning and comminution. Melt spinning was expected to produce high purity material which was chemically homogeneous with a very fine microstructure. The powders were then consolidated by hot isostatic pressing (HIP) and the HIP parameters were varied in order to identify the processing which yields dense material with maximum ductility. Thus, the approach taken was to enhance the toughness of the  $\text{Al}_3\text{Ti}$  matrix by use of rapid solidification technology and to augment the toughness of the composite by use of SCS-6 filaments.

Prior efforts were successful in generating the first HIP map for the consolidation of monolithic  $\text{Al}_3\text{Ti}$ , Figure 3[23]. Although the HIP map should be considered preliminary, it unambiguously illustrates that the HIP consolidation of  $\text{Al}_3\text{Ti}$  must be conducted at high pressures and at temperatures above 0.85 of homologous temperature. The same work examined the HIP consolidation of an  $\text{Al}_3\text{Ti}$  matrix SCS-6 fiber reinforced composite. However, HIP consolidation of IMCs is far more complicated than the consolidation of monolithic alloy powders. Careful consideration must be given as to how to achieve full (or optimal) density without degrading the properties of the intermetallic matrix or the ceramic reinforcement. In general, the temperature and pressure must be sufficiently great to consolidate the matrix, but low enough to minimize fiber-matrix reactions and inhibit fiber plasticity. In addition, in order to avoid deleterious residual stresses, careful consideration must be given to differences in thermal expansivities of the composites constituent phases. Temperature-pressure-time processing profiles must be employed minimizing thermally induced stresses.

In addition,  $\text{Al}_3\text{Ti}$  is a line compound that is stable over a narrow range of compositions. Excess aluminum was found to be extremely detrimental. Typically, the HIP consolidation temperature for  $\text{Al}_3\text{Ti}$  is approximately 400 °C above the melting temperature of pure aluminum. Any residual aluminum melts and wicks along the fiber, where it reacts with both the fiber and the matrix.

In order to curtail the possibility of this type of reaction, alloying additions were considered which expand the range of compositional stability. Figure 4, is an isothermal section of the Al-Ti-Nb equilibrium phase diagram at 1273K. Niobium forms  $\text{Al}_3\text{Nb}$  which is isostructural with  $\text{DO}_{22}$   $\text{Al}_3\text{Ti}$ ; consequently, Nb readily substitutes for Ti forming  $\text{Al}_3(\text{Ti}_x\text{Nb}_{x-1})$ . In addition, the compositional range over which it is stable is dramatically increased.

**Oxidation**

The environmental oxidation of titanium aluminides at high temperatures is dominated by reaction kinetics rather than equilibrium thermodynamics. This is because the activity of oxygen in air is fixed, the supply of oxygen is virtually unlimited, and metal oxides are typically thermodynamically more stable than metals. Oxidation kinetics are related to a large number of variables. The diffusion rates of oxygen, metal, electrons, and vacancies are significant. Scale chemistry, crystal structure, morphology, and scale adherence are also important.

The rate of oxidation is typically classified as logarithmic, linear, or parabolic [24, 25]. Logarithmic oxidation is generally observed at temperatures below 400 °C. Oxidation is initially very rapid but drops off to negligibly small values.  $\text{Al}_2\text{O}_3$  growth on aluminum at room temperature is an example of logarithmic oxidation. Linear oxidation behavior is constant with time and thus independent of the quantity of gas or metal previously consumed in the reaction. Linear oxidation is dominated by surface or phase boundary processes. Parabolic oxidation is typically observed at high temperatures and indicates that a thermal diffusion processes is rate-determining.

Mass transport in polycrystalline materials may also be dominated by diffusion along grain boundaries and other short-circuit paths of low diffusion resistance. The activation energy for grain boundary diffusion is approximately 0.5 to 0.67 that for lattice diffusion, and  $D_{gb}/D_l$  approaches  $10^5$ . However, since the grain boundary area amounts to only 5-10% of the total oxide area, these diffusion mechanisms only become significant at homologous temperatures below  $0.6T_{mp}$  [25]. Application of this rule-of-thumb to polycrystalline  $\text{Al}_2\text{O}_3$  and  $\text{TiO}_2$  scales suggests that short-circuit mechanisms may become significant below 1120 °C and 920 °C respectively.

**Oxidation of Titanium:** Thermodynamically, the oxidation of titanium should result in layers of different titanium oxides scales, viz.,  $\text{TiO}$ ,  $\text{Ti}_2\text{O}_3$ ,  $\text{Ti}_3\text{O}_5$ , and  $\text{TiO}_2$ . However, in investigations of the oxidation behavior of titanium below 1000 °C, only  $\text{TiO}_2$  has been observed [25]. The rate at which titanium oxidizes also follows different rate equations depending on temperature. Below 400 °C, Ti oxidizes logarithmically; cubic oxidation is observed between 400 and 600 °C. Parabolic oxidation dominates at temperatures between 600 °C and 1000 °C, while linear oxidation is observed above 1000 °C.

**Oxidation of Aluminum:** Although elemental aluminum melts at 660 °C, a temperature well below where the oxidation of titanium aluminides occurs, it is instructive to examine aluminum's oxidation response. Aluminum is known to form a tenacious, protective oxide layer. At room temperature, aluminum oxidizes logarithmically and an amorphous oxide layer 2 nm to 3 nm thick forms after about an hour[24]. Further oxidation at room temperature is negligible. Kim et al. [26] found that the amorphous oxide was triple hydrated, i.e.,  $\text{Al}_2\text{O}_3 \cdot 3\text{H}_2\text{O}$ . Heating the aluminum at temperatures below 300 °C, caused the decomposition of this compound into  $\text{Al}_2\text{O}_3 \cdot \text{H}_2\text{O}$  and the release of  $\text{H}_2\text{O}$ . At temperatures above 300 °C, the adsorbed moisture reacts with aluminum forming additional  $\text{Al}_2\text{O}_3$  and hydrogen. At temperatures above 300 °C, aluminum oxidizes parabolically; however, at 500 °C to 550 °C a linear plot fits experimental data better. At still higher temperatures, the amorphous oxide crystallizes forming polycrystalline gamma- $\text{Al}_2\text{O}_3$ .

**Titanium Aluminides:** In addition to their excellent specific mechanical properties, some titanium aluminides also possess good oxidation resistance. A number of studies have been conducted to determine the oxidation properties of titanium aluminides[27-37]. The oxidation behavior of titanium aluminides has been shown to be composition dependent. Protective  $\text{Al}_2\text{O}_3$  oxide scales are reported to form only when the Al content of TiAl exceeds 57% [35]. McKee and Huang [27] also examined the cyclic oxidation behavior of Ti-Al-X-Y alloys at temperatures between 850-900 °C. Oxidation resistance was found to increase with aluminum content and with the additions of Nb and W. Additions of less than 4% Cr decreased oxidation resistance; however, Cr additions of greater than 8% improved oxidation resistance. This oxidation response was explained in terms of reduced Ti activity. As  $\% \text{Ti} / (\% \text{Al} + \% \text{X} + \% \text{Y})$  decreases, oxidation resistance increases.

**Titanium Trialuminides:** The oxidation response of cast  $\text{Al}_3\text{Ti}$  has been examined by Smialek and Humphrey [31]. They observed parabolic oxidation, controlled by alpha  $\text{Al}_2\text{O}_3$  formation, at temperatures greater than 1000 °C. Anomalously high oxidation rates were observed at short times at temperatures below 1000 °C. This was explained in terms of the internal oxidation of aluminum which had partitioned during solidification.

The efficacy of titanium trialuminide coatings for gamma and alpha two titanium aluminides was studied by Subrahmanyam [29, 30].  $\text{Al}_3\text{Ti}$  coatings on Ti-14Al-24Nb decreased cyclic oxidation weight gains by at least a factor of 10. Work by Umakoshi, et al [28], and Hirukawa, et al, [34] showed that

the oxidation rate of bulk  $\text{Al}_3\text{Ti}$  is lower than that of bulk  $\text{TiAl}$  by at least a factor of 30 at  $1000^\circ\text{C}$ .

The greater oxidation resistance of  $\text{Al}_3\text{Ti}$  compared to the lower aluminides is due in part to the tendency for aluminum to oxidize internally in the lower aluminides. This results from an insufficient flow of aluminum atoms toward the surface, and the rapid diffusion of oxygen through the aluminide [37]. Wagner has theorized that the aluminum content of the aluminide must exceed a certain critical value,  $N_{\text{Al}}^{\text{crit}}$ , in order to prevent this internal oxidation, Eq 1 [37, 36, 38].

$$N_{\text{Al}}^* = \left( \frac{\pi g^* N_o D_o V_M}{2v D_{\text{Al}} V_{\text{ox}}} \right)^{1/2} \quad (1)$$

Where  $N_o$  is the solubility of oxygen in the alloy,  $D_o$  and  $D_{\text{Al}}$  are the diffusivities of oxygen and aluminum in the alloy,  $V_M$  and  $V_{\text{ox}}$  are the molar volumes of the alloy and oxide,  $v$  is the oxygen/metal ratio of the oxide, and  $g^*$  is the critical volume fraction of oxide to form a healing layer. Perkins, et al, [37] have found this value to be about 59% for  $\text{TiAl}$ .

The excellent oxidation resistance of  $\text{Al}_3\text{Ti}$  is also attributable in part to the nature of the  $\text{TiO}_2/\text{Al}_2\text{O}_3$  oxide layer which forms.  $\text{Al}_2\text{O}_3$  forms a dense, protective layer, which serves as a diffusion barrier against further oxidation.  $\text{TiO}_2$ , on the other hand, forms a porous layer of crystals which is only partially protective, and tends to spall. Thus the higher the aluminum content of the aluminide is, the higher the  $\text{Al}_2\text{O}_3$  content of the oxide will be, and the more protective the oxide layer will be against continued oxidation.

## EXPERIMENTAL PROCEDURE

### Materials Processing

**Composite Processing:** The four aluminum rich intermetallic alloys listed in Table 2 were considered for use as composite matrix materials. High purity elemental aluminum, niobium, and titanium were used in sample preparation. The preparation of cast and melt spun ribbon were both accomplished using a Marko Materials Model 2T Melt Spinner, Figure 5. Before melt-spinning, the entire chamber was cleaned by vacuuming then wiping clean with acetone. The chamber was then evacuated to 100 millitorrs by a mechanical



pump. A diffusion pump was then used to obtain a pressure of  $1 \times 10^{-5}$  torr. Laboratory grade Argon was then fed into the chamber until a pressure of 5 psia was obtained. This purging process was repeated two times to minimize the amount of oxygen in the chamber. After the final purge, an arc was struck to melt the materials. The castings, weighing 0.25 to 0.35 Kg, were prepared in a water cooled copper hearth by arc melting. The power was controlled from a DC power generator rated at 44 volts/1000 amps. After the ingot was melted for the third time, the hearth was tilted allowing the molten metal to be extracted by a rapidly spinning molybdenum wheel. The molybdenum wheel is 254 mm in diameter and rotated at a speed of 1500 rpm (approximately  $27 \text{ ms}^{-1}$ ). The melt spun ribbon produced in this manner was comminuted into powder using a hammer mill.

**Table 2. Alloy Compositions, Wt.%**

<u>Alloy</u>	<u>Aluminum</u>	<u>Titanium</u>	<u>Niobium</u>
1.	62.8	37.2	0.0
2.	60.7	32.3	7.0
3.	58.7	27.8	13.5
4.	55.1	19.6	25.3

Three fibers were examined in this work, Table 3.

**Table 3 Types of Fiber Investigated**

<u>Designation</u>	<u>Name</u>	<u>Composition</u>	<u>Diameter</u>
A	Titanium Diboride	CVD $\text{TiB}_2$ on Mo Core	120 $\mu\text{m}$
B	SCS-6	CVD $\beta\text{-SiC}$ on a Carbon Core	140 $\mu\text{m}$
C	Saphikon	Single Crystal sapphire ( $\text{Al}_2\text{O}_3$ )	20 $\mu\text{m}$

The composite test matrix is presented in Table 4. Alloys one and three were selected for fabrication into composites. The alloy powders and fibers were encapsulated in cylindrical titanium cans (approximately 25 mm in diameter by 120 mm long). The canisters were then hot vacuum degassed (one hour at 400°C), sealed, and helium leak checked. The materials were consolidated in a computer controlled Autoclave Manufacture Hot Isostatic Press (HIP) for six hours at a pressure of 172 MPa.

**Table 4 Composite Test Matrix**

Designation	Matrix	Fiber	Consolidation Temp.
1A-001	Al <sub>3</sub> Ti	TiB <sub>2</sub>	1100 °C
1A-002	Al <sub>3</sub> Ti	TiB <sub>2</sub>	1200 °C
3A-001	Al <sub>3</sub> Ti + Nb	TiB <sub>2</sub>	1100 °C
3A-002	Al <sub>3</sub> Ti + Nb	TiB <sub>2</sub>	1200 °C
1B-001	Al <sub>3</sub> Ti	SCS-6	1100 °C
1B-002	Al <sub>3</sub> Ti	SCS-6	1200 °C
3B-001	Al <sub>3</sub> Ti + Nb	SCS-6	1100 °C
3B-002	Al <sub>3</sub> Ti + Nb	SCS-6	1200 °C
1C-001	Al <sub>3</sub> Ti	Saphikon	1100 °C
1C-002	Al <sub>3</sub> Ti	Saphikon	1200 °C
3C-001	Al <sub>3</sub> Ti + Nb	Saphikon	1100 °C
3C-002	Al <sub>3</sub> Ti + Nb	Saphikon	1200 °C

### **Microstructural Characterization**

**Optical Microscopy:** The wrought alloys were mounted in dial-phthalate. The mounted specimens were hand polished on successively finer grades of abrasive paper, i.e. 220, 320, 500, and 1000 grit. The samples were lapped using 0.3 and 0.05 micron alumina slurries. A Nikon metallograph was used to examine the microstructures of the alloys and composites

**Scanning Electron Microscopy/Energy Dispersive Spectroscopy:**

Specimens were examined using an AMRAY 1000A or an AMRAY 1000B scanning electron microscope (SEM) operated at 20kV. In order to prevent feature charging and enhance resolution, SEM and energy dispersive spectrometry (EDS) specimens were coated with carbon using a Denton DV502 Vacuum Evaporation System. Compositional analysis was performed at 15-20kV using a Kevex Model 8000 EDS utilizing an ultra-thin window made of aluminum-coated parylene. Compositional analysis was accomplished comparing spectra obtained from area analysis with point analysis of the matrix and second phase particles.

**X-ray Diffraction:** X-ray diffraction (XRD) was used to identify the phases present in the melt spun ribbon, cast alloys and HIPed materials. X-ray analysis was performed on a Rigaku DMAX-B x-ray unit equipped with a  $\theta/2\theta$  goniometer and a graphite monochromator. X-rays were generated using a copper tube operating at 40KV and 30ma. The scan rate was 0.5 °/min and data was collected every 0.04 degrees.

**Differential Thermal Analysis:** A Du Pont 910 thermal analysis system equipped with a 1600°C Differential Thermal Analysis (DTA) cell was used to investigate phase changes occurring in the alloys. The calorimeter was calibrated using pure aluminum, titanium and niobium. Approximately 2g of each matrix alloy was heated from room temperature to 1600°C at 20°C per minute in a dry helium atmosphere.

**Oxidation**

The fiber reinforced intermetallic matrix composites exhibited a great deal of porosity and matrix cracking. This cracking prevented an accurate determination of the intrinsic oxidation response of the material. Therefore, in order to obtain an indication of how the composite would respond, the  $Al_3Ti$  matrix material was examined along with control specimens of TiAl and a  $L_{12}$  trialuminide,  $Al_5CuTi_2$ . The compositions of these alloys are shown in Table 5.

**Table 5 Alloy Compositions (wt,%) - Oxidation Evaluation**

Alloy	Titanium	Aluminum	Copper
AlTi	64.0	36.0	----
$Al_3Ti$	37.2	62.8	----
$Al_5CuTi_2$	32.6	45.9	21.6

**Cyclic Oxidation:** Cyclic oxidation tests were performed in order to determine the effects of rapid thermal cycling on the oxidation properties of potential matrix materials. Each test consisted of 144 or more thermal cycles. Oxidation tests were performed on all alloys in both the as-cast and the HIPed conditions at 900°C and 1100°C in air. Cycles consisted of a rapid heat-up (500 °C/min) to temperature, a 55 minute hold at temperature, and a rapid cool-down outside the furnace for 5 minutes. An ATS 3310 furnace was used for the tests; an apparatus designed and constructed by the authors was employed to move the specimen in and out of the furnace. Weight gains were measured using a Sartorius microbalance having a precision of ±0.01 mg.

**Isothermal Oxidation:** Isothermal oxidation tests were performed to determine the oxidation kinetics associated with each of the alloys in Table 5 at a constant temperature in air. Tests were performed on both the as-cast and the HIPed materials 900°C, 1000°C, and 1100°C. Isothermal oxidation experiments were conducted in a CM Rapid Temp furnace. Specimen weight was measured with a precision of ±0.01 mg every 24-hours for a period of 144 to 196 hours.

### **Thermodynamics**

Thermodynamic evaluation of the chemical activity of titanium and aluminum in Al<sub>3</sub>Ti was performed. In order to better understand the oxidation behavior of Al<sub>3</sub>Ti and Al<sub>3</sub>Ti-fiber interactions, it was important to know the chemical activity of Ti and Al. The activity of aluminum is readily estimated using Rault's Law and is for all practical purposes considered to be unity. Swalin [39] provides a means of estimating the activity of an element in an intermediate phase, Eq 2.

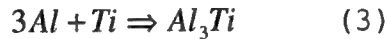
$$a_T = \exp \left[ \frac{(1-x)\Delta G_f^\circ}{(b-x)RT} \right] \quad (2)$$

where  $a_T$  is the activity of titanium,  $X$  is the maximum solubility of titanium in elemental aluminum,  $b$  is 0.25 for Al<sub>3</sub>Ti,  $R$  is the gas constant,  $T$  is temperature in K, and  $\Delta G_f^\circ$  is the free energy of formation of Al<sub>3</sub>Ti. Nonlinear regression analyses was performed using the experimental solubility data obtained from (St. John, and Massalaski) [3,40] in order to obtain equations for the maximum solubility of titanium in liquid and solid aluminum.

Phase stability diagrams were generated for the Ti-O-C, Al-O-C, and Si-O-C systems. This was accomplished by equating the free energies of formation for each of the possible

phases and solving for the natural logs of carbon and oxygen.

The standard free energy of formation for  $\text{Al}_3\text{Ti}$  (3) was calculated from known thermodynamic quantities of the products and reactants (e.g., specific heat, heats of formation, latent heats of formation) using equation 4.



$$\Delta G_{298}^o = \Delta H_{298}^o + \int_{T_0}^{T_1} \Delta C_p dT - T \Delta S_{298}^o - T \int_{T_0}^{T_1} \frac{\Delta C_p}{T} dT \quad (4)$$

## EXPERIMENTAL RESULTS

### Optical Metallography

Optical micrographs of the composite materials are presented in Figures 6 - 10. In general, the fibers were preferentially located in the ubiquitous matrix cracks. The most severely attacked fibers were the SCS-6. The  $\text{TiB}_2$  fibers did not appear to react extensively; however, extensive fiber cracking was observed. The Saphikon fibers withstood the HIP consolidation process best although heavy pitting was observed when consolidated at 1200 °C.

Composites with  $\text{TiB}_2$  fibers are presented in Figures 6 & 7. Circumferential cracks can be seen at the fiber-matrix interface and at the Mo core-CVD  $\text{TiB}_2$  interface. Radial cracks passing through the fibers are also clearly visible. Alloying does not appear to affect the microstructure of the HIP processed fiber, compare Figures 6a & 6b and 7a & 7b. At 1200 °C, fiber cracking appears somewhat more severe than at 1100 °C.

SCS-6 fibers show extensive reaction with the matrix materials. No SCS-6 fibers were found in the  $\text{Al}_3\text{Ti}$  matrix materials. The remnants of SCS-6 fibers were found in the  $\text{Al}_3\text{Ti} + \text{Nb}$  matrix materials, Figure 8. At 1100 °C, the fibers have an onion skin appearance. The carbon core of the fiber is no longer visible. Large cracks are observed passing through the fiber as well as around the fibers. At 1200 °C, the SCS-6 fiber ceases to have a spherical cross section. A diffuse inner region is surrounded by a blocky interphase region.

Optical micrographs of the saphikon fibers reinforced composites are presented in Figures 9 & 10. The composition of the matrix material appears to have little impact on the

microstructure. Fibers are preferentially located in matrix cracks, but the cracks generally run around the fibers. Pitting is observed in the saphikon fibers processed at 1100 °C; more severe pitting is observed in the fibers processed at 1200 °C. The matrix near the fibers appears to be recrystallized with an average grain size of 7µm. Holes in the matrix appear to have the same size and shape as do the grains.

#### **Scanning Electron Microscopy-Energy Dispersive Spectroscopy:**

SEM micrographs and representative energy dispersive spectrographs (EDS) of the  $\text{Al}_3\text{Ti}/\text{TiB}_2$  composites are presented in Figures 11 & 12. Matrix cracks are observed near the  $\text{TiB}_2$  fibers, Figure 11a. The cracks appear to emanate from the fibers. There is a significant amount of porosity in the matrix and which seems to be concentrated near the fiber. Radial cracks in the fiber are observed. The Mo core material has been partially extruded into the crack.

EDS analysis of the material filling the cracks in the  $\text{TiB}_2$  fibers shows the presence of both aluminum and molybdenum. The concentration of aluminum decreases approaching the fiber core. The concentration of molybdenum decreases with distance from the core. (Figure 11b.) The core of the  $\text{TiB}_2$  fiber has a ringed appearance. The concentration of molybdenum within the center of the fiber core is more intense than at the edges of the core, Figure 11c.

The composite HIPed at 1200 °C, displayed more matrix cracking and micro-porosity than the material HIPed at 1100 °C. The matrix also exhibited an unusual cross-hatched appearance. Composites processed at the higher temperature exhibit more fiber and fiber-matrix damage, Figure 12. The core of the  $\text{TiB}_2$  fibers HIPed at 1200 °C did not exhibit the ring structure observed in the  $\text{TiB}_2$  fibers HIPed at 1100 °C.

The  $\text{Al}_3(\text{Ti}, \text{Nb})/\text{TiB}_2$  composites also exhibit extensive matrix and fiber cracking, Figure 13. Matrix porosity and fiber splitting is observed. The ringed structure of the  $\text{TiB}_2$  core is not observed at either processing temperature, Figure 14. The matrix exhibits spherical regions having a dendritic type microstructure.

Extensive fiber-matrix reaction is observed in the composites containing SCS-6 fibers, Figures 15 & 16. Remains of the fibers are surrounded by aluminum-rich regions, Figure 15b. Evidence of aluminum infiltration into the fiber is also apparent. Although the reacted fiber has

retained the approximate size and shape of the original fiber, it has undergone extensive chemical disintegration.

EDS results indicate that after HIPing the SiC fiber becomes titanium-rich, Figure 15c. Nearly pure aluminum region are observed surrounding the fibers. The matrix microstructure exhibits a finely distributed cross-hatched appearance. The effect of increasing the HIP processing temperature is to cause even further fiber-matrix reaction, Figure 16.

As seen in Figure 17, alloying caused reactions between the SCS-6 fibers and the matrix to decrease. Fibers retained their circular shape but have deteriorated completely resulting in a porous appearance. Increasing the HIPing temperature resulted in crystallographic reactions within the fibers, Figure 18.

Neither the  $\text{Al}_3\text{Ti}$  nor the  $\text{Al}_3\text{Ti} + \text{Nb}$  matrix composites containing saphikon fibers exhibited optical or SEM evidence of fiber-matrix reactions, Figures 19. EDS analysis of the fiber, matrix, and the fiber-matrix interface could not discern chemical variations from the nascent materials, Figures 20.

Although the fiber and the matrix did not react chemically and remained intact at both consolidation temperatures, the matrix was cracked and the fiber sustained pitting damage. Increasing the HIPing temperature, was found to promote fiber pitting.

Table 6 Summary of Fiber-Matrix Interactions

Fiber	1. $\text{Al}_3\text{Ti}$	3. $\text{Al}_3\text{Ti} + \text{Nb}$
$\text{TiB}_2$	The fiber split radially. Al diffused inwardly. Mo diffused outwardly.	The fiber was severely cracked. Evidence of a transient liquid phase was observed.
SCS-6	Extensive fiber-matrix reaction. The fiber reacts forming a silicide. Nearly pure Al surrounded the fibers.	Less fiber-matrix reaction occurs than with the $\text{Al}_3\text{Ti}$ matrix. The fiber-matrix interface is very porous
Saphikon	No evidence of fiber-matrix reactions. Matrix cracked and full of holes.	No evidence of fiber-matrix reactions. Matrix cracked and full of holes.

### X-Ray Diffraction

Using the Joint Committee on Powder Diffraction Standards (JCPDS) published data as a control, the x-ray diffraction

patterns for the melt-spun powders were examined. Figure 21 represents the diffraction patterns for the melt-spun powders. Diffraction patterns for melt spun  $\text{Al}_3\text{Ti}$  and JCPDS powders were identical. All of the "d" distances were compatible, but intensity ratios varied. The addition of niobium to the alloy gave the diffraction pattern as seen in Figure 21. This diffraction pattern was compared to JCPDS's patterns for aluminum,  $\text{Al}_3\text{Ti}$  and  $\text{Al}_3\text{Nb}$ . The patterns for  $\text{Al}_3\text{Ti}$  and  $\text{Al}_3\text{Nb}$  are almost identical with the exception of a few distances. Notice the small amount of aluminum that is identifiable in the diffraction pattern.

### Differential Thermal Analysis

From the DTA analysis, it was determined that the melting temperature of  $\text{Al}_3\text{Ti}$  and  $\text{Al}_3\text{Ti} + \text{Nb}$  was approximately  $1475^\circ\text{C}$  [see Figure 22]. As seen in the DTA analysis, at  $660^\circ\text{C}$  (the melting temperature of aluminum) there is a small endothermic peak. Upon cooling and reheating the same sample, the aluminum peak disappeared. This is evidence of inhomogeneity and the ability of aluminum to go into solution upon reheating.

### Oxidation

**Cyclic Oxidation:** The results of the cyclic oxidation tests of  $\text{AlTi}$ ,  $\text{Al}_3\text{Ti}$ , and  $\text{Al}_5\text{CuTi}_2$  are presented in Figures 23-26.

**AlTi:** The oxidation weight gains for this alloy are shown in Figure 23. Weight gain is linear at both  $900^\circ$  and  $1100^\circ\text{C}$ . At  $900^\circ\text{C}$  the weight gain is about  $0.3 \text{ mg/cm}^2/\text{hr}$ , while that at  $1100^\circ\text{C}$  is about  $2.6 \text{ mg/cm}^2/\text{hr}$ . At both temperatures, large volumes of yellow and white oxides were produced, and flaked off during each cool-down cycle. An oxidized specimen is shown in Figure 24a.

**Al<sub>3</sub>Ti:** Cyclic weight gains for this alloy are shown in Figure 25. At  $1100^\circ\text{C}$ , weight gain is initially parabolic, but overall is in between linear and parabolic. Average weight gain over 206 hours is  $0.04 \text{ mg/cm}^2/\text{hr}$ , or about  $1/60$  that for  $\text{AlTi}$ . At both temperatures, the oxide product is pale gray and powdery, and non-uniformly distributed, Figure 24c.

**Al<sub>5</sub>CuTi<sub>2</sub>:** The oxidation weight gains for this alloy are shown in Figure 26. At  $900^\circ\text{C}$ , weight gain is roughly oxidation averages about  $0.02 \text{ mg/cm}^2/\text{hr}$  over 168 hours. At  $1100^\circ\text{C}$ , the behavior is quite different. After an initial low weight gain, the specimen appeared to "ignite", turning black and releasing a considerable amount of gas. The



weight increased by as much as  $30 \text{ mg/cm}^2/\text{hr}$  as the entire specimen was consumed. Figure 24b shows the appearance of the specimen after complete oxidation at  $1100^\circ\text{C}$ . Initially, the oxide appearance is similar to that in the  $\text{Al}_3\text{Ti}$  alloy, but after "ignition" turns dark brown to black, crusty, and deeply cracked.

**Isothermal Oxidation:** The results of the isothermal oxidation response of  $\text{AlTi}$ ,  $\text{Al}_3\text{Ti}$ , and  $\text{Al}_5\text{CuTi}_2$  are presented in Figures 27-29.

**AlTi:** Oxidation weight gain of this alloy under constant temperature conditions is shown in Figure 27. At both  $900^\circ$  and  $1100^\circ\text{C}$ , the weight gain appears to be parabolic, in contrast to the alloy's linear oxidation under cyclic conditions. The oxide product is thick, yellow, and adherent, and essentially free of visible cracks. Some cracking and spalling did occur, however, upon cooling to ambient temperature.

**Al<sub>3</sub>Ti:** Isothermal weight gains for this alloy are shown in Figure 28. As in cyclic oxidation, weight gains are very low, averaging about  $0.06 \text{ mg/cm}^2/\text{hr}$  over 168 hours, and are between linear and parabolic. The appearance of the oxide product is similar to that in the cyclic tests.

**Al<sub>5</sub>CuTi<sub>2</sub>:** Weight gains for this alloy are shown in Figure 29. At  $900^\circ\text{C}$ , the isothermal oxidation behavior is very similar to the cyclic behavior, with similar weight gains and roughly parabolic behavior. At  $1100^\circ\text{C}$ , as in the cyclic tests, weight gain was initially low, followed by a sudden "ignition", or rapid decomposition. Unlike the cyclic tests, though, in the isothermal tests the "ignition" of the specimen also resulted in the release of molten copper, which turned the entire alumina crucible dark brown.

**Effects of HIPing on Oxidation:** The purpose of HIPing the cast alloys was to reduce the level of porosity and micro cracking present. Both of these types of defects are believed to promote enhanced oxidation, and so HIPing was expected to decrease oxidation weight gains as compared to the as-cast condition. However, the as-cast specimens revealed a wide variation in surface quality and porosity, and this appears to have affected the oxidation properties much more than the changes produced by subsequent HIPing. The effectiveness of HIPing to reduce surface oxidation is therefore unclear.

**Thermodynamic Evaluation**

**Titanium Solubility:** The experimental solubility data of titanium in aluminum obtained from (St. John, and Massalaski)[40,3] is plotted in Figure 30. The results of the nonlinear regression analyses of the data are given in Eq 5 & 6, and in Figure 30.

$$X_{Ti(sat)}^{solid} = 1.92 \exp\left(\frac{-5,314}{T}\right) \quad (5)$$

and

$$X_{Ti(sat)}^{liq} = 475 \exp\left(\frac{-11,976}{T}\right) \quad (6)$$

**Standard Free Energy of Formation for Al<sub>3</sub>Ti:**

Equations 5,6,&7 were used to calculate the free energy of formation for Al<sub>3</sub>Ti using Cp, enthalpy, and entropy data gathered from the literature. The free energy of formation for Al<sub>3</sub>Ti was fit to equations having the form of

$$\Delta G^\circ = A + BT$$

where A and B are coefficients and T is temperature in K. These quantities are presented in Table 7.

**Table 7 Thermodynamic Constants for the Formation of Al<sub>3</sub>Ti.**

Temperature, K	-A x 10 <sup>-3</sup>	B
298-933	41.7	-0.0082
933-1155	49.9	8.83
1155-1473	50.7	9.54

**Titanium Activity in Aluminum-Rich Al<sub>3</sub>Ti:** The calculated activities are presented in Figure 31.

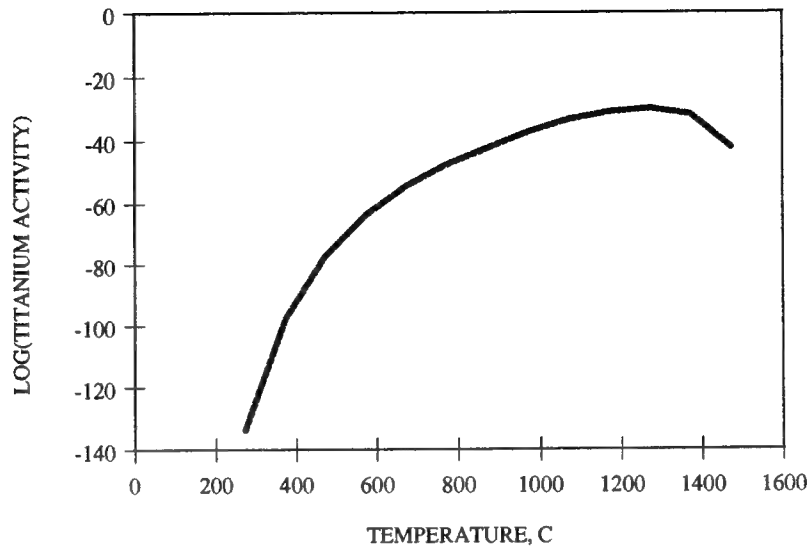


Figure 31 - The calculated activity of titanium in  $\text{Al}_3\text{Ti}$ .

The change in free energy associated with dissolving one mole of titanium into a dilute solution may be estimated by taking the log of Eq. 5 & 6. The quantity inside the exponential term is associated with the enthalpy and the coefficient is associated with the entropy term Eq. 7, Table 8.

$$\ln(X) = \frac{\Delta \bar{S}}{R} - \frac{\Delta \bar{H}}{RT} \quad (7)$$

Table 8 The Estimated Enthalpy and Entropy Associated with the Dissolution of Titanium in a Dilute Solution.

Temperature, K	$\Delta \bar{H}$ (cal/mol)	$\Delta \bar{S}$ (cal/mol)
<933	-11,00	3.8
>933	-24,00	943

The phase stability diagrams are presented in Figures 32 & 33.

**DISCUSSION OF RESULTS****Fiber-Matrix Thermal Expansion Mismatch**

Differences in the coefficients of thermal expansivities (CTE) of the matrix and fiber materials result in internal strains and stresses being generated during HIP processing. If the fiber and matrix are well bonded, the matrix and fiber strains may be assumed equivalent. The strains in the matrix and fiber are due to thermal expansion and applied stress, Eq 8.

$$\alpha_m \Delta T + \frac{\sigma_m}{E_m} = \alpha_f \Delta T + \frac{\sigma_f}{E_f} \quad (8)$$

Further, since the volume fraction of fiber is negligible in the composites investigated, the average stress in the matrix may be considered negligible and the equation simplifies to

$$\sigma_f = E_f (\alpha_m - \alpha_f) \Delta T \quad (9)$$

Fiber stress is a function of fiber modulus, the difference in fiber-matrix CTE, and the change in temperature.

Following HIP consolidation at either 1100 °C or 1200 °C, all the materials were cooled to room temperature. During cooling, thermal stresses are induced in both the fiber and matrix. At temperatures above 800 °C, the strength of the matrix drops precipitously and can not effectively transfer loads to the fiber. Therefore, above 800 °C, thermally induced stresses may be safely ignored. The calculated fiber stress (compressive) induced upon cooling after HIP consolidation are compared with handbook values of fiber strength in Table 9. In all cases, the fiber stress approaches that of its theoretical UTS. Although this may result in some fiber damage, it seems unlikely that the observed fiber cracking is due to fiber-matrix CTE mismatch.

Table 9 Estimated HIP Processing Induced Fiber Stress.

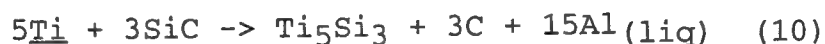
Property	Saphikon	TiB <sub>2</sub>	SCS-6
Matrix CTE (x 10 <sup>6</sup> /°C)	15	15	15
Fiber CTE (x 10 <sup>6</sup> /°C)	9	8	4.8
Fiber Modulus (GPa)	448	448	428
Fiber Stress (GPa)	2.1	2.5	3.4
Fiber UTS (GPa)	2.1-3.4	2.1-3.4	3.4-4.1

**SCS-6/Matrix Interactions:** HIP processing results in extensive degradation of the SCS-6 fibers. Chemical attack of the fiber is not confined to an interphase layer, but results in a total fiber metamorphosis. SiC is replaced with titanium silicide and the fiber is enveloped in elemental aluminum. A partial list of possible reaction products is provided in Table 10.

Table 10 Possible Reaction Products for Al<sub>3</sub>Ti/SCS-6

TiC	Ti <sub>5</sub> Si <sub>3</sub>	Al
Ti <sub>2</sub> C	TiSi	Si
Ti <sub>3</sub> AlC	TiSi <sub>2</sub>	<u>Si</u>
Al <sub>4</sub> C <sub>3</sub>	Ti <sub>x</sub> Si <sub>y</sub>	C

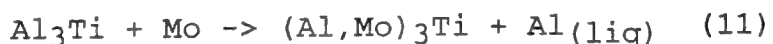
A chemical reaction consistent with the observed microstructure is provided in Eq 10.



Examination of the Richardson diagrams for the formation of metal carbides reveals that SiC is a weak carbide former and readily reduced by Ti. The free energy of formation of Al<sub>4</sub>C<sub>3</sub> is comparable to that of SiC; and is therefore also unstable in the presence of Ti. Ti<sub>5</sub>Si<sub>3</sub> is a potent silicide former and is believed to form in preference to TiC. Note too, that for each mole of silicide formed 15 moles of aluminum are liberated. This accounts for the observed elemental aluminum surrounding the fibers.

**TiB<sub>2</sub>/Matrix Interactions:** Optical and SEM/EDS examination of TiB<sub>2</sub> reinforced composites did not reveal Al<sub>3</sub>Ti-TiB<sub>2</sub> reaction products. However, the core of the CVD fiber is molybdenum which can and does interact with the matrix. Matrix-molybdenum contact occurs as the result of radial splits in the CVD TiB<sub>2</sub> fiber. Splits in the fiber may be the result of differences in their CTE's: the CTE of TiB<sub>2</sub> is  $8 \times 10^{-6}/^{\circ}\text{C}$  and that of molybdenum is  $5 \times 10^{-6}/^{\circ}\text{C}$ .

EDS indicates that aluminum has diffused into the molybdenum core and that molybdenum has diffused into the matrix, Figure 11. This is most likely the result of molybdenum substituting for aluminum in Al<sub>3</sub>Ti and liberating aluminum.



Most transition element such as Cu, Ni, Fe, Cr, are believed to substitute for titanium in the Al<sub>3</sub>Ti lattice. Molybdenum is believed to be the exception and capable of substituting on both lattice sites [4].

**Saphikon/Matrix Interactions:** Optical and SEM/EDS examination of Saphikon reinforced composites revealed no chemical reaction products, Figures 19 & 20. The only possible reaction, Eq 12, of saphikon with Ti in solution is to form a titanium oxide and elemental aluminum is not energetically favorable. Therefore, the system may be considered thermodynamically stable.



Matrix cracking of this system is extensive. Fibers invariably are located at matrix cracks. Matrix cracking is most likely attributable to thermally induced stress as a result of differences in fiber-matrix thermal expansivities.

## Oxidation

Cyclic and isothermal oxidation tests provide a qualitative comparison of the oxidation properties of Al<sub>3</sub>Ti-based materials and similarly processed  $\gamma$ -TiAl. In this analysis, oxidation is assumed to proceed according to the equation:

$$W^n = kt + C \quad (13)$$

where W is the weight gain per unit area after time t, and k is the rate constant. The units for k are  $(\text{mg}/\text{cm}^2)^n/\text{sec}$ . The n-exponent depends upon the mechanism which controls the oxidation rate; n=1 represents linear or interface-controlled oxidation, n=2 is parabolic or diffusion-limited oxidation, and 3 represents some form of exponential

behavior, such as oxidation controlled by grain-boundary diffusion.

The oxidation of these materials was assumed to follow an Arrhenius-type temperature dependence, wherein

$$k = A \exp(-Q/RT) \quad .(14)$$

where A is a constant and Q is the activation energy for the rate-controlling process. By plotting  $\ln(k)$  as a function of  $1/T$ , a straight line whose slope is  $(-Q/R)$  is obtained.

### **AlTi.**

Experiments by Meier, Perkins, et al [36] indicate that Al-Ti compounds containing less than 59 atomic % (45 weight percent) aluminum do not form a continuous  $\text{Al}_2\text{O}_3$  scale, but rather a mixed  $\text{Al}_2\text{O}_3/\text{TiO}_2$  layer under an initial layer of almost pure  $\text{TiO}_2$ . This was found to be the case in these experiments on near-stoichiometric AlTi, as well.

**Cyclic Oxidation:** As can be seen from Figure 23, the cyclic oxidation behavior of AlTi is linear. During the hot portion of the cycle, the oxide formed is more or less adherent. However, upon cooling, it becomes detached and peels away due to the thermal expansion coefficient mismatch between the oxide and the AlTi, exposing the underlying AlTi to the next hot cycle. The SEM image in Figure 34 suggests that oxidation occurs through the selective oxidation of aluminum within the AlTi. This alumina formation depletes the surrounding AlTi of aluminum, eventually raising the activity of titanium high enough that the formation of  $\text{TiO}_2$  becomes thermodynamically favorable.

Table 11 shows the calculated linear rate constants for the cyclic specimens at 900° and 1100°C. Although tests were conducted at only two temperatures, the  $\ln(k)$  versus  $1/T$  plot in Figure 35 suggests an activation energy of about 34 cal/mol.K. This is about 57% of the activation energy for bulk diffusion of oxygen through  $\text{TiO}_2$ , and also very close to the activation energy for grain boundary diffusion in  $\text{Al}_2\text{O}_3$  (32 kcal/mol), suggesting that short-circuit diffusion may control oxide formation during the hot portion of the cycle. Parabolic behavior is not observed, however, due to the complete spallation of the oxide during each cooldown cycle.

**Isothermal Oxidation:** The isothermal oxidation behavior of AlTi differs from the cyclic behavior in that the oxide layer does not peel away, because no thermal cycling occurs. Therefore the oxide remains essentially adherent, and continues to grow in thickness as long as the specimen remains at temperature. The outer oxide layer is shown in the SEM image in Figure 36 to consist of islands of  $\text{Al}_2\text{O}_3$  in

a porous matrix of  $\text{TiO}_2$ . The outermost layer of the oxide is predominantly  $\text{TiO}_2$ , while thin layers within the oxide are either alumina-rich or titania-rich. These regions are believed to correspond to transient oxidation which occurred during the heat-up and cool-down cycles when the specimen was removed from the furnace for weighing.

Even with the adherent oxide, there is evidence of internal oxidation of aluminum at all test temperatures. At  $900^\circ$  and  $1000^\circ\text{C}$ , the internally oxidized zone consists of a two-phase outer region about  $10\text{ }\mu\text{m}$  thick, consisting of plates of  $\text{Al}_2\text{O}_3$  in aluminum-depleted  $\text{AlTi}$ , and a single-phase region underneath which was also found to be aluminum-deficient compared to the  $\text{AlTi}$  in unaffected areas. This lower layer may be  $\text{AlTi}_3$  or a mixture of  $\text{AlTi}_3$  and  $\text{AlTi}$ . At  $1100^\circ\text{C}$ , the internal oxidation zone consists of a two-phase outer layer containing  $\text{Al}_2\text{O}_3$  and a severely Al-depleted phase, and an inner two-phase layer in which the aluminum is depleted to a lesser degree (see Figure 34). The overall thickness of the zone is nearly  $100\text{ }\mu\text{m}$ . The  $\text{Al}_2\text{O}_3$  in the outer layer appears to form on preferred crystallographic planes within each  $\text{AlTi}$  grain.

It appears that the oxidation of  $\text{AlTi}$  begins with a brief initial transient period in which  $\text{TiO}_2$  is the major product. Thereafter, oxidation proceeds via internal oxidation of aluminum, forming plates of  $\text{Al}_2\text{O}_3$  in an increasingly aluminum-poor matrix. Meanwhile, this matrix is consumed from the outer surface inward; this explains the observed oxide morphology. The rate of titanium consumption is controlled by the rate of  $\text{Al}_2\text{O}_3$  formation, in that the formation of alumina eventually raises the activity of titanium in the  $\text{AlTi}$  to the point where  $\text{TiO}_2$  formation becomes favorable. The exponential behavior observed over a range of test times, however, indicates that the overall oxidation rate is controlled not by  $\text{Al}_2\text{O}_3$  formation, but by the inward diffusion of oxygen through the oxide. This is supported by Figure 35, which shows the activation energy for oxidation to be about  $28.8\text{ kcal/mol.K}$ , or just under half the activation energy for bulk diffusion of oxygen through  $\text{TiO}_2$ . It should be noted that Figure 35 is based on the assumption of linear kinetics. Since the true behavior is roughly parabolic, the linear rate constants shown for isothermal oxidation are not strictly valid; however, since measuring the weight gains at successive intervals required the use of multiple specimens, parabolic rate constants could only be estimated by assuming  $C$  in Equation 13 to be zero. Both linear and parabolic constants are shown in Table 11. If the estimated parabolic constants are plotted in Figure 35, an activation energy of  $57\text{ kcal/mol}$  is obtained. The rate of isothermal oxidation therefore appears to be controlled by some combination of short-circuit and bulk diffusion through  $\text{TiO}_2$ , with the latter expected to be dominant above  $920^\circ\text{C}$ .



Table 11**AlTi Oxidation Kinetics**

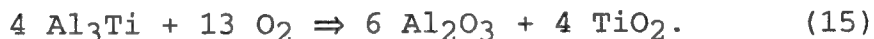
		Rate Constant k	
Temp. °C	Condition	Linear (mg/cm <sup>2</sup> hr)	Parabolic (mg <sup>2</sup> /cm <sup>4</sup> hr)
Cyclic			
900	Both	0.328	
1100	Both	2.674	
Isothermal			
900	As Cast	0.795*	16.5
	HIPed	0.852*	15.8
1000	As Cast	2.225*	119
	HIPed	1.783*	76
1100	As Cast	4.961*	625
	Hiped	5.032*	678

\* - Based upon the total weight gain after 24 hours.

Comparison of cyclic and isothermal oxidation rates reveals that initially, the isothermal condition gives a much higher oxidation rate (dW/dt). While the linear cyclic rate remains constant with time, the parabolic isothermal oxidation slows down with time because of the build-up of the protective oxide. Thus after about 24-48 hours, dW/dt is lower for the isothermal condition. The initial high isothermal rate is probably a result of the difference in heat-up rates. Whereas the cyclic specimens were heated from ambient temperature to the test temperature in about two minutes, the isothermal test furnace took about two hours to reach the test temperature. The high cyclic heat-up rate allowed the early formation of a protective Al<sub>2</sub>O<sub>3</sub> scale before much TiO<sub>2</sub> could form. This scale, along with the TiO<sub>2</sub>, spalled off during each cool-down cycle, but the early formation of alumina kept the oxidation rate relatively low. The slower isothermal heat-up rate, on the other hand, allowed more TiO<sub>2</sub> to form along with the alumina, and thus the permeability of the oxide was greater. Thus the oxide which accumulated on the cyclic specimens after one hour was as protective as that formed on the isothermal specimens after 24-48 hours.

**Al<sub>3</sub>Ti.**

Al<sub>3</sub>Ti has been noted by previous researchers for its ability to form a continuous Al<sub>2</sub>O<sub>3</sub> coating, which acts as a barrier to the diffusion of oxygen and aluminum ions. Oxidation weight gains are therefore typically assumed to follow the parabolic form of Equation 13. The oxidation behavior of Al<sub>3</sub>Ti appears to be strongly influenced by both its chemistry and the surface quality of the specimens. Thermodynamically, Al<sub>2</sub>O<sub>3</sub> is expected to form preferentially to TiO<sub>2</sub>; however, since Al<sub>3</sub>Ti is ideally a line compound, the preferential formation of Al<sub>2</sub>O<sub>3</sub> results in the formation of lower aluminides which are less oxidation resistant than Al<sub>3</sub>Ti. The oxidation of Al<sub>3</sub>Ti is therefore assumed to proceed according to the reaction:



SEM/EDS examination suggests that TiO<sub>2</sub> is not present in significant amounts in the Al<sub>2</sub>O<sub>3</sub> coating, and therefore may not contribute to diffusion processes. The lack of TiO<sub>2</sub> in the oxide may be a result of preferential Al<sub>2</sub>O<sub>3</sub> formation, due to the reduced oxygen partial pressure at the oxidizing surface, once an Al<sub>2</sub>O<sub>3</sub> layer has formed.

**Cyclic Oxidation:** Figure 37 shows cyclic oxidation data for Al<sub>3</sub>Ti at 900 and 1100°C plotted as weight gain per unit area versus (time)<sup>1/2</sup>. The slope of a straight line drawn through the data points is then equal to the parabolic rate constant  $k_p$ . Note in the figure that the slope is not constant in some cases, but rather decreases with increasing time. This suggests that either the rate constant decreases with time or the n-exponent in Equation 13 is actually greater than 2. The latter possibility will be discussed in a subsequent section. For these calculations, the former case is assumed, and  $k_p$  values are calculated based on the longer test times. These values are shown in Table 12. For cyclic oxidation, the activation energy  $Q$  was found to be about 35 kcal/mol (Figure 38), which is very close to the activation energy for short-circuit (grain boundary) diffusion of oxygen in Al<sub>2</sub>O<sub>3</sub> or TiO<sub>2</sub>. However, the oxidation rate is much too high to be explained by diffusion, as can be seen from the following calculation.

By differentiating Equation 13 with respect to time, the oxide growth rate can be determined at a particular instant:

$$dW/dt = (k/n) W^{(1-n)} \quad (16)$$

which reduces to  $dW/dt = k_p/2W$  for the parabolic case. The  $W$  in the denominator is the total weight gain per unit area up to the time in question. The weight gain can be assumed to be entirely due to the pickup of oxygen, so  $dW/dt$  can be converted into a flux of reactive ions (either oxygen diffusing inward or metal ions diffusing outward).

Diffusion data[41] suggests that at 1100°C, the fastest diffusivity possible in the  $\text{Al}_3\text{Ti}/\text{Al}_2\text{O}_3/\text{TiO}_2$  system is for bulk diffusion of oxygen through  $\text{TiO}_2$ . An upper limit for the diffusivity in the oxide coating can be obtained by assuming that the  $\text{TiO}_2$  which forms is distributed in such a way that all of the inward diffusion of oxygen occurs through that oxide. From Fick's first law,  $J = -D(dC/dx)$ , it was determined that to support the observed oxidation rates in  $\text{Al}_3\text{Ti}$  in 1100°C cycling, the concentration of diffusing oxygen ions at the outer surface of the oxide would have to be on the order of  $7 \times 10^{24}$  atoms/cm<sup>3</sup>. This is about two orders of magnitude greater than the total number of oxygen lattice sites per cm<sup>3</sup> in  $\text{TiO}_2$ , which suggests that diffusion through the oxide layer is not the limiting factor in oxide growth.

The above result can be duplicated by considering oxygen transport from the standpoint of apparent permeability  $K$ . The flux can then be given by [42]

$$J = \frac{K(P_{O_2})^m}{x} \quad (17)$$

where  $p_{O_2}$  is the atmospheric partial pressure of oxygen and  $m$  is 1.  $K$  is equal to the product of diffusivity and solubility  $S$ . Calculated values of  $K$  and  $S$  are listed in Table 12. The apparent required solubilities at both 900 and 1100°C are on the order of  $10^{25}$  atoms/cm<sup>3</sup>, which agrees well with the previous calculation. This further supports the theory that short-circuit diffusion through grain boundaries or cracks in the oxide, and not lattice diffusion, is the rate-controlling mechanism.

**Isothermal Oxidation:** Figure 39 shows weight gain per unit area versus  $(\text{time})^{1/2}$  for  $\text{Al}_3\text{Ti}$  under isothermal conditions at 900, 1000, and 1100°C. Parabolic rate constants were determined for these tests in the same manner as for the cyclic tests. These  $k_p$  values are shown in Table 12 along with calculated values of  $K$  and  $S$ . The rate constants for isothermal oxidation are slightly lower at 900°C than in cyclic oxidation, but somewhat higher at 1100°C. There is also a knee in the isothermal data at 1000°C, indicating a possible change in transport mechanism around that temperature. Below 1000°C, the activation energy is close to the value expected for grain boundary diffusion in  $\text{Al}_2\text{O}_3$ , while above 1000 °C it is close to that for bulk diffusion in alumina (see Figure 38). The observed oxidation rates, however, are still much higher than those predicted for diffusion control.

A partial explanation for the unusually high oxidation rates and rate constants can be found in the SEM micrograph in Figure 40. This image shows the outer oxide scale formed after 168 hours at 1100°C. Calculations from the weight gain data indicate that the thickness of the oxide should be 37  $\mu\text{m}$ . However, the micrograph clearly shows that the outer oxide is only 4  $\mu\text{m}$  thick. The remaining 90% of the weight gain was found to be the result of the internal oxidation of a second phase, which was identified previously as  $\alpha\text{-Al}$ , and which constitutes 2.1 volume percent of the material.[43] If it is assumed that this phase oxidizes completely, the remainder of the observed weight gain is just enough to form a surface layer 3.7  $\mu\text{m}$  thick. Similarly, the oxide coating after 24 hours at 1000°C was about 2  $\mu\text{m}$  thick, suggesting that about 22% of the second phase has oxidized.

Based on the thinner oxide coating, the previous calculations for the necessary permeabilities and solubilities would be reduced by a factor of ten. The resulting values for  $S$  are still a factor of ten higher than the overall concentration of oxygen lattice sites in  $\text{TiO}_2$ , however, indicating that the oxidation rate is still much too high to be bulk diffusion limited. If the assumption of parabolic behavior is retained, the discrepancy might be due to the imperfect structure of the oxide. The  $\text{Al}_2\text{O}_3$  scale may contain numerous cracks, pores, or other imperfections which greatly increase its permeability to oxygen.

It can be seen from Figure 37 that the data does not fit the parabolic assumption very well in many cases. To better characterize the oxidation behavior, Equation 13 was solved simultaneously for three or more data points from a specimen. This allowed approximate values for  $n$ ,  $k$ , and  $C$  to be determined over the range of data used in the calculation. The resulting  $n$ -values are summarized in Table 13. In general, the  $n$ -exponents at the start of the oxidation tests increased from near 2 at 1100°C to 4 or more at 900°C. Furthermore, as the tests progressed, in most cases  $n$  increased. This unusual behavior may be represents an extended period (at least 100 hours) of what would normally be called transient oxidation, resulting from a combination of physical and chemical factors.

**Table 12 Al<sub>3</sub>Ti Parabolic Oxidation Parameters**

Temp. °C	Condition	Rate Constant $k_p$ ( $\text{mg}^2/\text{cm}^4\text{hr}$ )	Apparent Permeability $K$ ( $\text{cm}.\text{sec})^{-1}$	Required Solubility $S$ ( $\text{cm}^{-3}$ )
<b>Cyclic</b>				
900	As Cast	0.0052	$6.83 \times 10^{10}$	$2.4 \times 10^{25}$
1100	As Cast	0.3324	$4.37 \times 10^{12}$	$3.7 \times 10^{25}$
	HIPed	0.0460	$6.04 \times 10^{11}$	$5.1 \times 10^{24}$
<b>Isothermal</b>				
900	As Cast	0.0031	$4.07 \times 10^{10}$	$1.4 \times 10^{25}$
	HIPed	0.0014	$1.84 \times 10^{10}$	$6.4 \times 10^{24}$
1000	As Cast	0.0095	$1.24 \times 10^{11}$	$6.8 \times 10^{24}$
	HIPed	0.0086	$1.13 \times 10^{11}$	$6.2 \times 10^{24}$
1100	As Cast	0.826	$1.08 \times 10^{13}$	$9.2 \times 10^{25}$
	HIPed	0.246	$3.23 \times 10^{12}$	$2.8 \times 10^{25}$

(Based on estimated effective diffusivities of  $2.87 \times 10^{-15} \text{ cm}^2/\text{sec}$  at  $900^\circ\text{C}$ ,  $1.83 \times 10^{-14} \text{ cm}^2/\text{sec}$  at  $1000^\circ\text{C}$ , and  $1.18 \times 10^{-13} \text{ cm}^2/\text{sec}$  at  $1100^\circ\text{C}$ .)

The SEM micrograph in Figure 40 shows that the specimens contained considerable interconnected porosity, with a very rough and uneven surface. The latter would tend to hinder the formation of a continuous, protective oxide layer, while the former would allow molecular oxygen to get into the specimen, exposing to oxidation a total surface area which is probably much greater than the "ideal" surface area calculated from the dimensions of the specimen. In addition, the porosity exposes the 2.1% Al phase to rapid internal oxidation, particularly at the higher temperatures. The total weight gain is therefore the sum of the internal weight gain and external scale formation.

Until a truly protective outer scale can form, the oxidation behavior of the specimens is dominated by the kinetics of internal oxidation. These kinetics can not be characterized based on these experiments, but it is likely that they would include an exponential term to describe the influx of oxygen through the growing oxide products, and a logarithmic term to account for the continuous consumption of the  $\alpha$ -Al phase. As the internal oxidation proceeds, the outer scale continues to grow, and becomes progressively more protective. The combined effects of these processes may account for the unusually high apparent n-exponents. Presumably, once a continuous protective  $\text{Al}_2\text{O}_3$  scale formed, or at least after the second phase was completely consumed, further oxidation would assume the expected parabolic behavior. In fully dense specimens, the initial "transient" oxidation normally only lasts a few hours, but due to the above factors, the transient period in the specimens examined here was extended to times close to or beyond the duration of the tests.

**Table 13  $\text{Al}_3\text{Ti}$ : Calculated n-Exponents**

Type of Test	Temp. °C	Condition	Initial	Average	Final
Cyclic					
	900	As-Cast	3.6	-----	
		HIPed	--	5.44	6.26
	1100	As-Cast	---	2.09	---
		HIPed	---	2.76	---
Isothermal					
	900	As-Cast	11.62	8.81	4.73
		HIPed	6.84	6.30	5.68
	1000	As-Cast	2.70	---	4.76
		HIPed	4.97	---	4.31
	1100	As-Cast	1.72	2.49	3.65
		HIPed	1.72	---	3.09

**Al<sub>5</sub>CuTi<sub>2</sub>.**

The addition of copper to Al<sub>3</sub>Ti was expected to improve the deformation and fracture behavior by converting the DO<sub>22</sub> structure of Al<sub>3</sub>Ti to an L1<sub>2</sub> structure. The effects of copper additions on oxidation properties were also investigated. The addition of a third component to binary Al<sub>3</sub>Ti greatly complicates oxidation behavior, in that the selective oxidation of any element results in the creation of some number of new phases. Copper, as the most noble of the three elements, was not expected to oxidize; rather, its main effect initially was to reduce the aluminum content, and thus the alloy's tendency to form a protective alumina scale. The aluminum content (62.5 atom %) is still above the 59% threshold found by Meier et al [36] for AlTi at 1100°C, so it was expected that alumina scales would still form. This was found to be the case; however, above 1000°C, the copper was found to cause severe chemical instability in the material.

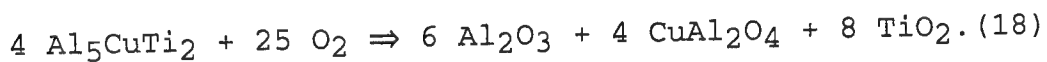
**Cyclic Oxidation:** As with Al<sub>3</sub>Ti, graphs of cyclic weight gain per unit area versus (time)<sup>1/2</sup> are not linear (Figure 41). At 900°C, this effect can again be described as either a decreasing rate constant with time or an n-exponent greater than 2. Assuming parabolic behavior and using data at longer times, the cyclic data at 900°C indicates a parabolic rate constant of about 0.025 in the As-Cast condition, and about 0.001 in the HIPed condition. At 1100°C, weight gain accelerated rapidly as the specimen became unstable, and so rate constants at extended times could not be calculated; however, the data suggests an initial  $k_p$  of about 3.50 in the As-Cast condition. These  $k_p$  values are shown in Table 14.

**Isothermal Oxidation:** Figure 42 shows that the isothermal behavior was very nearly parabolic. The rate constants calculated for 900° and 1000°C are approximately one order of magnitude higher than those for Al<sub>3</sub>Ti under similar conditions. This may be attributed to the lower aluminum content of the copper-modified material, which makes the formation of an alumina scale less likely. At 1100°C, however, the rate constant drops to the same level as at 900°C, and to a much lower level than Al<sub>3</sub>Ti at the same temperature.

Table 14**Al<sub>5</sub>CuTi<sub>2</sub> Parabolic Rate Constants**

	Temp. °C	Condition	Rate Constant $k_p$ (mg <sup>2</sup> /cm <sup>4</sup> hr)
<b>Cyclic</b>	900	As Cast	.025
		HIPed	0.001
	1100	As Cast	3.5 (initial)
		HIPed	-----
<b>Isothermal</b>	900	As Cast	0.028
		HIPed	0.010
	1000	As Cast	0.922
		HIPed	0.236
	1100	As Cast	0.028

**High Temperature Instability:** The oxidative and physical instability at 1100°C can be explained in terms of the kinetic path of oxidation. From the Al-Cu and Ti-Cu binary phase diagrams [3] it can be seen that all of the Al-Cu and Ti-Cu compounds have melting temperatures below 1100°C with the exception of  $\beta$ -Ti. Complete oxidation of the compound at 1100°C, based on phase stability diagrams [44] and on the phases identified by x-ray spectroscopy, proceeds according to the equation:



The  $\text{CuAl}_2\text{O}_4$  phase was expected to decompose into  $\text{CuO}$  and  $\text{Al}_2\text{O}_3$  below 800°C. However, EDS and X-ray spectroscopy indicated that no  $\text{CuO}$  and only a small amount of  $\text{CuAl}_2\text{O}_4$  were present in the oxide. In addition, elemental copper peaks were identified in the crucible, which had turned a deep brown color. Thus, it appears that as oxidation occurs,  $\text{Al}_2\text{O}_3$  and  $\text{TiO}_2$  form preferentially, while the alloy becomes progressively more copper-rich. As the copper content of the alloy increases, new, lower-melting-point phases would form. Eventually a phase which is liquid at 1100°C is formed, at which point rapid oxidation of the aluminum and titanium in the liquid occurs, thus accounting for the sudden rapid weight gain. The remaining molten



copper would oxidize more slowly, and could flow out into the crucible before oxidizing.

### CONCLUSIONS

1. Saphikon is the most compatible fiber with the  $\text{Al}_3(\text{Ti}, \text{Nb})$  matrices.
2.  $\text{TiB}_2$  appears to be chemically compatible with the  $\text{Al}_3(\text{Ti}, \text{Nb})$  matrices.
3. SCS-6 fiber is incompatible with the  $\text{Al}_3(\text{Ti}, \text{Nb})$  matrices.
4. The lack of matrix ductility results in significant matrix cracking during HIP consolidation due to fiber-matrix CTE mismatch.
5. The microstructure of  $\text{Al}_3\text{Ti} + \text{Nb}$  powder is coarser than that of  $\text{Al}_3\text{Ti}$ . The as-solidified microstructure of  $\text{Al}_3\text{Ti} + \text{Nb}$  powder is retained during HIP processing, i.e., prior partical boundaries are visible in the HIPed materials.
6.  $\text{AlTi}$  oxidizes at a rate two orders of magnitude faster than  $\text{Al}_3\text{Ti}$ .
7. Partitioning of aluminum during solidification of  $\text{Al}_3\text{Ti}$  results in internal oxidation of  $\text{Al}_3\text{Ti}$ . The internal oxidation of free aluminum accounts for 90% of the total weight gain.
8. Oxidation of  $\text{Al}_5\text{CuTi}_2$  proceeds with the preferential consumption of Al and Ti. As a result, low melting point copper rich phases form leading to rapid oxidation.
9. The oxidation behavior of  $\text{AlTi}$  is linear. The oxidation behavior of  $\text{Al}_3\text{Ti}$  and  $\text{Al}_5\text{CuTi}_2$  was fit to parabolic kinetic equations; however, the n exponents were generally greater than 2.
10. The oxidation kinetics of  $\text{Al}_3\text{Ti}$  is controlled by the short circuit diffusion of molecular oxygen through cracks and imperfections in the oxide scale.

**ACKNOWLEDGMENTS**

The authors are very grateful to Mrs. Mary E. Donnellan for her technical contributions to this work. Technical discourse with Mr. John B. Boodey was also very valuable. The financial support of ONR Code 11 is gratefully acknowledged as is the guidance of the program's Technical Monitor, Dr. Steven Fishman.

**REFERENCES**

1. E.L. Hall and Shyh-Chin Huang, "Microstructures of Rapidly-Solidified Binary TiAl Alloys, Acta Metallurgica et Materialia, 38(4)(1990), 539-549.
2. J.D. Destefani, "Advances in Intermetallics," Advanced Materials & Processes, 2(1989), 37-41.
3. Binary Alloy Phase Diagrams, vol I, T.B. Massalski et al. editors, (ASM, Materials Park, OH, 1986), 175
4. K.S. Kumar, "Review: Ternary Intermetallics in Aluminum-Refractory Metal-X(X= V, Cr, Mn, Fe, Co, Ni, Cu, Zn) Systems," (Report MML JL 89-46, Martin Marietta Laboratories, Baltimore, MD, April 1989).
5. M. Yamaguchi, Y. Shirai, and Y. Umakaoshi, "Deformation Behavior of Single and Polycrystal Al<sub>3</sub>Ti and Al<sub>3</sub>Ti with Ternary Alloying Additions," Dispersion Strengthened Aluminum Alloys, ed. Y-W. Kim and W.M. Griffith (Warrendale, PA: The Metallurgical Society, 1988), 721-740
6. D.G. Pettifor, "The Structures of Binary Compounds: I. Phenomenological Structure Maps," Journal of Physics C, 19(1986), 285-313.
7. S. Zhang, J.P. Nic, and D.E. Mikkola, "New Cubic Phases Formed by Alloying Al<sub>3</sub>Ti with Mn and Cr," Scripta Metallurgica, 24(1990), 57-62.
8. J. Tarnacki and Y-W Kim, "A Study of Rapidly Solidified Al<sub>3</sub>Ti Intermetallics with Alloying Additions," Scripta Metallurgica, 22(1988), 329-334.
9. M.B. Winnicka and R.A. Varin, "Compression Ductility and Fracture of Boron-Free and Highly Boron-Doped Al<sub>5</sub>CuTi<sub>2</sub> Intermetallic Compound," Scripta Metallurgica et Materialia, 24(1990), 611-615.

10. E.P. George, W.D. Porter, and D.C. Joy, "Identification of Cleavage Planes in an  $\text{Al}_3\text{Ti}$ -Base Alloy by Electron Channeling in the SEM," (Materials Research Society, Pittsburgh, PA, 1989), vol. 133, 311-315.
11. E.P. George, W.D. Porter, H.M. Henson, W.C. Oliver, and B.F. Oliver, "Cleavage Fracture in an  $\text{Al}_3\text{Ti}$ -based Alloy Having the  $\text{L}_{12}$  Structure," Journal of Materials Research, 4(1)(1989), 78-84.
12. E.P. George, J.A. Horton, W.D. Porter, and J.H. Schneibel, "Brittle Cleavage of  $\text{L}_{12}$  Trialuminides," Journal of Materials Research, 5(8)(1990), 1639-1648.
13. C.L. Fu, "Electronic, Elastic, and Fracture Properties of Trialuminide Alloys:  $\text{Al}_3\text{Sc}$  and  $\text{Al}_3\text{Ti}$ ," Journal of Materials Research, 5(5)(1990), 971-980.
14. D.B. Marshall B.N. Cox, and A.G. Evans, "The Mechanics of Matrix Cracking in Brittle Matrix Fiber Composites," Acta Metallurgica 33(11)(1985), 2013-2021.
15. D.J. Hannant, D.C. Hughes, and A. Kelly, "Toughening of cement and other brittle solids with fibres," Philosophical Transactions of the Royal Society of London. 310(1983), 175-190.
16. J.Aveston, G.A. Cooper, and A. Kelly, "Paper2 Single and multiple fracture,"
17. J.R. Rice, Fracture. Ed., H.Liebowitz, 2(1968), 191
18. Ajay K. Misra, "Identification of Thermodynamically Stable Ceramic Reinforcement Materials for Iron Aluminide Matrices," Metallurgical Transactions A. 21A(1990), 441-446.
19. D.Jewitt and M. Harrison, "Single Crystal Alumina Fiber Development," Proceedings DoD Eighth Metal Matrix Composite MMC Technology Conference, Vol 1. (Monterey, CA: NPGS, June 1989).
20. Ajay K. Misra, "Thermodynamic Analysis of Chemical Compatibility of Ceramic Reinforcement Material with Niobium Aluminides," Journal of Materials Research. (5)(7)(1990), 1561-1566.
21. M.H. Loretto and D.G. Konitzer, "The Effect of Matrix Reinforcement Reaction on Fracture in  $\text{Ti-6Al-4V}$ -Based Composites," Metallurgical Transactions A. 21A(June 1990), 1579-1587.

22. S.F. Baumann, P.K. Brindley, and S.D. Smith, "Reaction Zone Microstructure in a  $Ti_3Al$  + Nb/SiC Composite," Metallurgical Transactions A. 21A(June 1990), 1559-1569.
23. William E. Frazier and Mary E. Donnellan, "HIP Consolidation of Aluminum-Rich Intermetallic Alloys and Their Composites," (NAWCADWAR-92003-60, Naval Air Warfare Center, Aircraft Division, Warminster, Jan 1992).
24. O. Kuaschewski and B.E. Hopkins, Oxidation of Metals and Alloys. (London, UK: Butterworths, 1953)
25. Per Kofstad, High-Temperature Oxidation of Metals. (NY, NY: John Wiley, 1966)
26. Y-W.Kim, W.M. Griffith, and F.H. Froes, "Surface Oxides in P/M Aluminum Alloys," Journal of Metals. 32(8)(August 1985), 27-33.
27. D.W. Mckee and S.C. Huang, "The Oxidation Behavior of Gamma-Titanium Aluminide Alloys Under Thermal Cycling Conditions," Corrosion Science 33(12)(1992)1899-1914.
28. Y. Umakoshi et al., "Oxidation Resistance of Intermetallic Compounds  $Al_3Ti$  and  $TiAl$ ," Journal of Material Science. 24(1989)1599-1603.
29. J. Subrahmanyam, "Cyclic Oxidation of Aluminized Ti-14Al-24Nb Alloy". Journal of Materials Science, Vol. 23, pp.1906-1910 (1988).
30. J. Subrahmanyam and J. Annapurna, "High Temperature Cyclic Oxidation of Aluminide Layers on Titanium". Oxidation of Metals, Vol.26, No.3/4, pp.275-285 (1986).
31. J.L. Smialek and D.L. Humphrey, "Oxidation Kinetics of Cast  $TiAl_3$ ," Scripta Metallurgica et Materialia. 26(1992)1763-1768.
32. E.U. Lee and J. Waldman, Scripta Metallurgica et Materialia. 22(1988), 1389.
33. R.A. Perkins, K.T. Chiang, and G.H. Meier, "Formation of Alumina on Ti-Al Alloys". Scripta MET, Vol.21, pp.1505-1510 (1987).
34. K. Hirukawa, H. Mabuchi, and Y. Nakayama, "Oxidation Behavior of  $TiAl_3$ -Based Alloys with the  $L1_2$  Structure". Scripta MET, Vol.25, pp.1211-1216 (1991).

35. G.H. Meier, "Fundamentals of the Oxidation of High-Temperature Intermetallics". In Oxidation of High-Temperature Intermetallics, Ed. T. Grobstein and J. Doychak, TMS, 1988, pp.1-16.
36. G.H. Meier, D. Appalonia, R.A. Perkins, and K.T. Chiang, "Oxidation of Ti-Base Alloys". In Oxidation of High-Temperature Intermetallics, Ed. T. Grobstein and J. Doychak, TMS, 1988, pp.185- 193.
37. R.A. Perkins and K.T. Chiang, "Formation of Alumina on Niobium and Titanium Alloys". In Oxidation of High-Temperature Intermetallics, Ed. T. Grobstein and J. Doychak, TMS, 1988, pp.157- 169.
38. M.G. Hebsur, et al, "Influence of Alloying Elements on the Oxidation Behavior of NbAl<sub>3</sub>". In Oxidation of High-Temperature Intermetallics, Ed. T. Grobstein and J. Doychak, TMS, 1988, pp.171- 183.
39. Richard A. Swalin, Thermodynamics of Solids. (NY, NY: John Wiley & Sons, 1972).
40. D.H. StJohn and L.M. Hogan, "Thermal Stability in the Al-Al<sub>3</sub>Ti System," Journal of Materials Science 15(1980)2369-2375.
41. W.D. Kingery, H.K. Bowen, and D.R. Uhlman, Introduction to Ceramics, Second Edition. J. Wiley & Sons, 1976.
42. S.N. Sankaran, R.A. Outlaw, and R.K. Clark, "Surface Effects on Hydrogen Permeation through Ti-14Al-21Nb Alloy". In Summary Proceedings of the 4th Workshop on Hydrogen-Material Interactions, Ed. H.G. Nelson. NASP Workshop Publication 1013, Feb. 1993, pp.245- 266.
43. W.E. Frazier, J.E. Benci, and J.W. Zanter, "Microstructural Evaluation of As-Cast and Melt-Spun Al<sub>3</sub>Ti and Al<sub>3</sub>Ti Plus Copper". In Low Density, High Temperature Powder Metallurgy Alloys, Ed. W.E. Frazier and M.J. Koczak, TMS, 1991, pp.49-69.
44. R.S. Roth, T. Negas, and L.P. Cook, Phase Diagrams for Ceramists, Vol. IV (Figures 5000-5590). The American Ceramic Society, Inc., Columbus, OH, 1981.

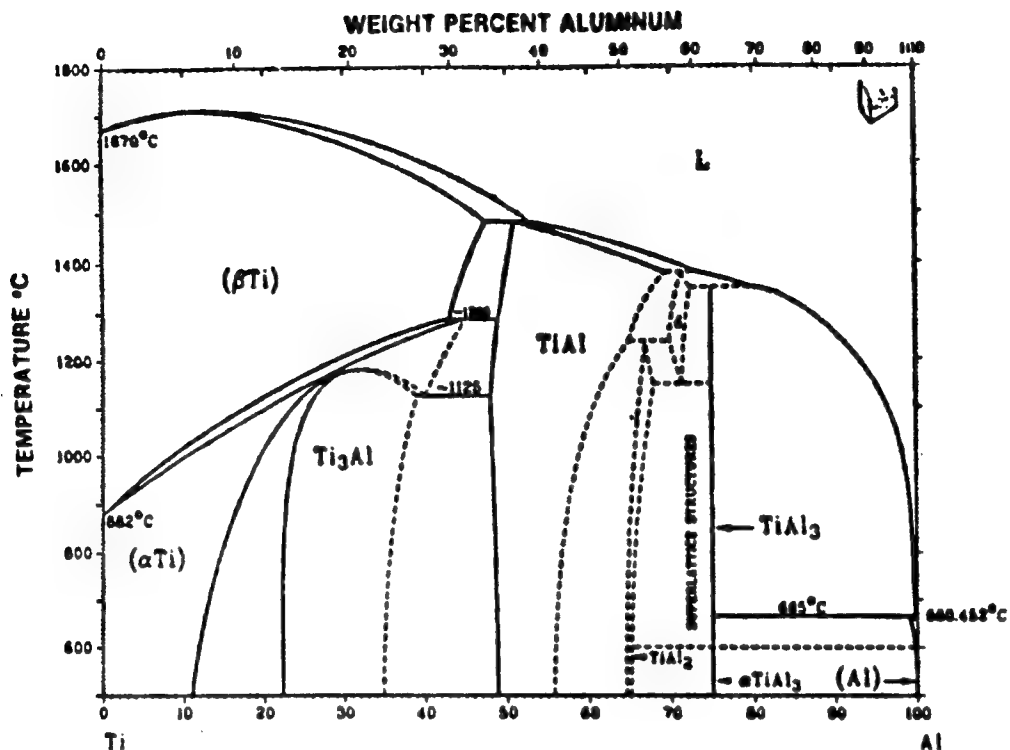


Figure 1 The Aluminum-Titanium Equilibrium Phase Diagram.

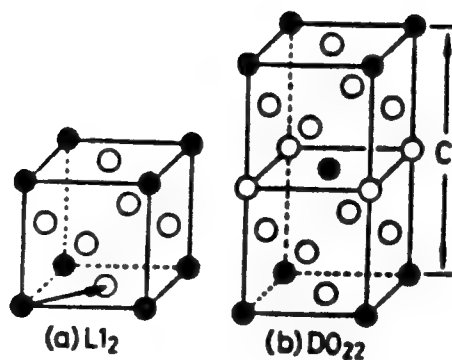


Figure 2 Crystal structure from L<sub>12</sub> to DO<sub>22</sub>.

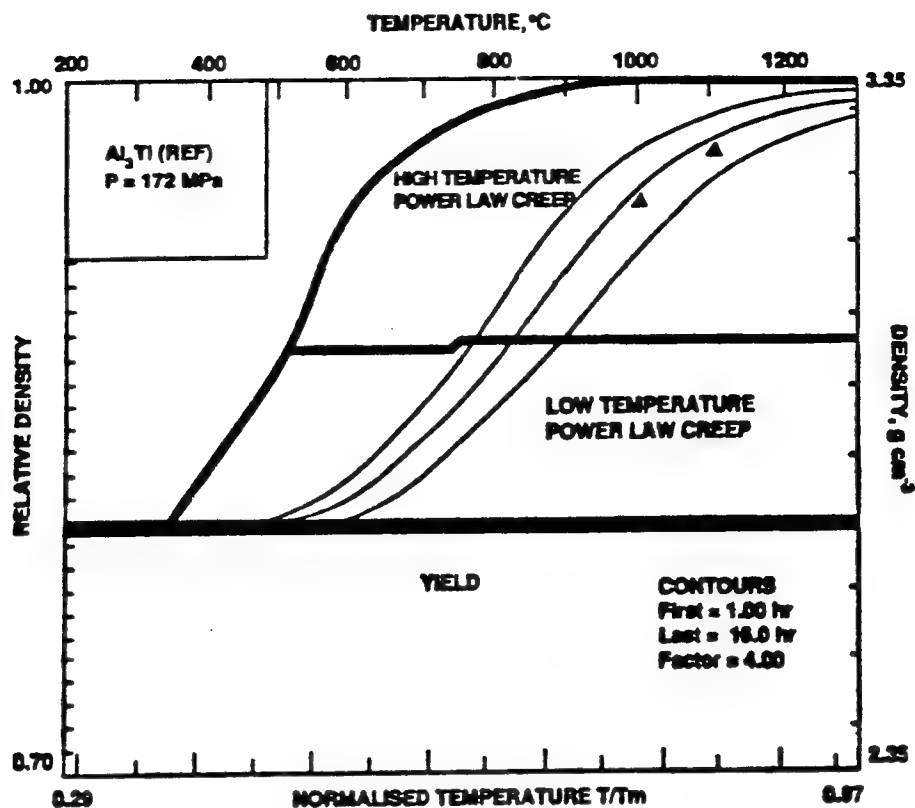


Figure 3 HIP Map for the Consolidation of  $\text{Al}_3\text{Ti}$ .

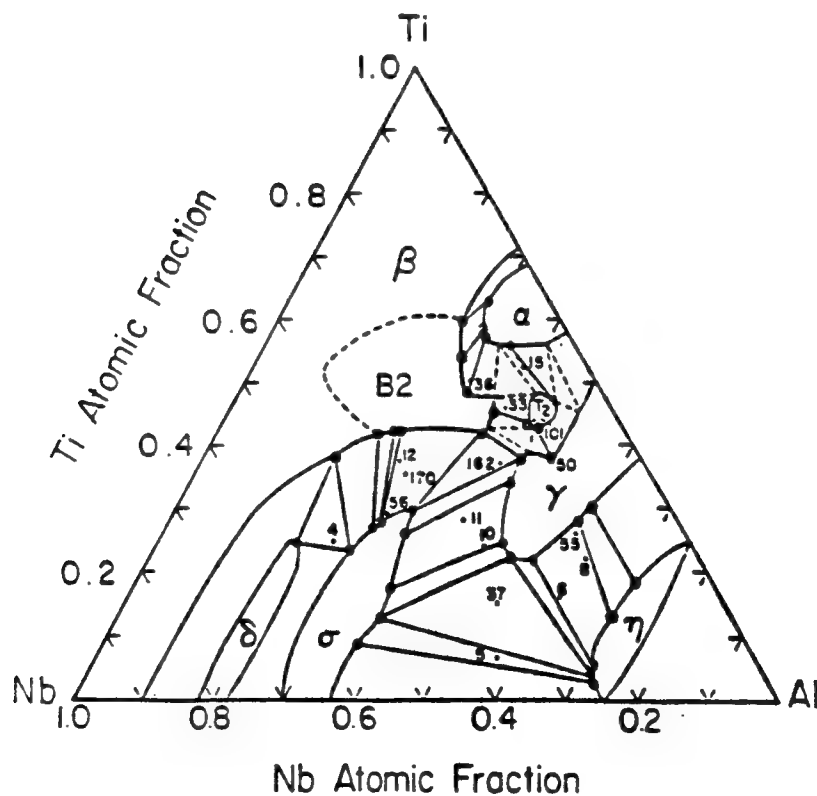


Figure 4 Isothermal Section of the Al-Ti-Nb Equilibrium Phase Diagram at  $1200^{\circ}\text{C}$ .

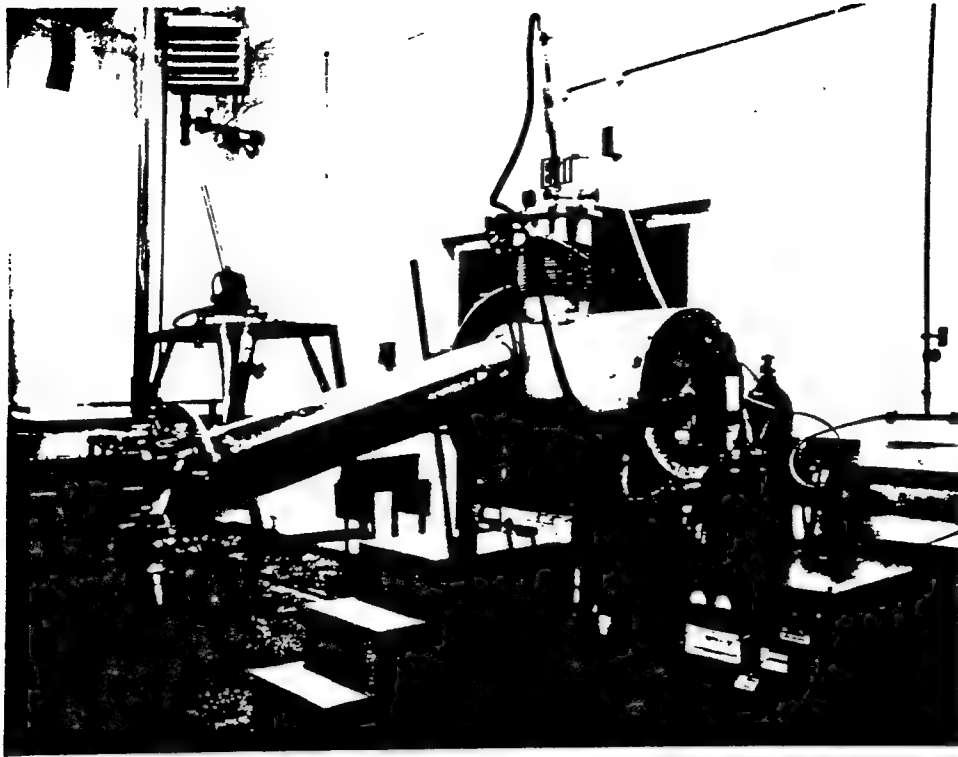
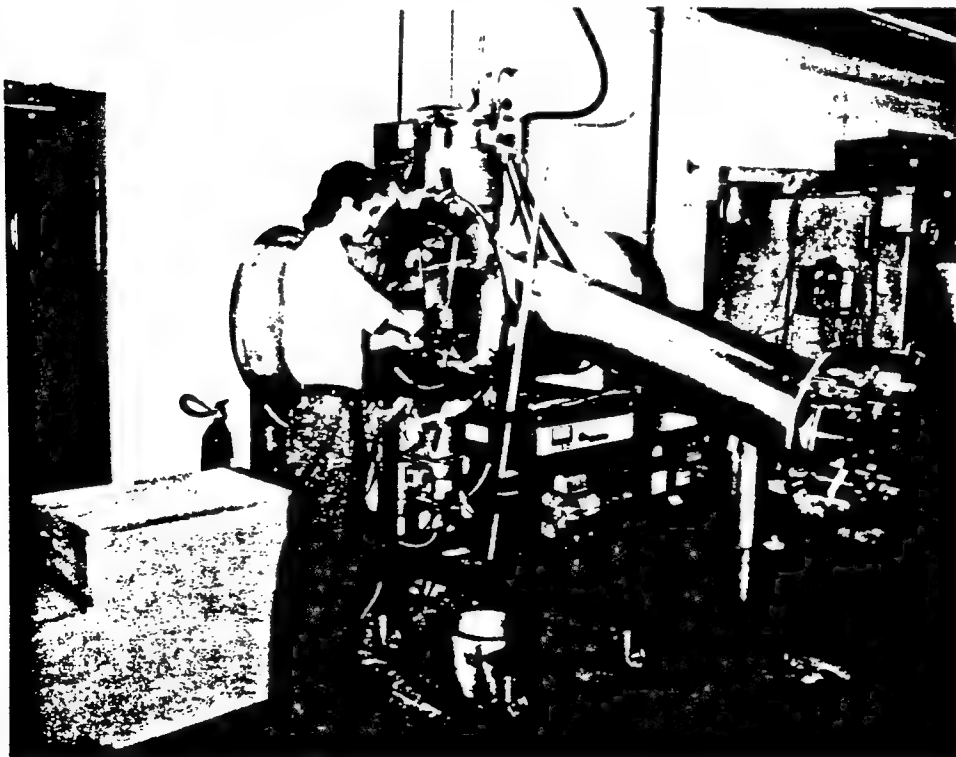
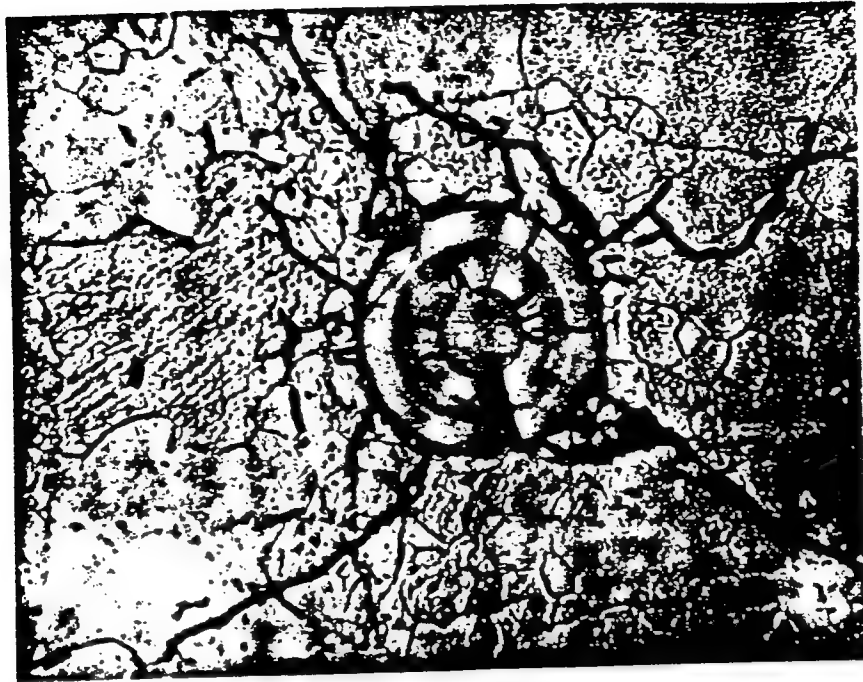


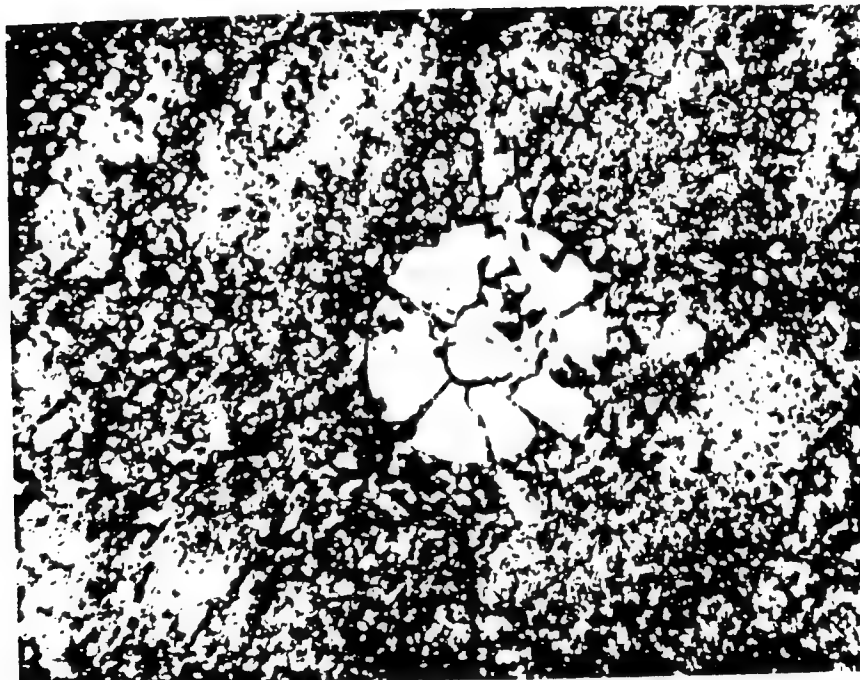
Figure 5 Marko Materials Melt Spinner.





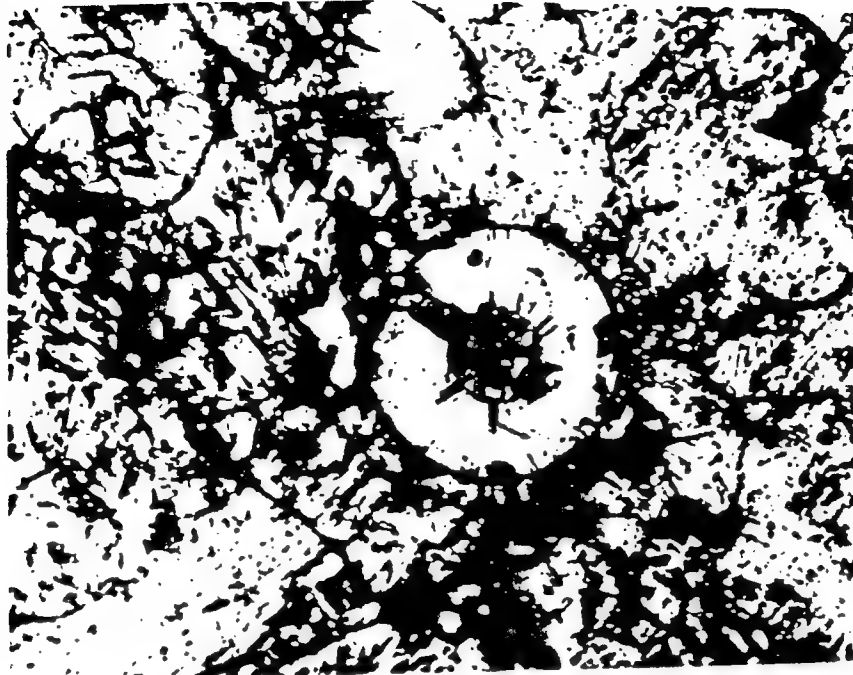


(a)



(b)

Figure 6 Optical Micrographs at 400X of  $\text{TiB}_2$  Fiber Composites Consolidated at 1100 °C: (a)  $\text{Al}_3\text{Ti}$  Matrix and (b)  $\text{Al}_3\text{Ti}+\text{Nb}$  Matrix.



(a)



(b)

Figure 7 Optical Micrographs at 400X of TiB<sub>2</sub> Fiber Composites Consolidated at 1200 °C: (a) Al<sub>3</sub>Ti Matrix, and (b) Al<sub>3</sub>Ti + Nb Matrix.



(a)



(b)

Figure 8 Optical Micrographs of SCS-6 Fiber Composites Consolidated in  $\text{Al}_3\text{Ti}$  + Nb Matrix: (a) at 1100 °C (200X), and (b) at 1200 °C (220X).

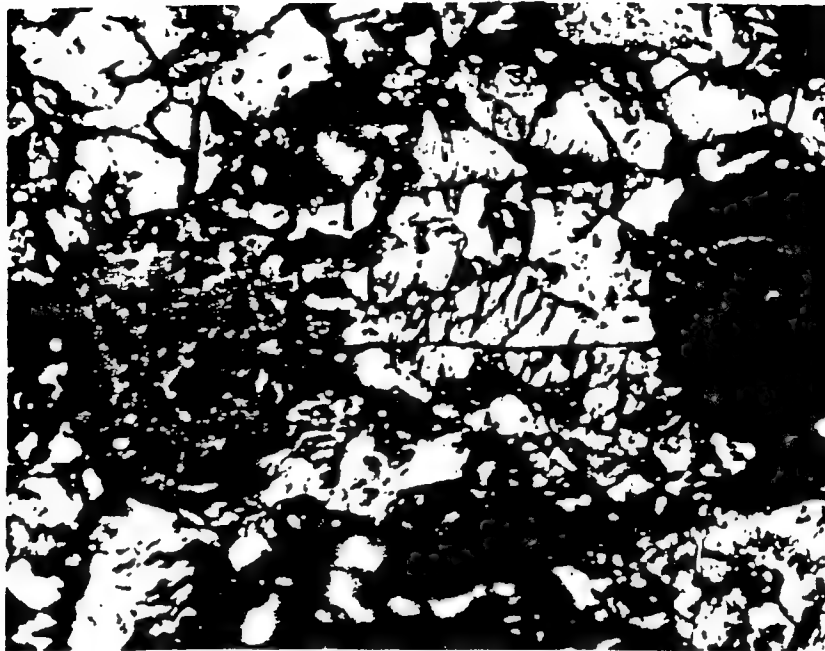


(a)

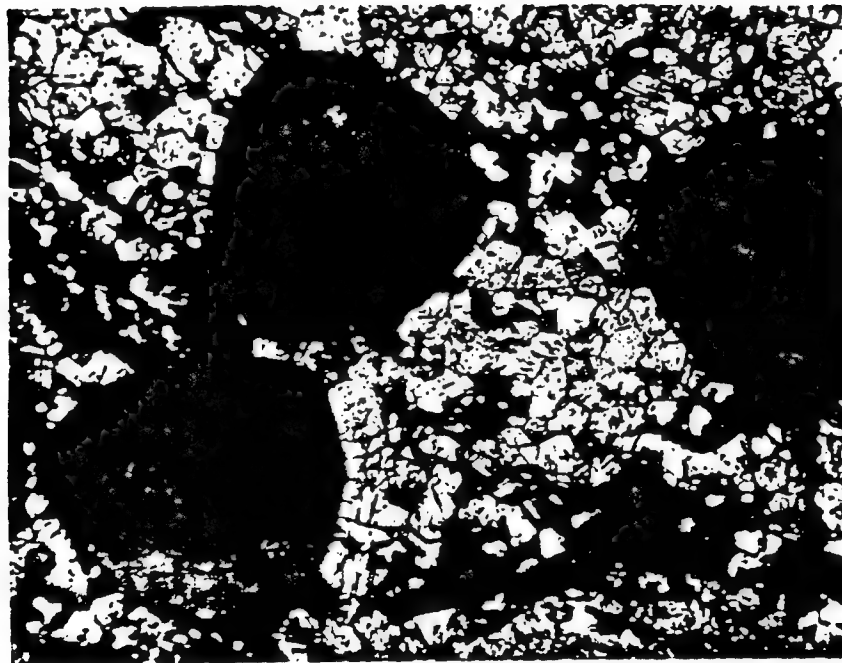


(b)

Figure 9 Optical Micrographs at 400X of Saphikon Fiber Composites Consolidated at 1100 °C: (a)  $\text{Al}_3\text{Ti}$  Matrix, and (b)  $\text{Al}_3\text{Ti} + \text{Nb}$  Matrix.

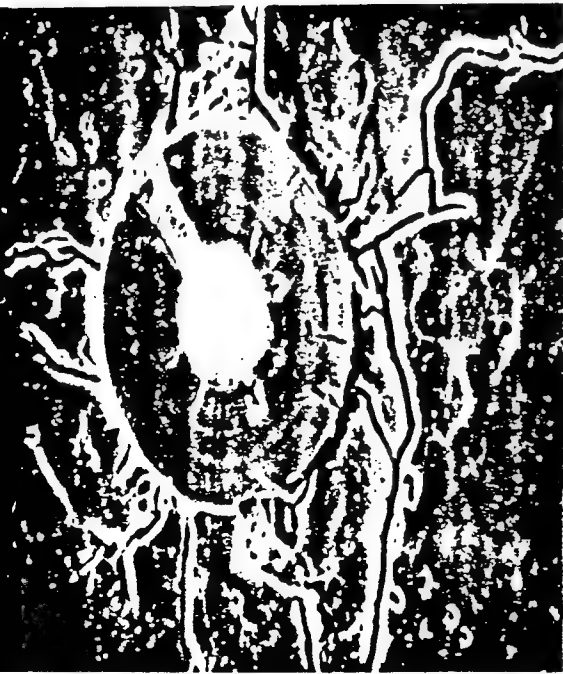


(a)



(b)

Figure 10 Optical Micrographs of Saphikon Fiber Composites Consolidated at  $1200^{\circ}\text{C}$ : (a)  $\text{Al}_3\text{Ti}$  Matrix (400X), and (b)  $\text{Al}_3\text{Ti} + \text{Nb}$  Matrix (440X).



(a)



(b)



(c)

Figure 11  $\text{Al}_3\text{Ti}/\text{TiB}_2$  Composites HIPed at 1100 °C: (a) SEM Micrograph, (b) EDS Map for Aluminum and (c) EDS Map for Molybdenum.



Figure 12 SEM Micrograph of  $\text{Al}_3\text{Ti}/\text{TiB}_2$  Composites HIPed at 1200 °C.



Figure 13 SEM Micrograph of  $\text{Al}_3(\text{Ti}, \text{Nb})/\text{TiB}_2$  Composites HIPed at 1100 °C

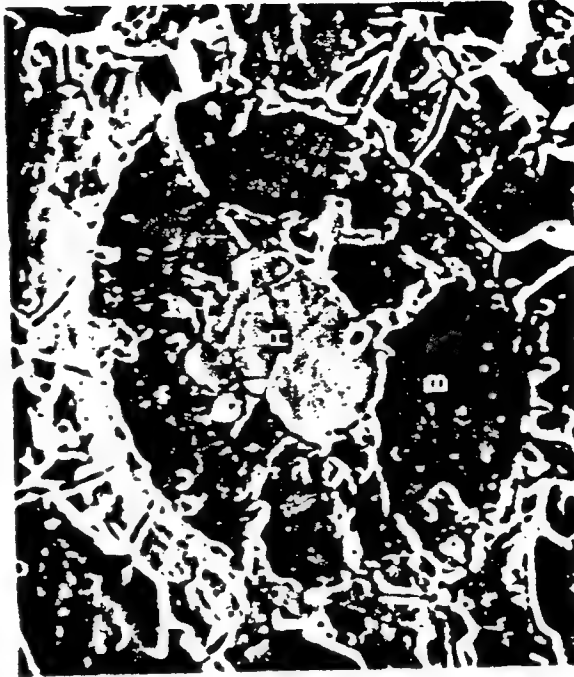


Figure 14 SEM Micrograph of  $\text{Al}_3(\text{Ti}, \text{Nb})/\text{TiB}_2$  Composites HIPed at 1200 °C

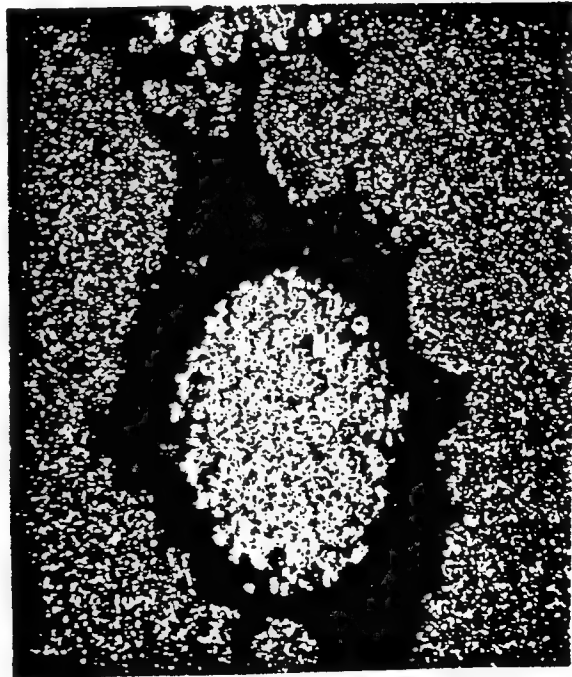




(a)



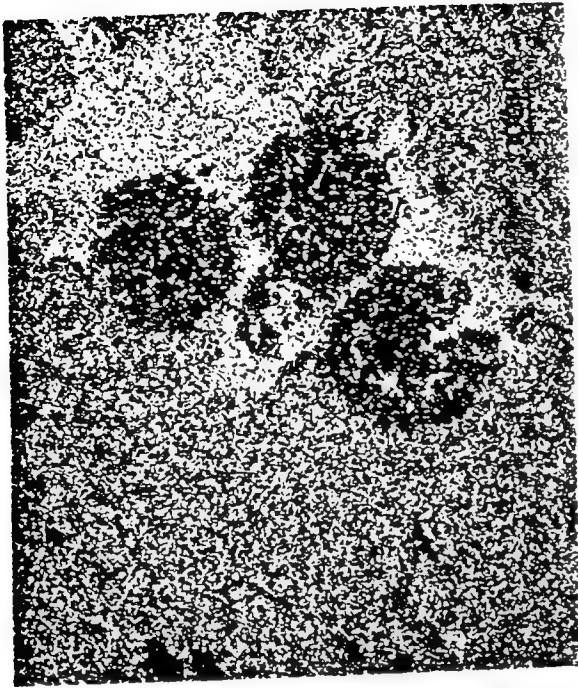
(b)



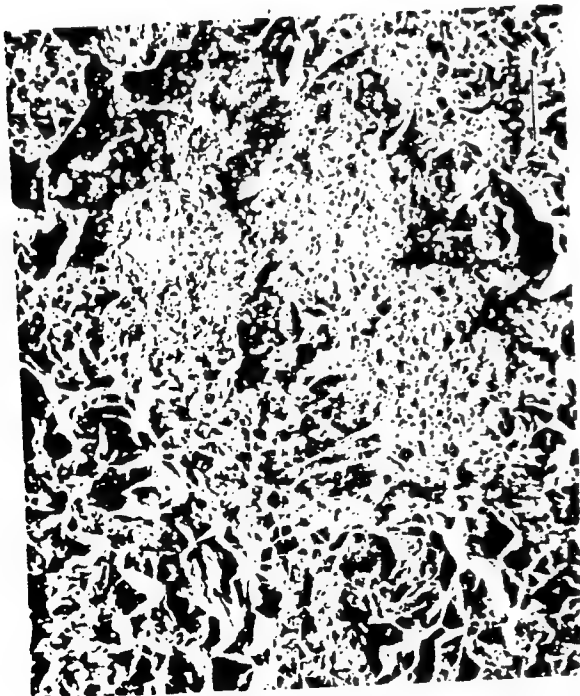
(c)

Figure 15 Al<sub>3</sub>Ti/SCS-6 Composites  
HIPed at 1100 °C: (a) SEM  
Micrograph, (b) EDS Map for  
Aluminum, and (c) EDS Map for  
Titanium.





(b)



(a)

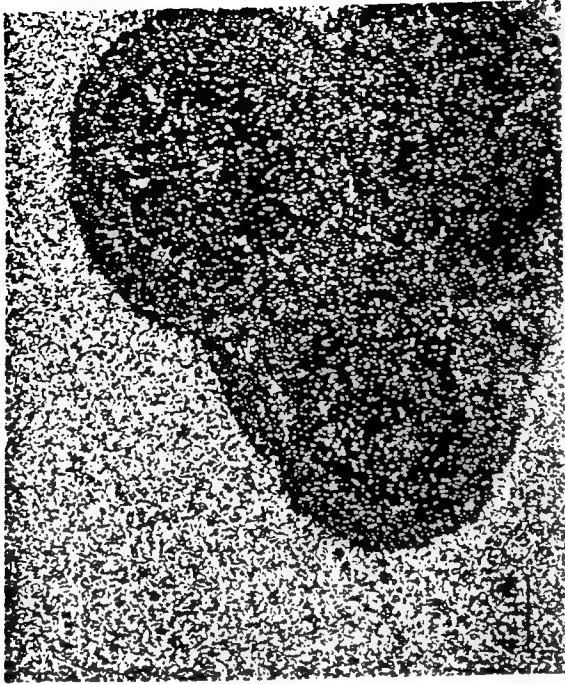


(c)

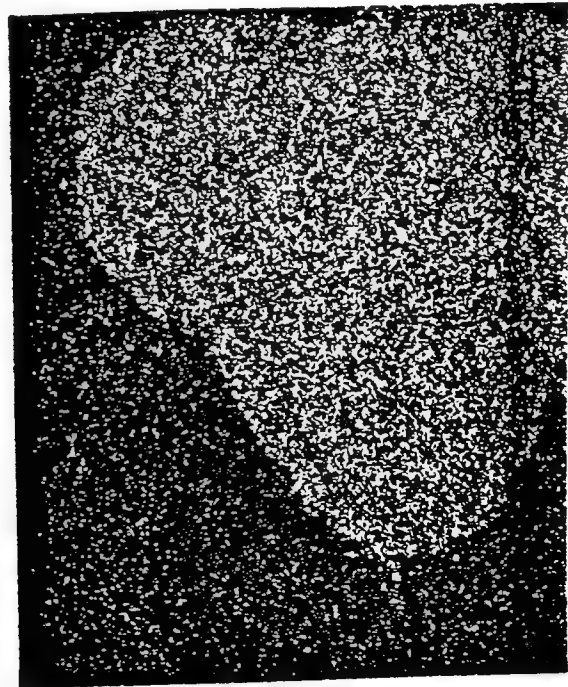
Figure 16 Al<sub>3</sub>Ti/SCS-6 Composites  
HIPed at 1200 °C: (a) SEM  
Micrograph, (b) EDS Map for  
Aluminum, and (c) EDS Map for  
Titanium



(a)

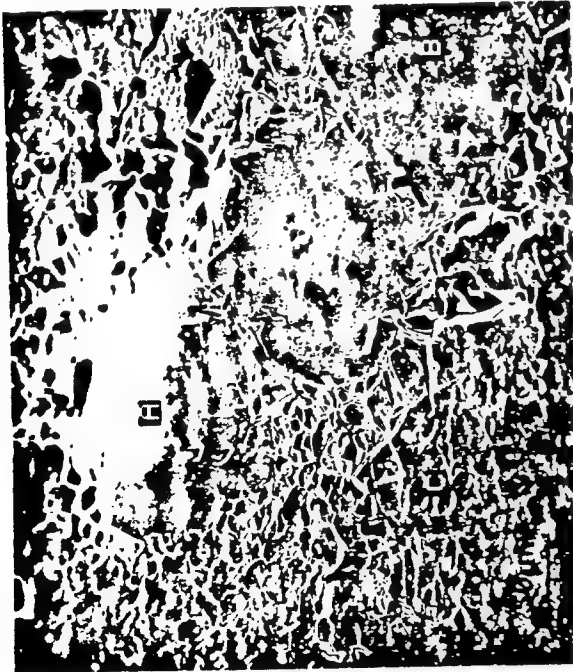


(b)

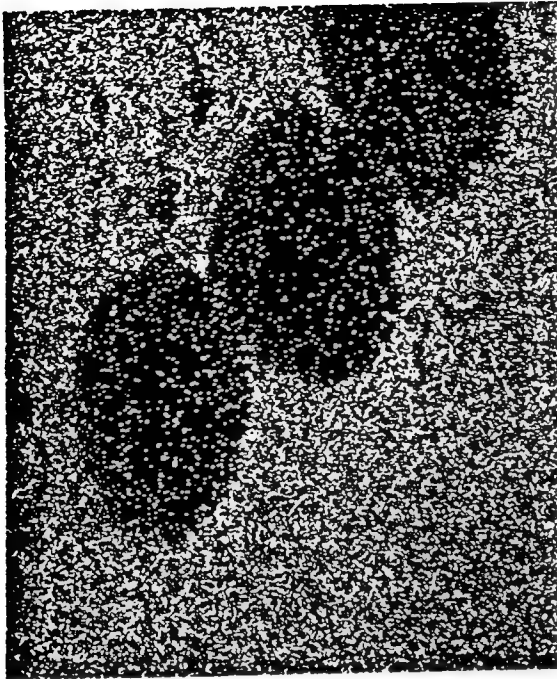


(c)

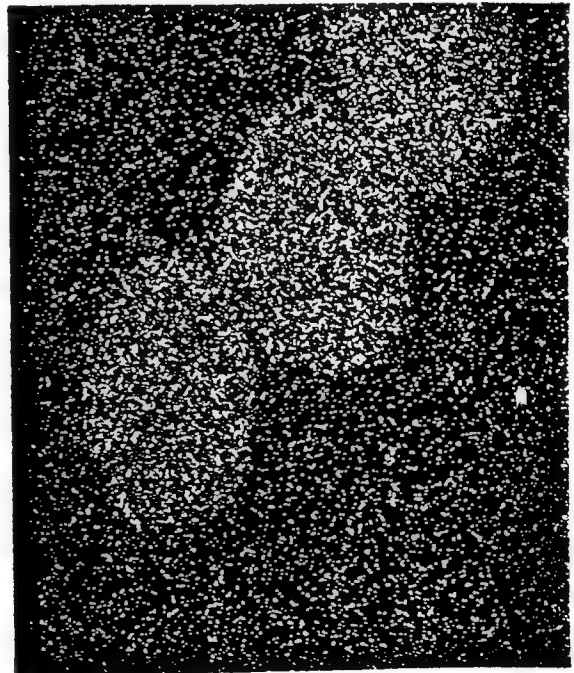
Figure 17  $\text{Al}_3(\text{Ti}, \text{Nb})/\text{SCS-6}$   
Composites HIPed at 1100 °C:  
(a) SEM Micrograph, (b) EDS Map for  
Aluminum, and (c) EDS Map for  
Titanium.



(a)

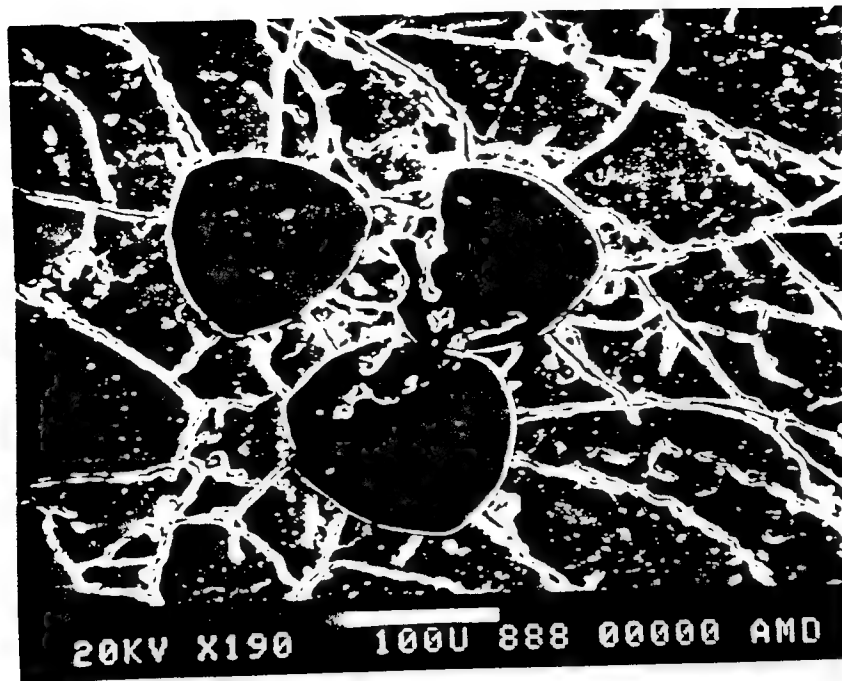


(b)



(c)

Figure 18  $Al_3(Ti, Nb)/SCS-6$   
Composites HIPed at 1200 °C:  
(a) SEM Micrograph, (b) EDS Map for  
Aluminum, and (c) EDS Map for  
Titanium.

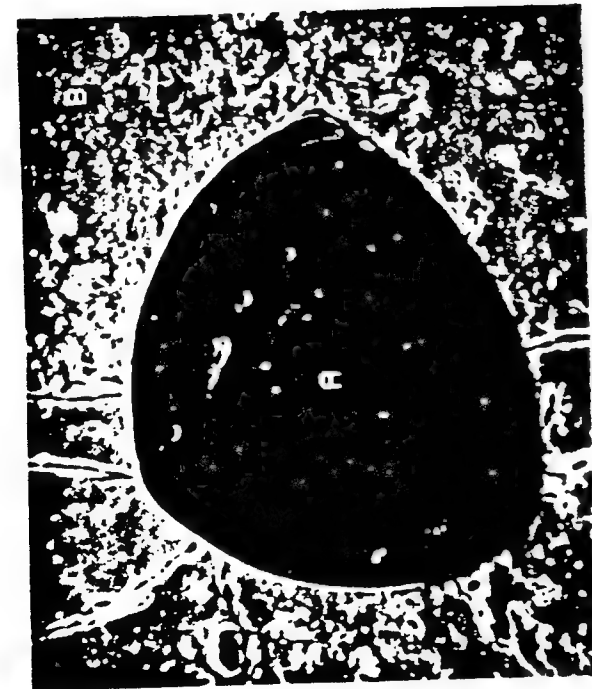


(a)

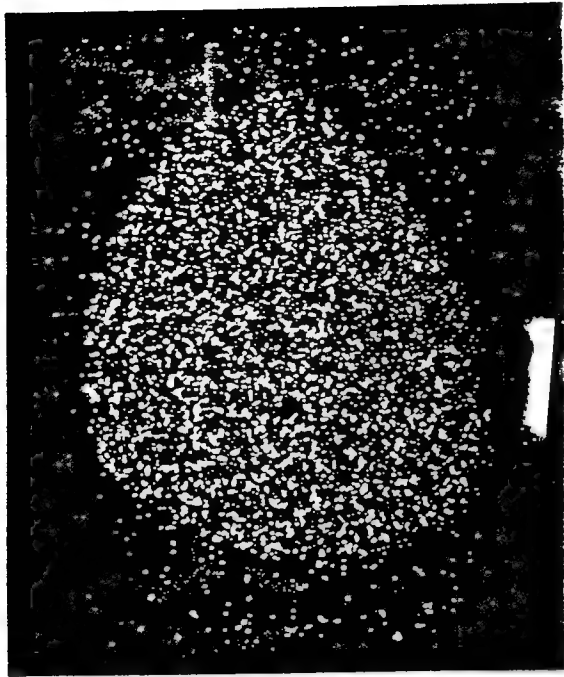


(b)

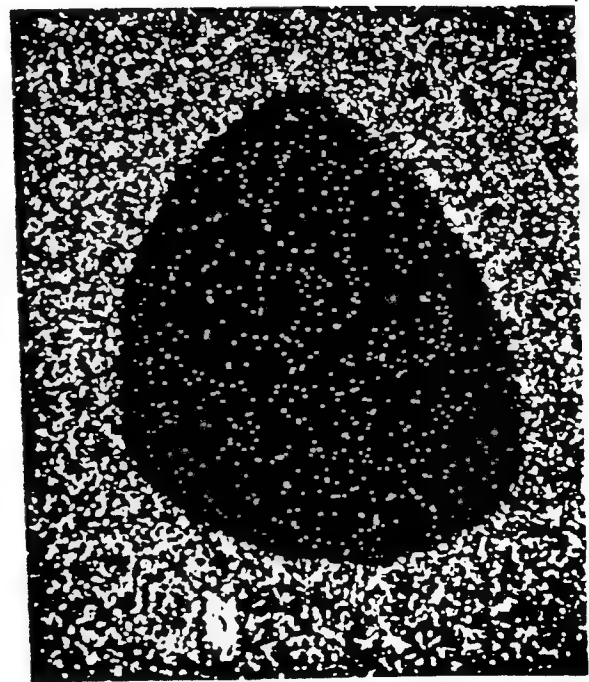
Figure 19 A SEM Micrograph of  $\text{Al}_3\text{Ti}$ /Saphikon Composites HIPed at (a) 1100 °C and (b) 1200 °C.



(a)

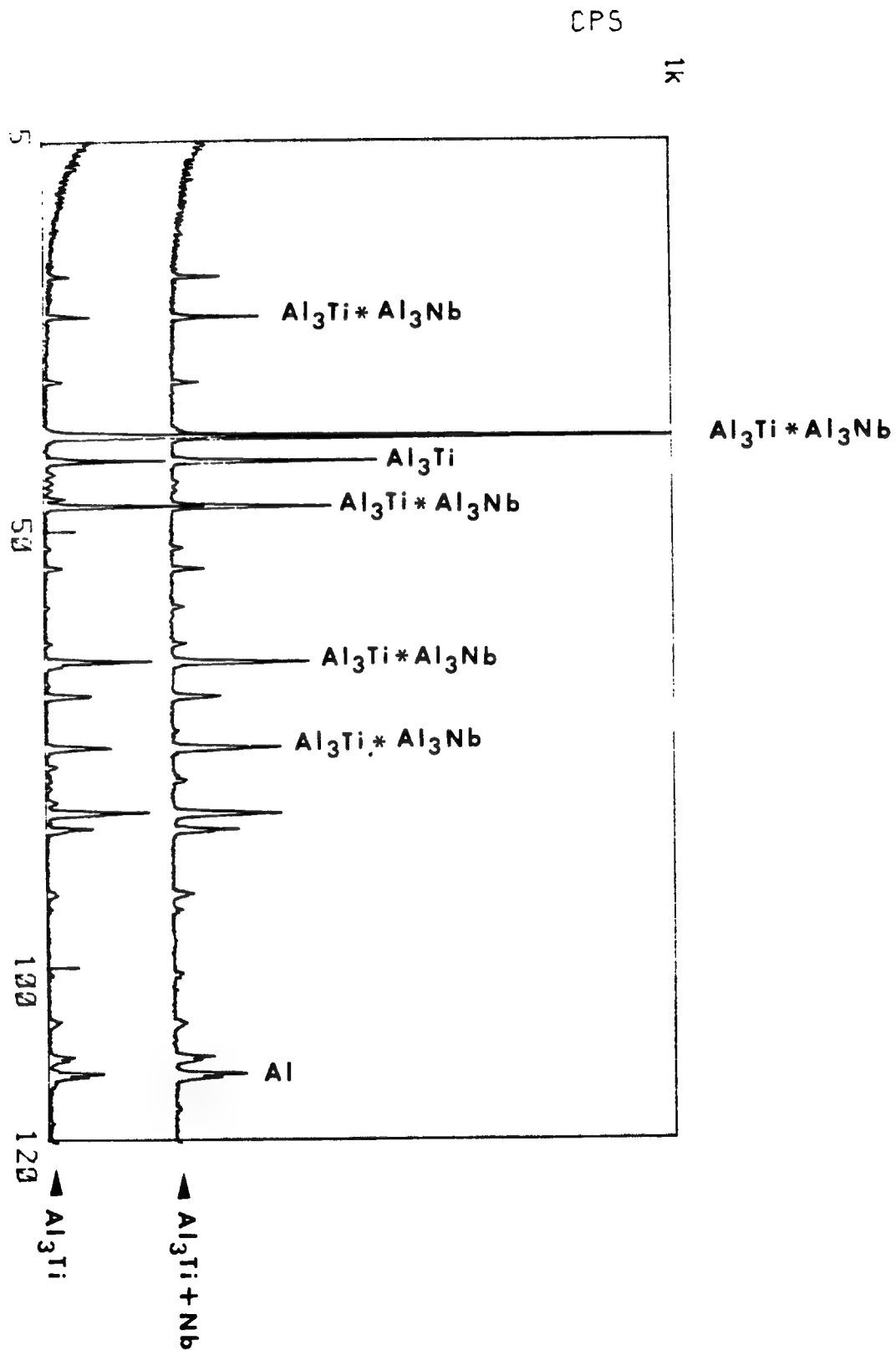


(b)



(c)

Figure 20  $\text{Al}_3(\text{Ti}, \text{Nb})/\text{Saphikon}$   
Composites HIPed at 1100 °C:  
(a) SEM Micrograph, (b) EDS Map for  
Oxygen, and (c) EDS Map for  
Titanium.

Figure 21 X-ray Diffraction Profiles for Melt Spun  $\text{Al}_3\text{Ti}$ , and Melt Spun  $\text{Al}_3\text{Ti} + \text{Nb}$ .

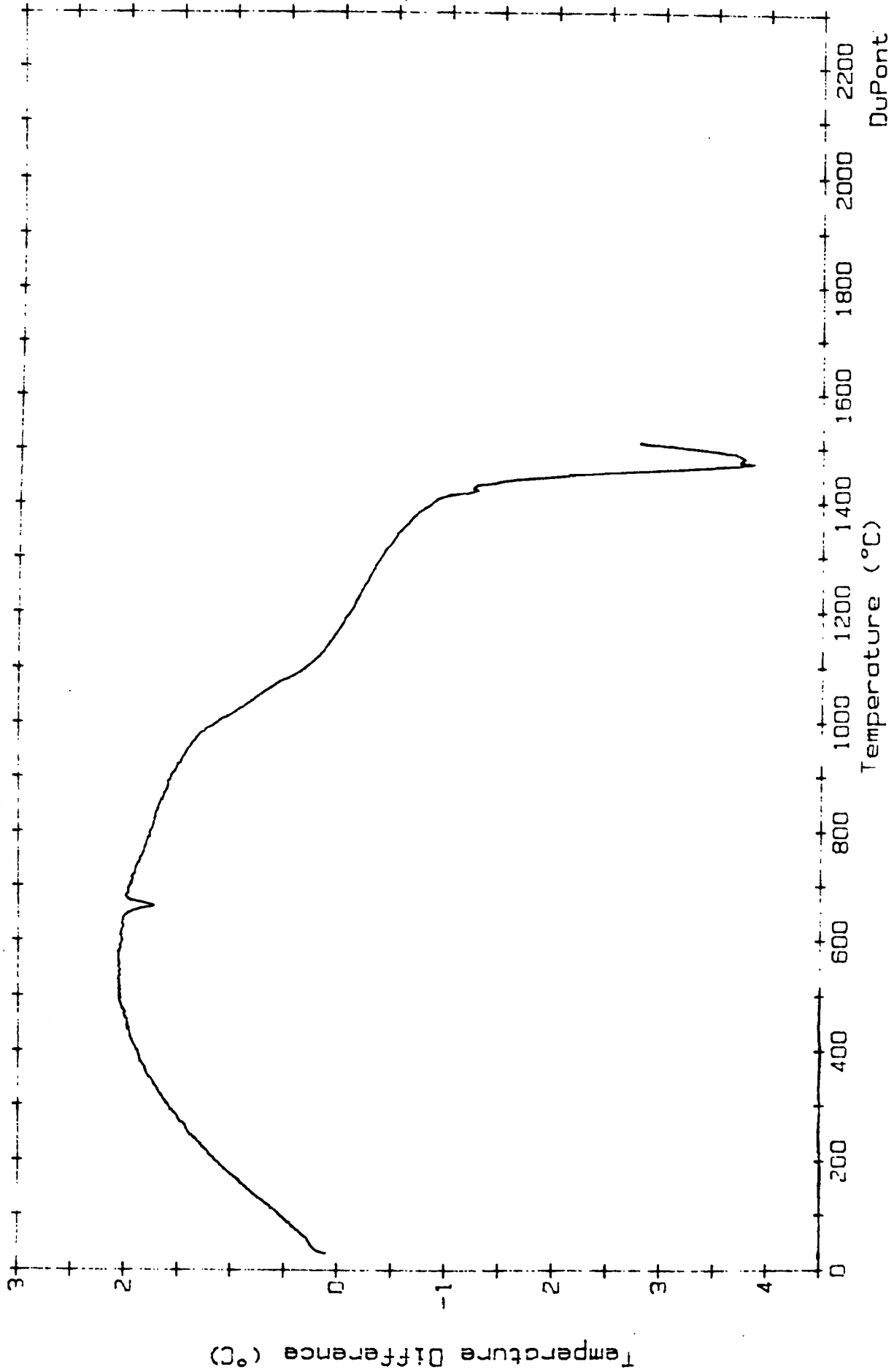
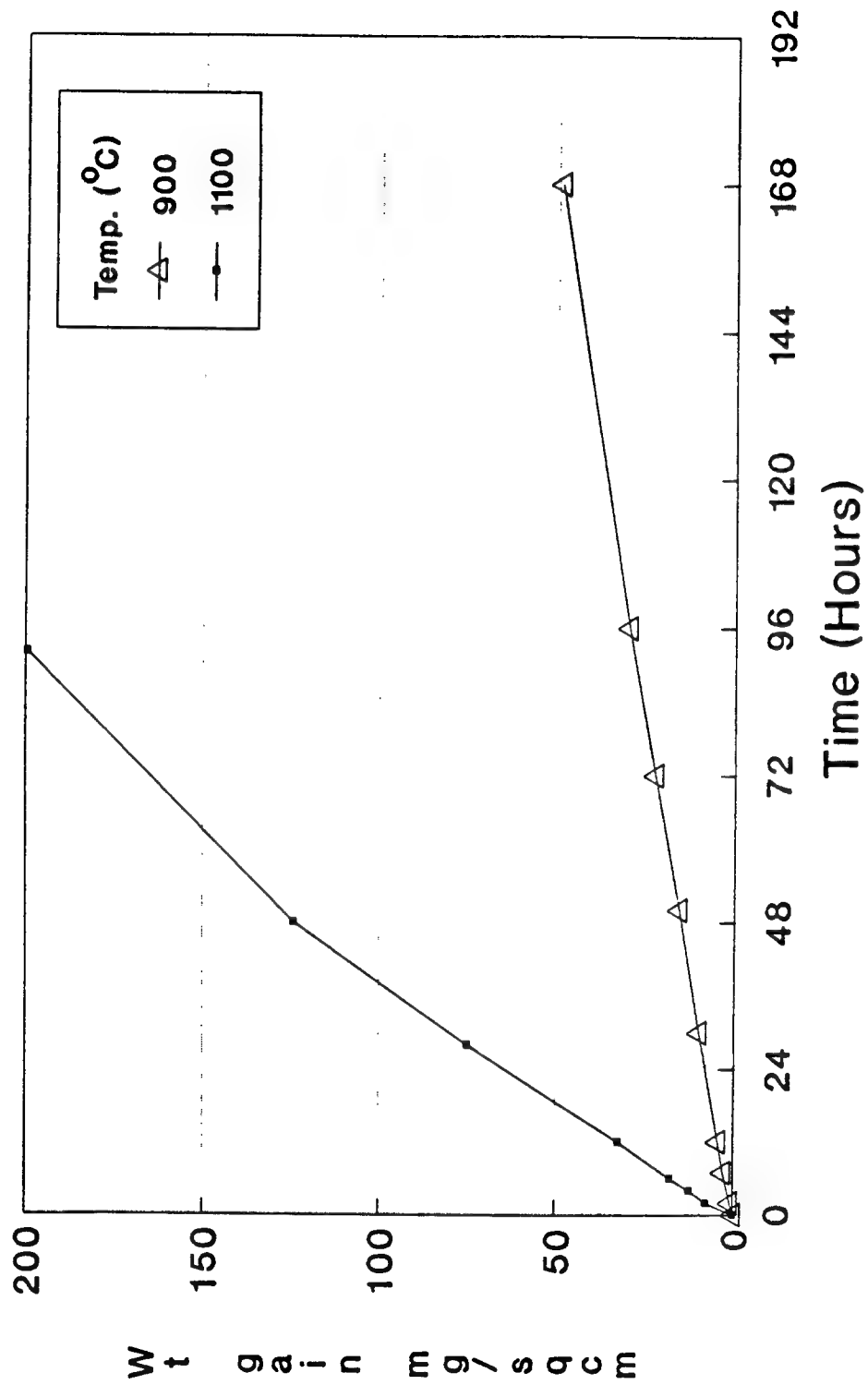


Figure 22 Differential Thermal Analysis Profile for  $\text{Al}_3\text{Ti} + \text{Nb}$ .



All specimens tested as-cast.

Figure 23 Weight Gain of AlTi in Cyclic Oxidation.

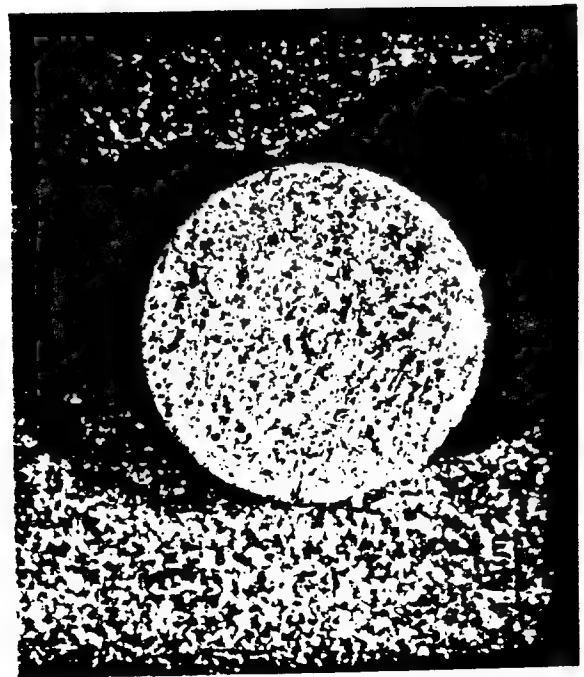




(a)



(b)



(c)

Figure 24 Appearance of Specimens after 28 Hours Cyclic Oxidation at 1100°C: (a) AlTi, (b) Al<sub>5</sub>CuTi<sub>2</sub>, and (c) Al<sub>3</sub>Ti.

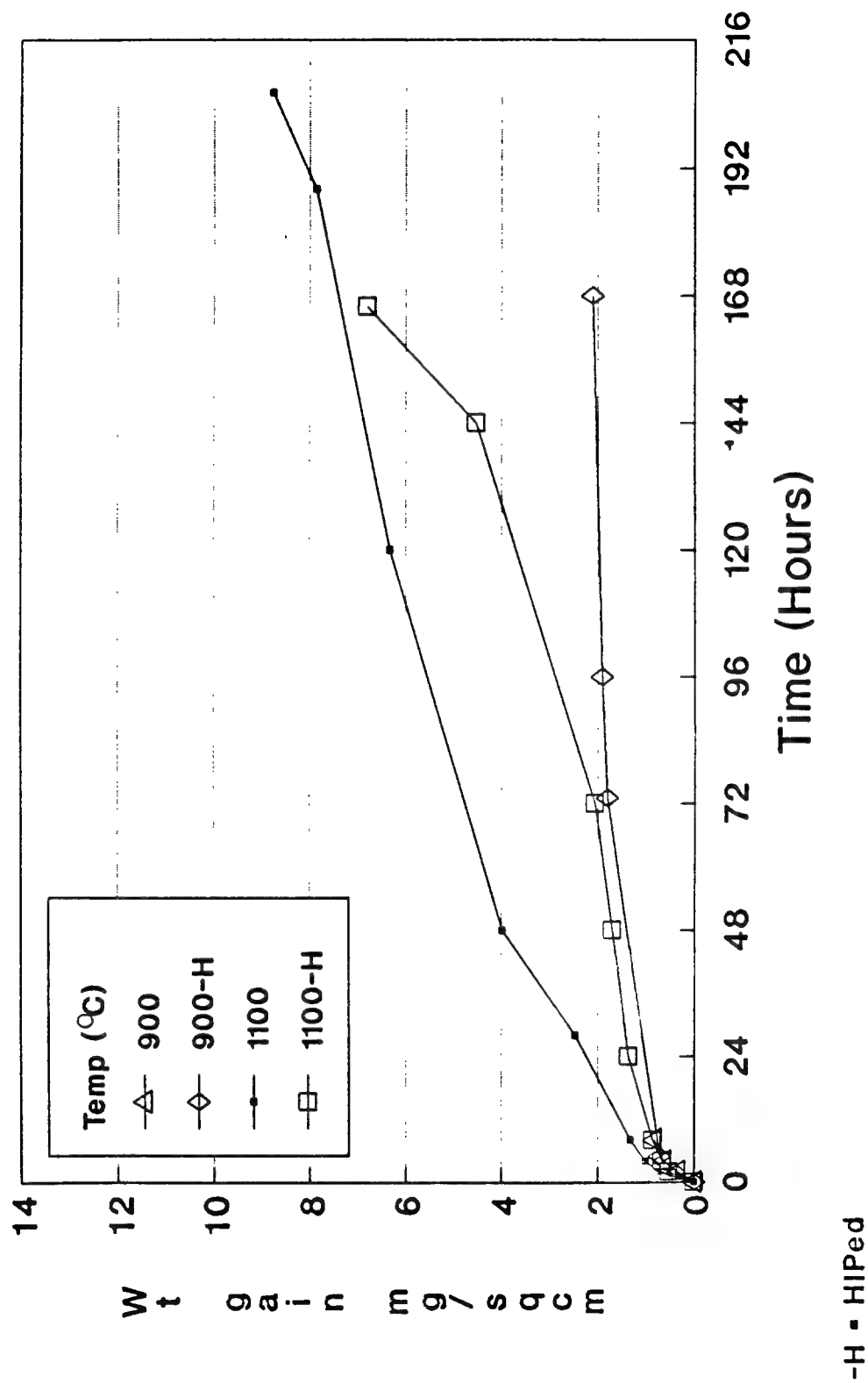


Figure 25 Weight Gain of  $Al_3Ti$  in Cyclic Oxidation.

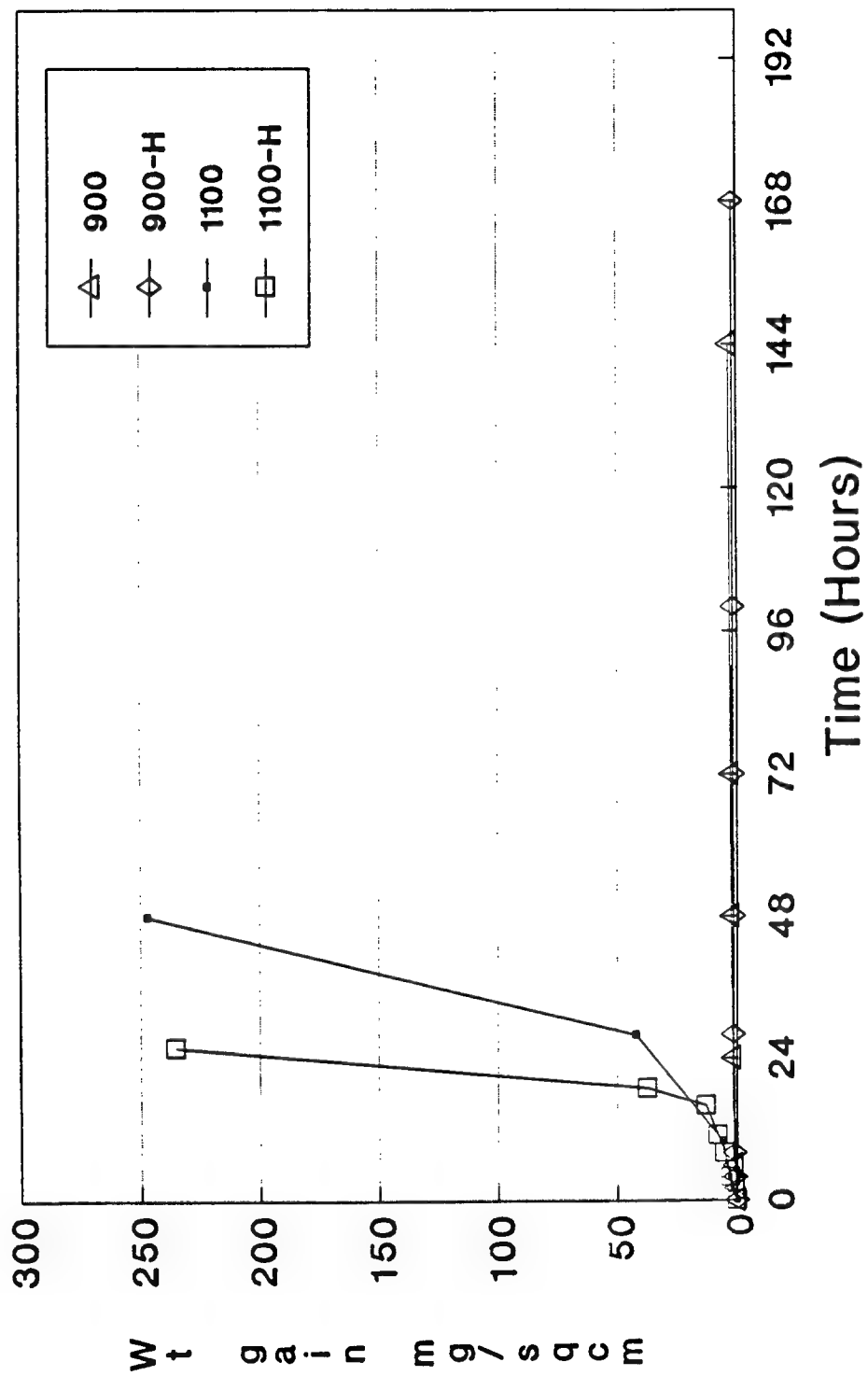
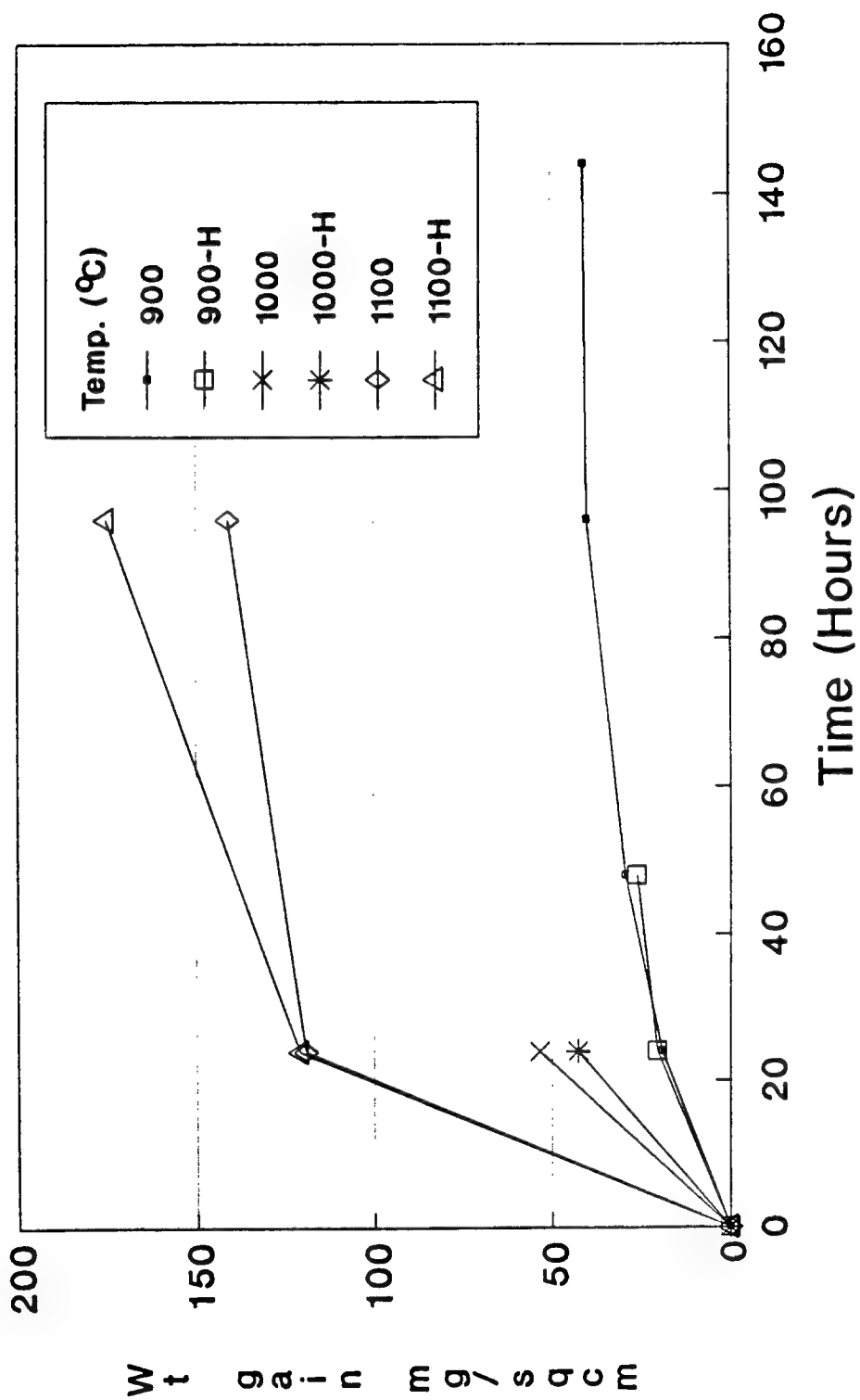
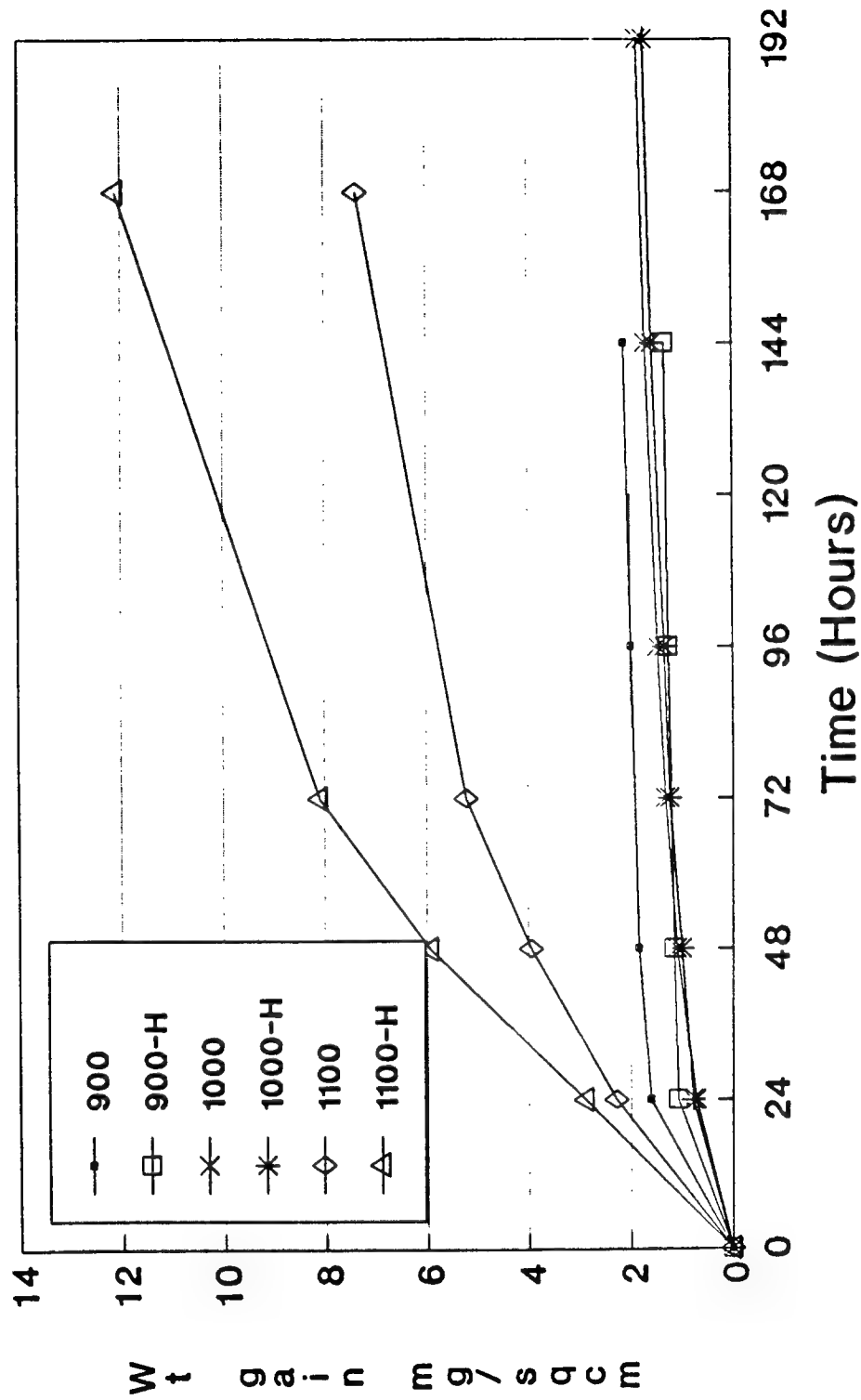


Figure 26 Weight Gain of Al<sub>5</sub>CuTi<sub>2</sub> in cyclic oxidation.



-H = Cast + HIPed. Others were as-cast.

Figure 27 Weight Gain of AlTi in Isothermal Oxidation.



-H = HIPed

Figure 28 Weight Gain of  $Al_3Ti$  in Isothermal Oxidation.

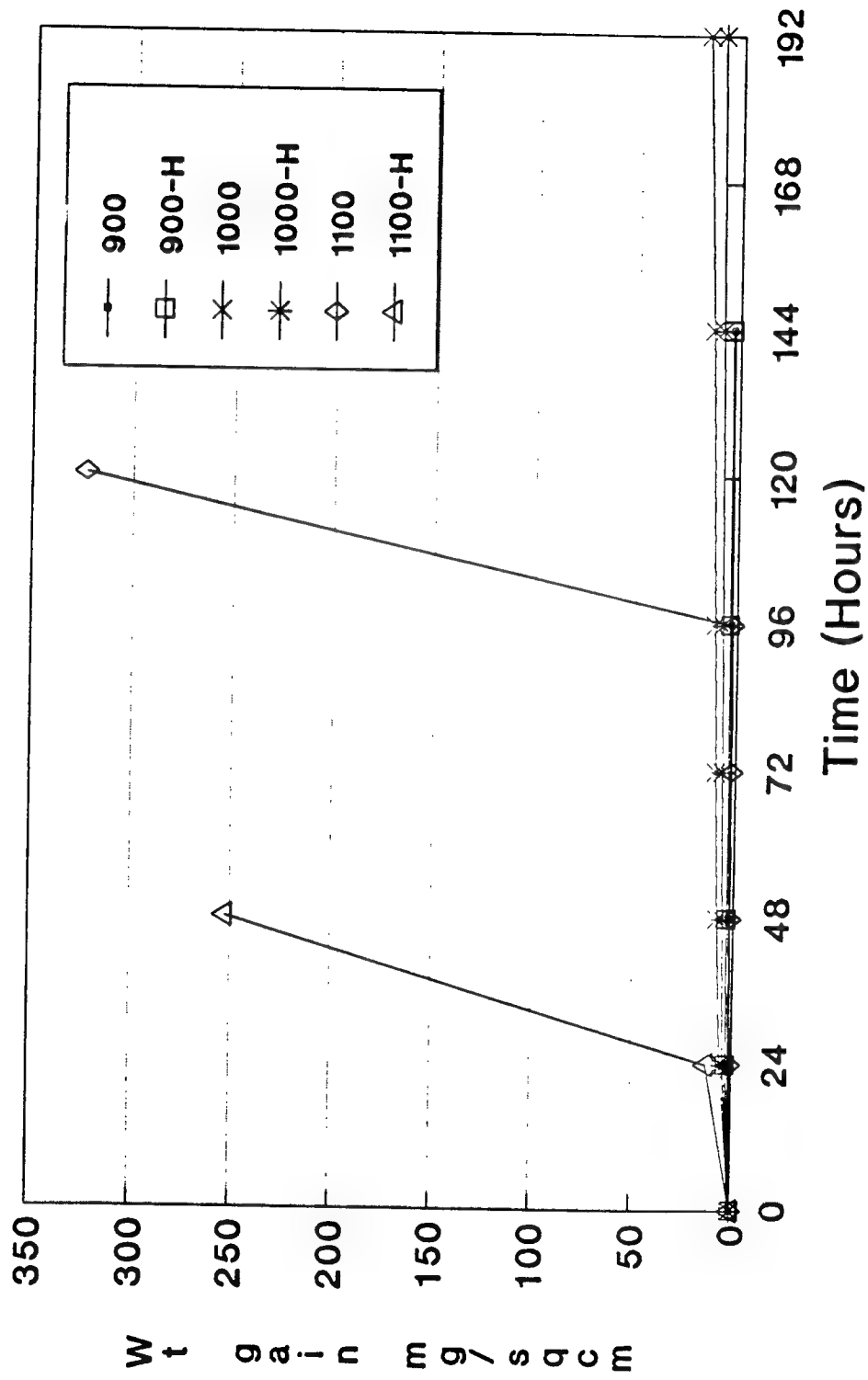


Figure 29 Weight Gain of  $Al_5CuTi_2$  in Isothermal Oxidation.

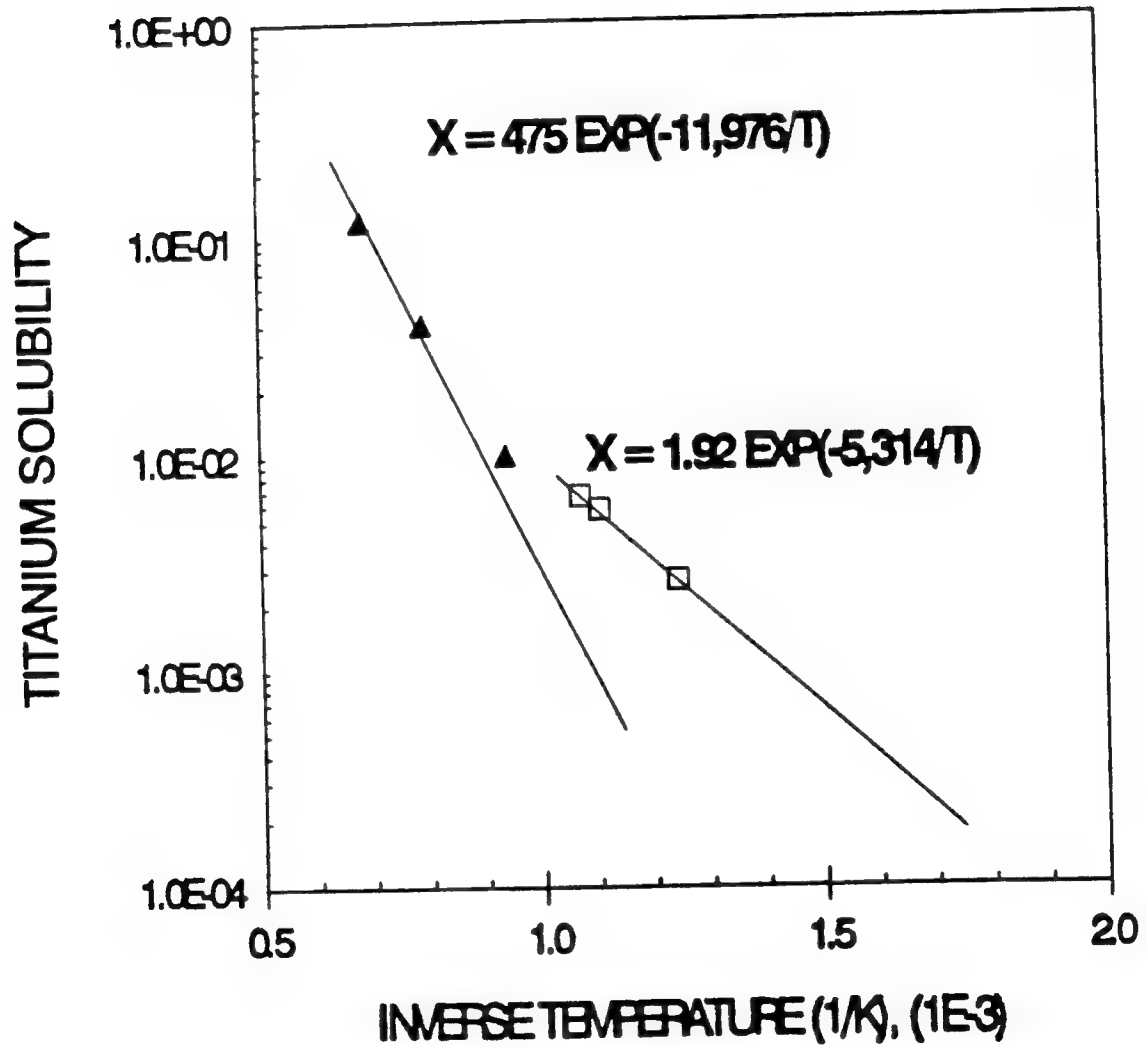


Figure 30 Solubility of Titanium in Aluminum.

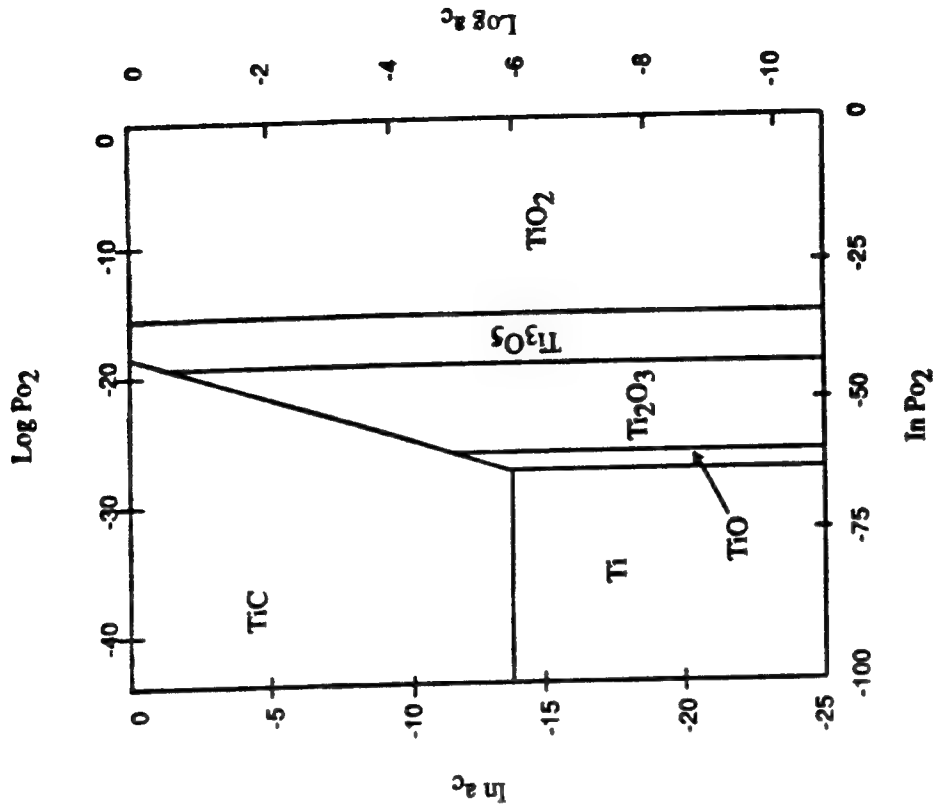


Figure 32 Al-C-O Phase Stability Diagram at 1200°C.

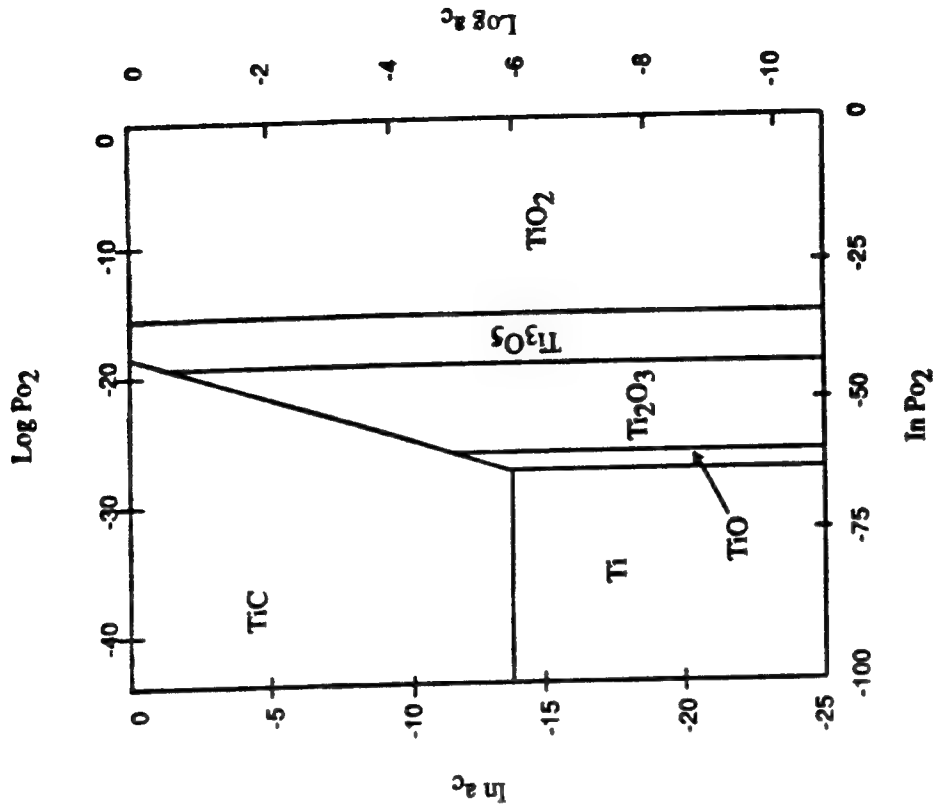


Figure 33 Ti-C-O Phase Stability Diagram at 1200°C.



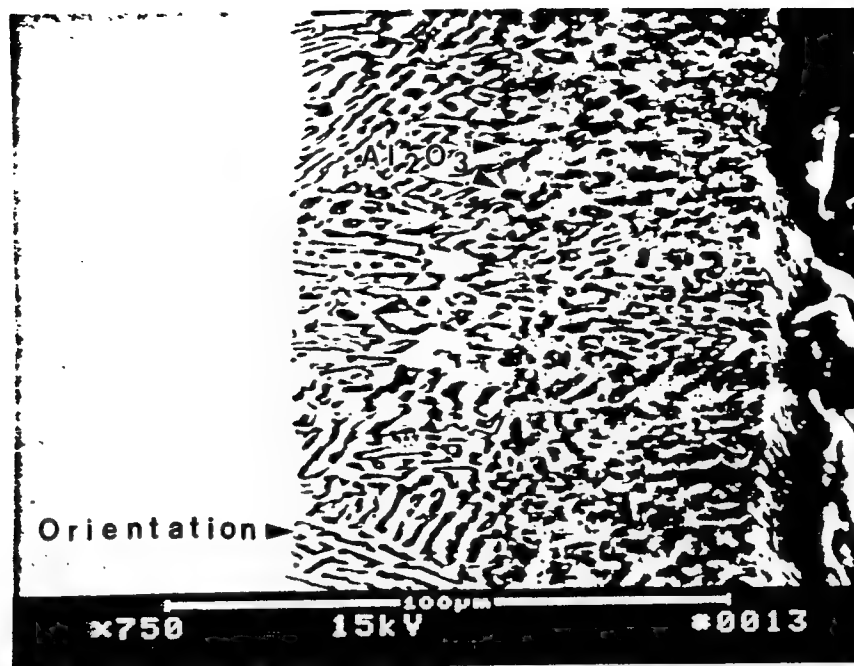
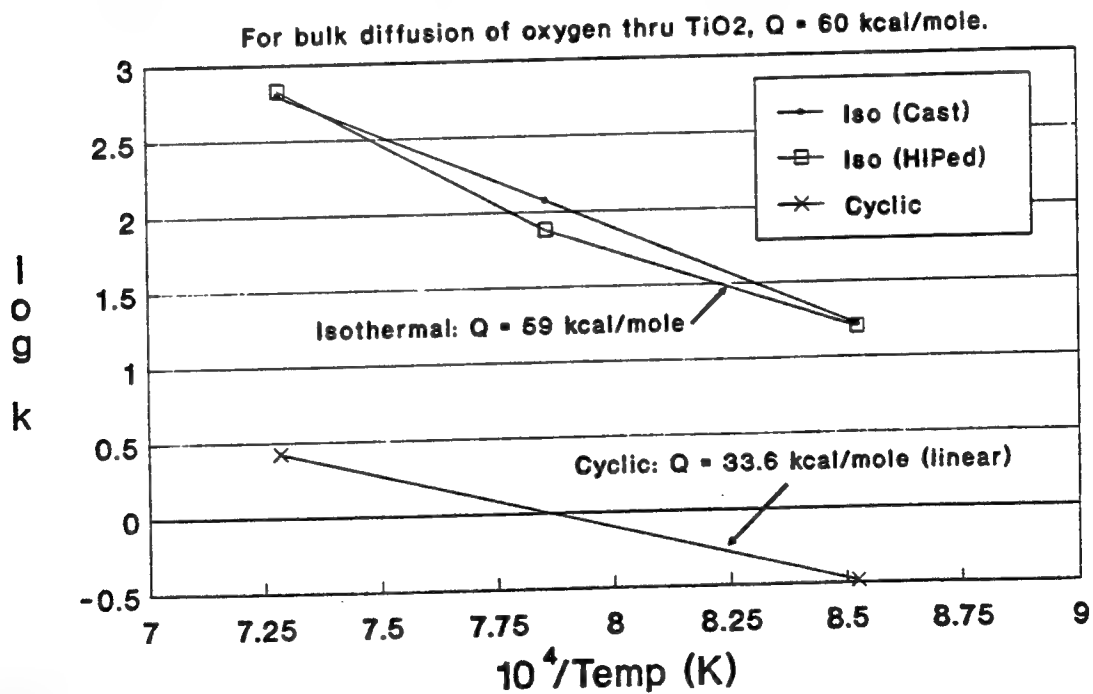


Figure 34 SEM Image of AlTi after Cyclic Oxidation, Showing Internal Oxidation of Aluminum.



Oxidation was parabolic under isothermal conditions, linear under cyclic conditions

Figure 35 Oxidation Kinetics for AlTi.

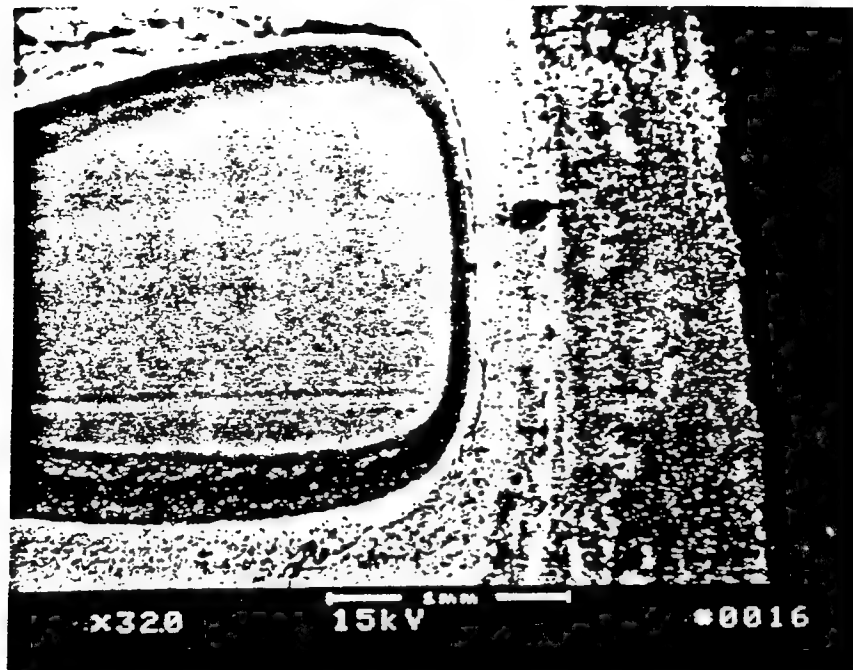


Figure 36 SEM Image Showing the Oxide Layer on AlTi after 48 hours Isothermal Oxidation at 1100°C.

### Oxidation of $\text{Al}_3\text{Ti}$ Cyclic Oxidation

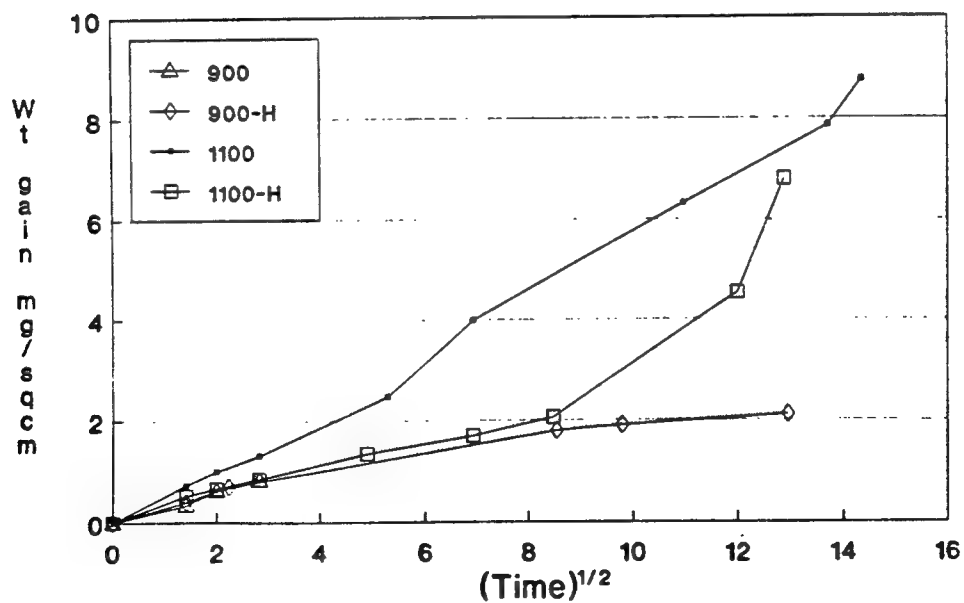


Figure 37 Parabolic Weight Gain Curves for  $\text{Al}_3\text{Ti}$  in Cyclic Oxidation.

# Oxidation Kinetics - $\text{TiAl}_3$

Q for bulk diffusion of oxygen thru  $\text{Al}_2\text{O}_3$  = 100 kcal/mole  
 Q for grain boundary diffusion = 32 kcal/mole

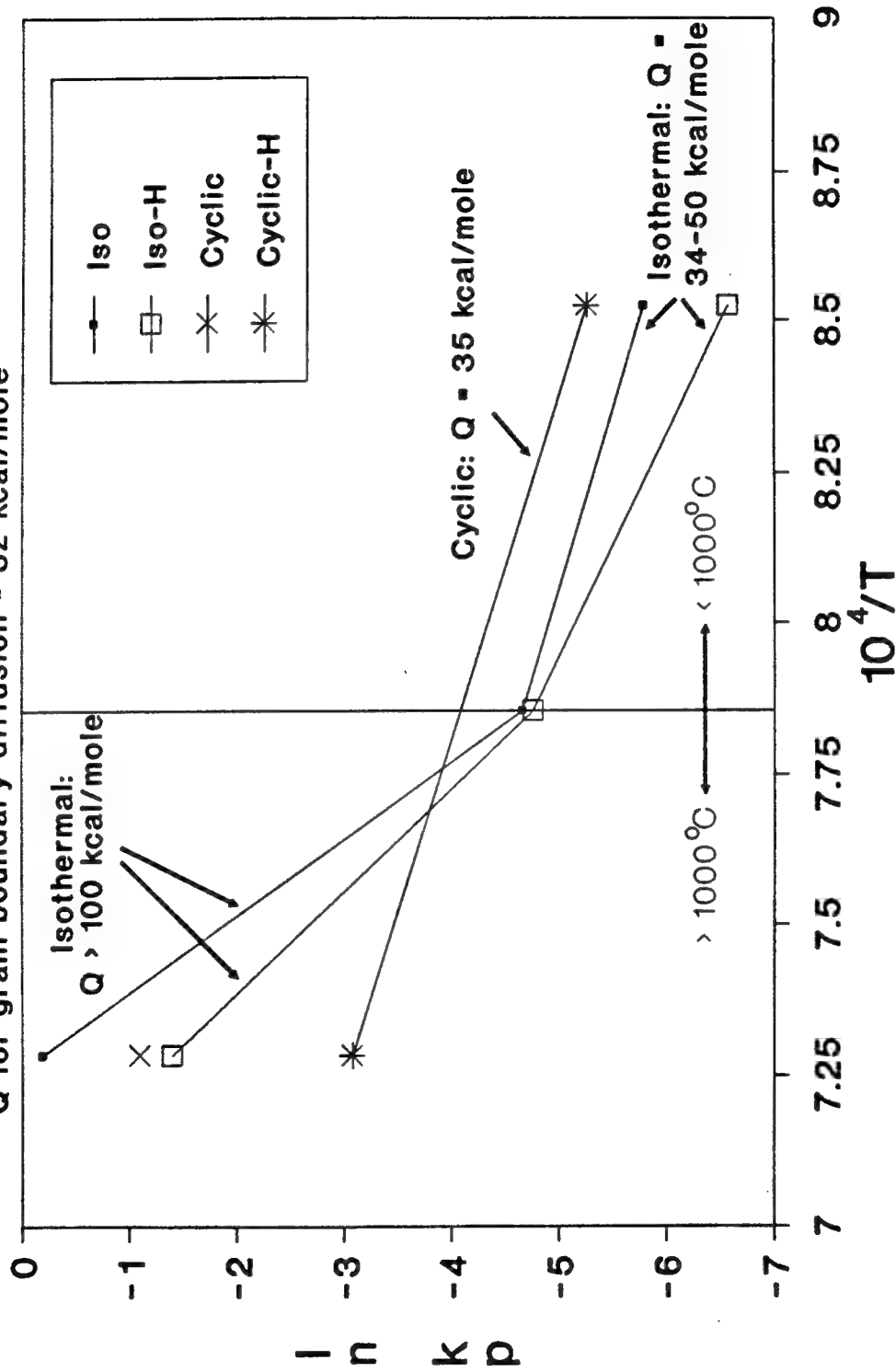


Figure 38 Oxidation Kinetics for  $\text{Al}_3\text{Ti}$ .

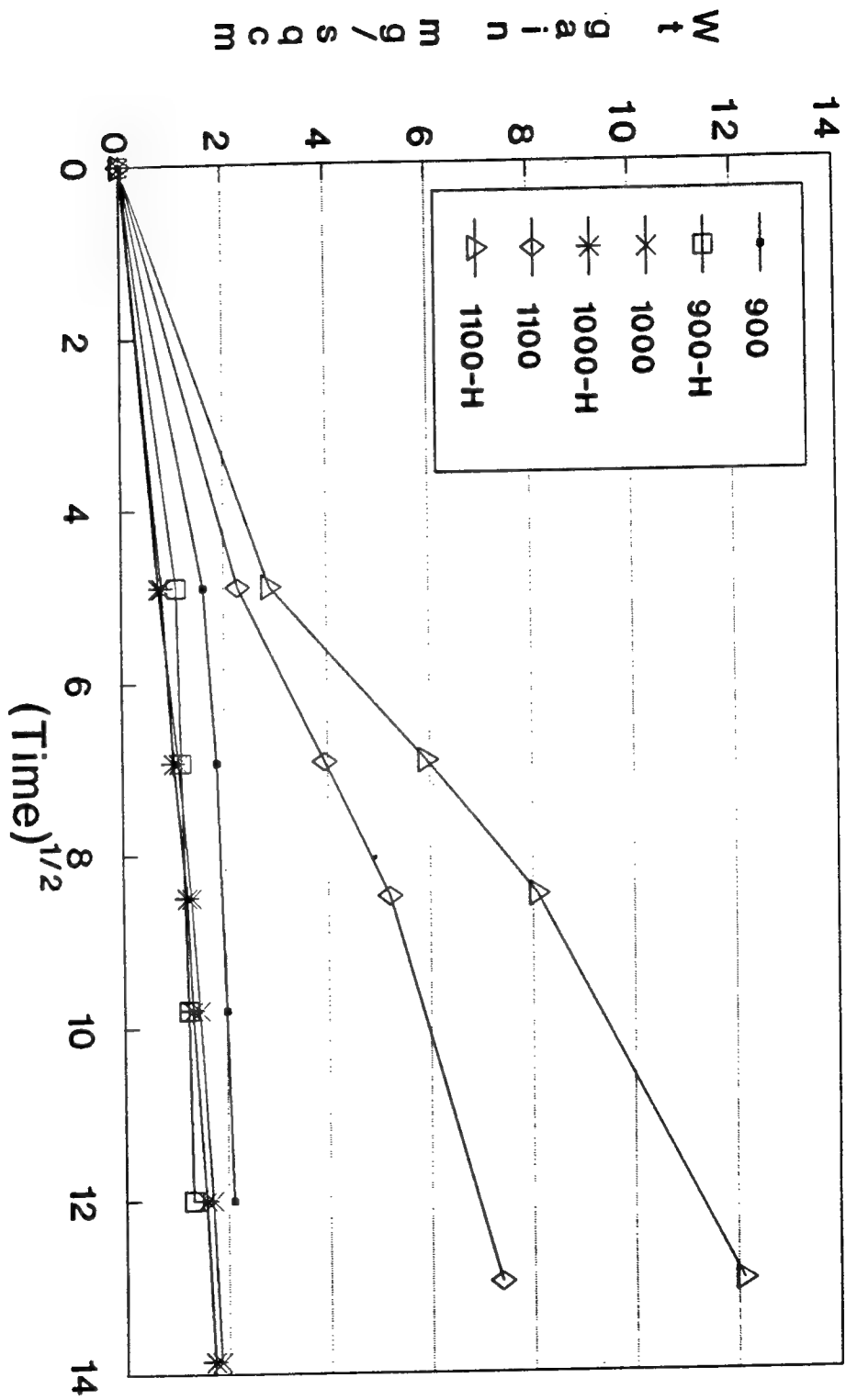


Figure 39 Parabolic Weight Gain Curves for  $\text{Al}_3\text{Ti}$  in Isothermal Oxidation.

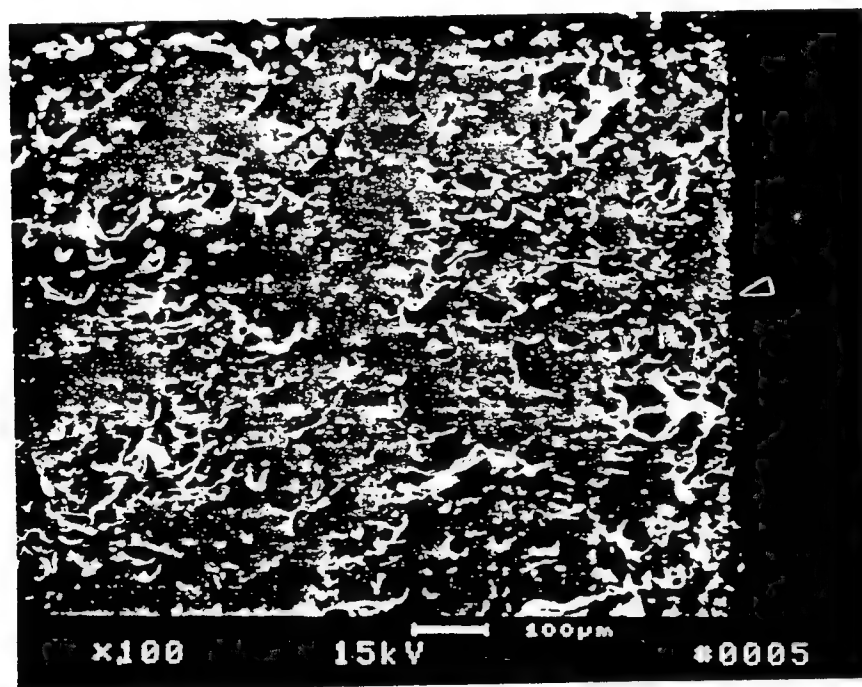


Figure 40 SEM Image of  $\text{Al}_3\text{Ti}$  Showing External Oxide Formation and Internal Oxidation after Isothermal Exposure at  $1100^\circ\text{C}$ .

# Oxidation of $\text{Al}_5\text{CuTi}_2$ Cyclic Oxidation

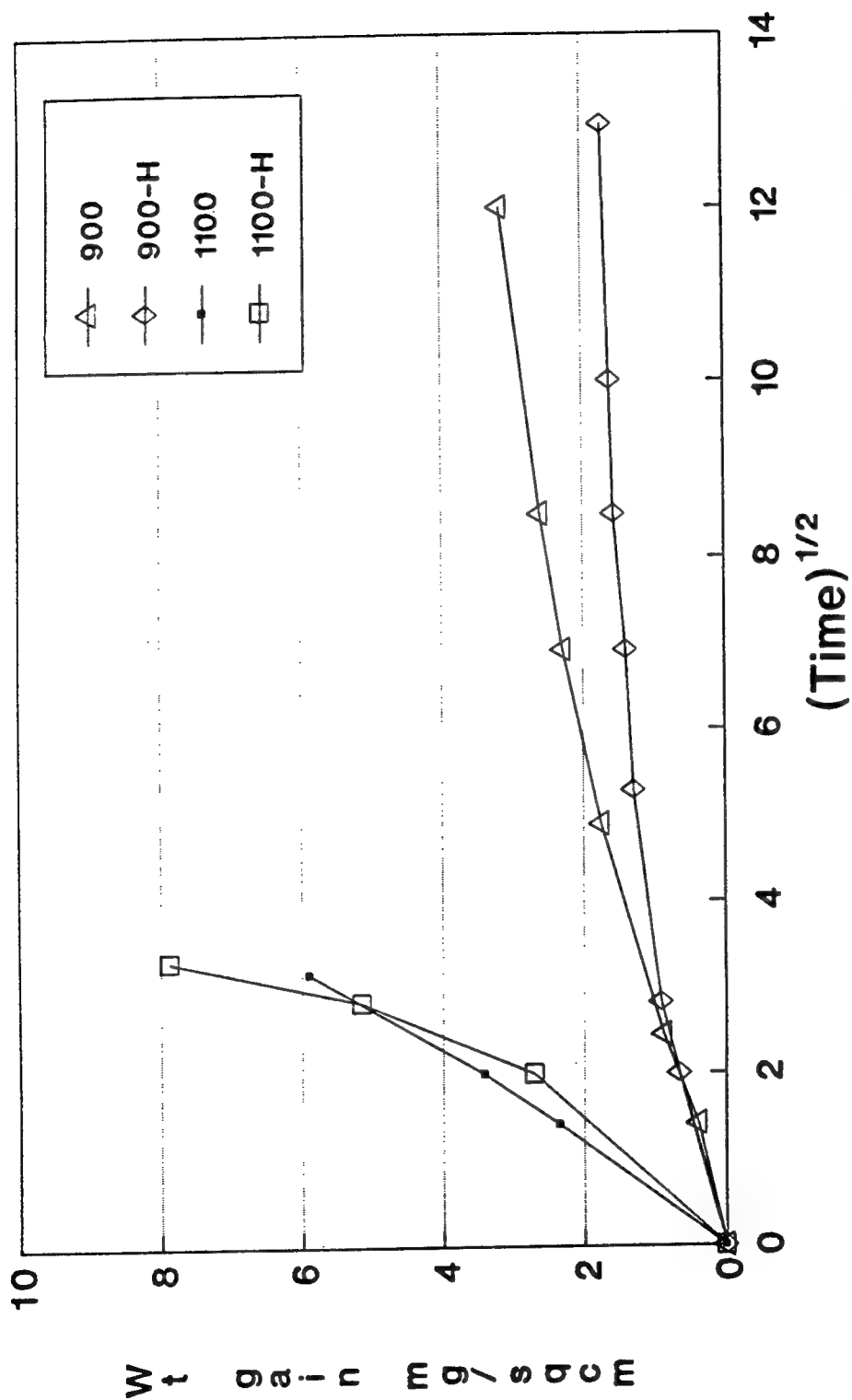


Figure 41 Parabolic Weight Gain Curves for  $\text{Al}_5\text{CuTi}_2$  in Cyclic Oxidation.

# Oxidation of $\text{Al}_5\text{CuTi}_2$ Isothermal Oxidation

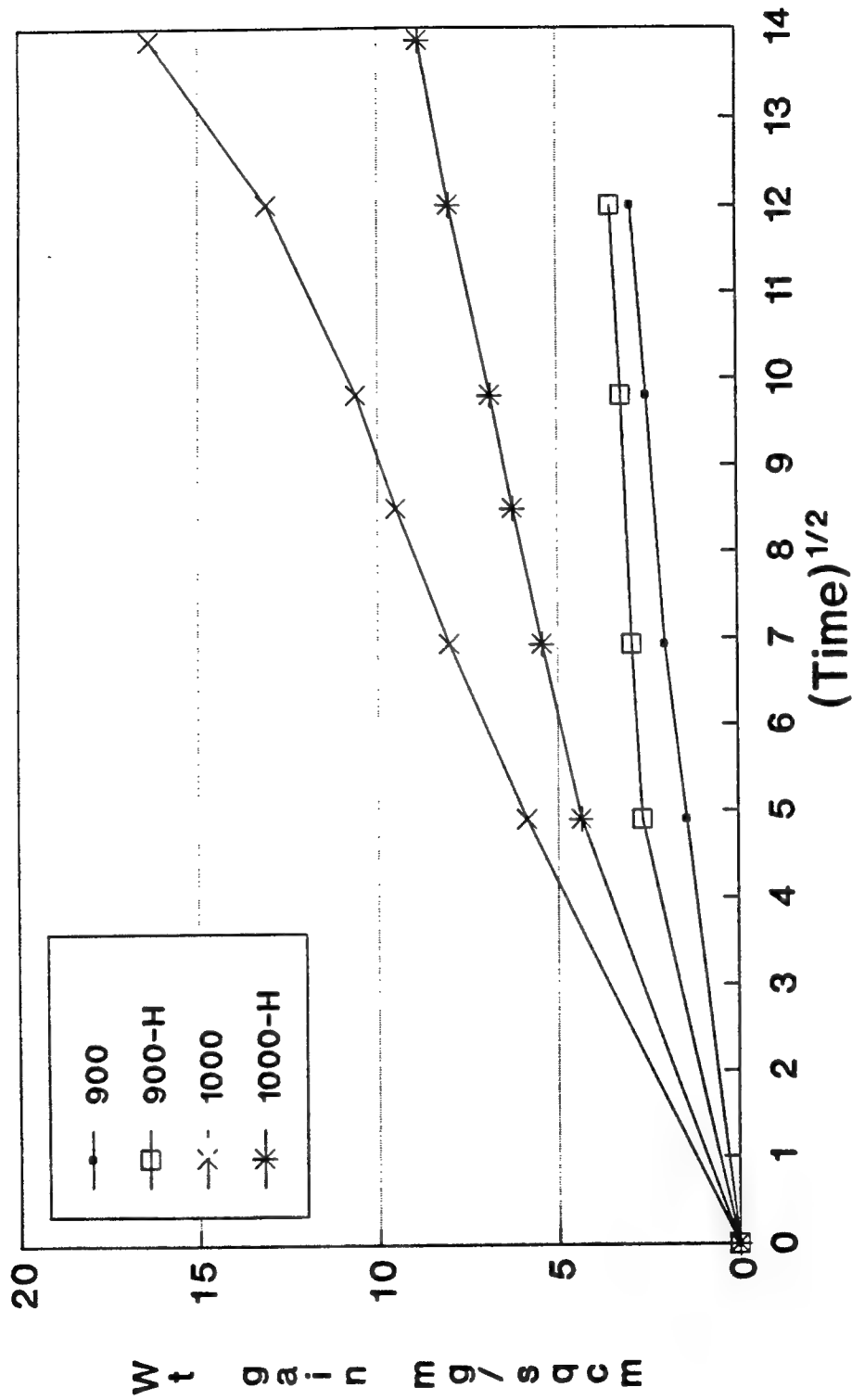


Figure 42 Parabolic Weight Gain Curves for  $\text{Al}_5\text{CuTi}_2$  in Isothermal Oxidation.

University of California, Dept. of Materials Science,  
Berkeley, CA, 94720, J. Morris, Jr., R. O. Richie.....2

University of California, Santa Barbara CA 93106,  
C. G. Levi.....1

University of Pennsylvania, School of Engineering and  
Applied Science, 109 Town Building David Pope.....1

U.S. Air Force, AFOSR/NE Bldg. 410, Bolling AFB,  
Washington, DC 20332-6448, Dr. Allen H. Rosenstein .....1

The Wichita State University, Dept of Mechanical  
Engineering, Wichita, KS 67208, Jorge E. Talia.....1



Innovare Inc., Airport Road, Commonwealth Park,  
7277 Park Drive, Bath, PA 18014, Al R. Austen.....1

Lockheed Missiles and Space Co., Metallurgy Dept. 93-  
10/204, 3251 Hanover St., Palo Alto CA 94304,  
R. Lewis and J. Wadworth.....2

Marko Materials Inc., 144 Rangeway Rd., N. Billerica,  
MA 01862, R. Ray.....1

Martin Marietta Laboratories, 1450 South Rolling Rd.,  
Baltimore, MD 21227-3898, J. Venables, K.S. Kumar.....2

Massachusetts Institute of Technology, 77 Massachusetts  
Av., Cambridge, MA 20139, J. Cornie.....1

Metal Working News, 201 King of Prussia Rd., Radnor, PA  
19089, R. R. Irving.....1

Metal Working Technology Inc. 1450 Scalp Avenue,  
Johnstown, PA 15904, W. L. Otto.....1

McDonnell Aircraft Co., Box 516, Saint Louis, MO 63166,  
K. K. Sankaran.....1

Michigan Technological University, Houghton, Michigan  
49931, M. McKimpson.....1

NASA Headquarters, 600 Independence Av., Washington,  
DC 20546, N. Mayer, S. Vennesi.....2

NASA Langley Research Center, Hampton, VA 23365,  
A. Taylor, L. Blackburn, .....2

National Bureau of Standards, Gaithersburg, MD 20899,  
R. Shaffer, J. R. Manning.....2

National Science Foundation, Office of Science and  
Technology Centers Division, 1800 G Street,  
Washington, DC 20550, L. W. Haworth.....1

NAWCADWAR, Warminster, PA, 18974-5000,  
Library, Code 8131 (2 Copies),  
W.E. Frazier, Code 6063 (15 Copies).....17

NAVAIRSYSCOM, Washington, DC 20361, J. Collins Air-  
5304, L. Slotter Air-931.....2

NAWCADWAR, Lakehurst, NJ 08733-5100, R. Celin (AV624-  
2173), R. Jablonski (AV624-2174), G. Fisher (SESD)  
(AV624-1179), B. Foor (02T) .....4

NAWCADWAR, P.O. Box 7176, Trenton, NJ 08628-0176,  
F. Warvolis (PE34), A. Culbertson, .....2

Naval Air System Command, Washington, DC 20361-5140,  
     R. A. Retta (AIR-51412), .....1

Naval Air System Command, Washington, DC 20361-5140,  
     J. Jarrett (AIR-51412J), .....1

Naval Industrial Resources Support Activity, Bldg. 75-2  
     Naval Base Phila., PA 19112-5078, L. Plonsky  
     (NAVIRSA-203) .....1

Naval Industrial Resources Support Activity, Bldg. 75-2  
     Naval Base, Phila., PA 19112-5078, D. Fabry  
     (NAVIRSA-204) .....1

Naval Post Graduate School, Mechanical Engineering  
     Department, Monterey, CA 93943, T. McNelly .....1

Naval Research Laboratory, Washington, DC 20375,  
     Metallurgy .....1

Northrop, Aircraft Division, One Northrop Av.,  
     Hawthorne, CA 90250, S. P. Agrawal and  
     G. R. Chanani .....2

Office of Naval Research, 800 Quincy St. , Arlington,  
     VA 22217-5000  
     G. Yoder (1 copy)  
     S. Fishman (6 copies) .....7

Rice University, MEMF, P.O. Box 1892, Houston, TX  
     77251, Enrique Berrera .....1

Temple University, Dept. of Mechanical Engineering,  
     12th & Norris St. Phila., PA 19122, Jim S.J. Chen ....1

United Technologies Research Center, East Hartford,  
     Connecticut 06108, William P. Allen, D.N. Duhl .....2

University of California, Dept. of Mechanical  
     Engineering, Irvine, CA 92717, Enrique J. Lavernia .....1

University of Wisconsin, Department of Metallurgy and  
     Mineral Engineering, 1509 University Av., Madison, WI  
     53706, John H. Perepezko .....1

Wayne State University, 5050 Anthony Wayne Drive,  
     Detroit, MI 48202, John Benci .....1

Worcester Polytechnic Institute, 100 Institute Road,  
     Worcester MA 01609-2280, D. Apelian .....1

Pratt and Whitney, P.O. Box 109600 West Palm Beach, FL  
     33410-9600, B. H. Walker, R. Anderson .....2

## DISTRIBUTION LIST

	Copies
Air Force Wright Aeronautical Lab., Wrigth Patterson AFB, OH 45433, W. Griffith (MLTM) and J. Kleek (WL/MLLM), .....	2
ARPA, 3701 North Fairfax Drive, Arlington, VA 22203, William Barker, Robert Crowe, Benn Wilcox.....	3
Allied-Signal Corp., P.O. Box 1021R, Morristown, NJ 07960, S.K. Das and P. Gilman.....	2
BDM International, Inc., 4001 N. Fairfax Dr. #750, Arlington, VA 22203, P. A. Parrish.....	1
Boeing Commercial Airplane, Seattle WA , W. Quist.....	1
Center for Naval Analyses, 4401 Front Ave., P.O. Box 16268 Alexandria, VA 22302-0268.....	1
Clemson University, Dept. of Mechanical Engineering, Riggs Hall, Clemson, SC 29634-0921, H.J. Rack.....	1
Defense Technical Information Center, Bldg. #5, Cameron Station, Bldg. 5, Alexandria, VA 22314 (Attn. Adminstrator).....	2
Department of Energy, 100 Independence Av., SW Washington, DC 20585, Code CE142.....	1
Drexel University, Dept. of Materials Engineering, 32nd and Chestnut St., Phila., PA 19104, M. J. Koczak .....	1
Elkem Development Center, 200 Deer Run Road, Sewickley, PA 15143, Deepak S. Madan.....	1
Garrett Auxiliary Power Division, 2739 East Washington Street, P.O. Box 5227, Phoenix, AZ 85010, C. McCormick.....	1
Grumman Areospace Corp., Bethpage, NY 11714, M. Donnellan, P. N. Adler.....	2
Howmet Corp, 1500 South Warner St. Whitall, MI 49461- 1895, Metallurgy.....	1
Idaho National Engineering Laboratory, P.O. Box 1625, Idaho Falls, ID 83415, J. R. Knibloe.....	1
Inco Alloys International, P.O. Box 1958, Huntington, WV 25720, J. deBarbadillo.....	1